Hydraulic bulge test for the mechanical characterization of uncoated and drug-coated polymeric materials constituting angioplasty balloons

MASTER THESIS IN BIOMEDICAL ENGINEERING

Martina Ferrari - 968652
Elena Fomiatti - 969181

Contents

Acknowledgements

Special thanks to:

Professor Vena, for accompanying us during the final part of our university journey. Not only did he enrich our knowledge, but he also taught us the importance of being independent in finding answers to our doubts;

Luca and Deepthi, for their support throughout our thesis;

our families, boyfriends, and friends, for standing by our side during this long journey at Politecnico di Milano.

Thank you to all of you who have been a part of this great achievement of ours.

Abstract

Peripheral Artery Disease (PAD) is a pathologic process leading to obstruction of vessels that carry blood from the heart to the body's extremities. Because they provide a solution for vessel opening, angioplasty balloons are a reliable instrument for treating PAD. Drug-coated balloons (DCBs) are a promising option as they can reduce complications associated with in-stent restenosis and late thrombosis resulting from stent implantation by providing a high drug dosage directly to the vessel. However, the main drawback of the current DCBs is the lack of effective drug delivery control, which can result in low therapeutic levels and drug loss. To address this issue, it is crucial to evaluate the multi-axial mechanical response of the balloon material and the drug coating.

This research aims to investigate the mechanical properties of polymer substrates and evaluate the excipient layer's and the excipient-drug system's mechanical response under strain. Uniaxial and multiaxial (bulge test) stressing during in-situ mechanical testing are used to accomplish these goals. Firstly, the study provides a quantitative analysis of the mechanical behavior of the polymeric substrate itself. Secondly, the coating integrity is investigated in relation to the results obtained in the first step.

The bulge test and the concurrent use of confocal laser microscopy enable the extraction of displacement data regarding the inflation of the examined samples at various pressure levels.

The mechanical properties of the polymeric substrate are investigated by subjecting Nybax® and Nylon angioplasty balloons, as well as Pebax® films, to uniaxial tensile tests using a tensile loading device to determine the material parameters.

On the other hand, a bulge loading system is used to accomplish multiaxial loading, which provides a correlation between the applied pressure and the sample deflection. Ultimately, the experimental scenario is reproduced through a finite element model. In this way, the parameters of the analytic model that accurately describes the material's behavior have been identified.

As stress and strains cannot be directly measured during the bulge test, simulations that best fit the experiments are assumed to provide information on the membrane's surface strain during bulging. Therefore, the mechanical integrity of both polymer-coating and drug-polymer-coating on Pebax® samples is evaluated through bulge test. The results obtained with the numerical simulations provide insight into the critical strain that leads to coating fracture.

Key-words: angioplasty balloons, bulge test, mechanical characterization.

Abstract in italiano

La Malattia Arteriosa Periferica (MAP) è un processo patologico che porta all'ostruzione dei vasi che trasportano il sangue dal cuore alle estremità del corpo. Poiché forniscono una soluzione per l'apertura dei vasi, i palloni per angioplastica sono uno strumento affidabile per il trattamento della MAP. I palloni rivestiti di farmaco (drug-coated balloons, DCBs) sono una promettente opzione, in quanto riducono le complicanze associate alle restenosi intra-stent e alla trombosi tardiva dovuta all'impianto dello stent, fornendo un'elevata dose di farmaco direttamente al vaso. Tuttavia, il principale svantaggio degli attuali DCBs è il controllo inefficace della somministrazione del farmaco, dovuto spesso alla delaminazione del rivestimento durante la procedura. Per affrontare questo problema, è fondamentale valutare la risposta meccanica multi-assiale del pallone e del rivestimento di farmaco.

Questa ricerca mira ad indagare le proprietà meccaniche dei substrati polimerici e valutare la risposta meccanica dello strato di eccipiente e del sistema eccipiente-farmaco sotto sforzo. Per raggiungere questi obiettivi, si utilizzano prove meccaniche in-situ uniassiali e multi-assiali (test di rigonfiamento). In primo luogo, lo studio fornisce un'analisi quantitativa del comportamento meccanico del substrato polimerico. In secondo luogo, l'integrità del rivestimento è indagata in relazione ai risultati ottenuti nella prima fase. Il test di rigonfiamento e l'uso concomitante del microscopio laser confocale consentono di estrarre gli spostamenti relativi al gonfiaggio dei campioni esaminati a vari livelli di pressione. Le proprietà meccaniche del substrato polimerico sono indagate sottoponendo i palloni in Nybax® e Nylon, così come i film in Pebax® a test di trazione uniassiali per determinare i parametri del materiale. Contrariamente, un sistema di gonfiaggio viene utilizzato per ottenere una sollecitazione multi-assiale che fornisce una correlazione tra la pressione applicata e la deflessione sperimentata dal campione. Infine, lo scenario sperimentale viene riprodotto attraverso un modello a elementi finiti. In questo modo, si identificano i parametri del modello analitico che descrivono accuratamente il comportamento del materiale. Poiché gli sforzi e le deformazioni non possono essere misurati sperimentalmente, si assume che le simulazioni forniscano informazioni sulla deformazione superficiale della membrana durante il gonfiaggio. Pertanto, l'integrità meccanica del rivestimento (polimerico e farmaco-polimerico) sui campioni di Pebax® è valutata attraverso il test di gonfiaggio e le simulazioni forniscono informazioni sulla deformazione critica che porta alla rottura del rivestimento.

Parole chiave: palloni per angioplastica, test di rigonfiamento, caratterizzazione meccanica.

1 Introduction

1.1. Peripheral artery disease

Peripheral Arterial Disease (PAD) is the pathologic process leading to obstruction of vessels that carry blood from the heart to the body's extremities (Figure 1). The most common cause of this disease is atherosclerosis; fewer common causes include inflammatory disorders of the arterial wall (vasculitis) and noninflammatory arteriopathies [1]. The consequences are flow-limiting stenosis or total occlusion of arteries. Atherosclerosis is responsible for cardiovascular diseases in millions of patients every year [2], and it is mainly treated by endovascular methods.

Percutaneous Transluminal Angioplasty (PTA) with or without stenting is among the preferred choices for the treatment of PAD. However, results are poor, with 50–85% of patients developing significant restenosis (re-occlusion), and 16-65% developing occlusions within 2 years post-treatment [3].

The primary success rate of PTA is 90-95%; however, secondary success is not satisfactory. At the coronary site, restenosis occurs in about 40% of lesions within 6 months from the procedure [4].

The use of drug-eluting stents (DES), or rather bare metal stents coated with anti-proliferative drugs, was a breakthrough and successful in treating coronary artery disease. However, stents have shown very poor clinical outcomes in treating PAD, because they are located in body regions subjected to frequent movement.
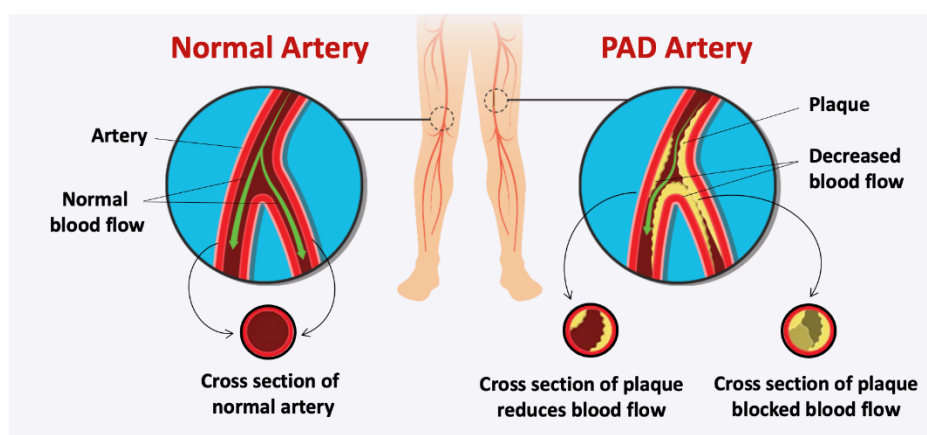

Figure 1: Normal artery (left-hand side) and Peripheral Arterial Disease (PAD) artery (right-hand side).

1.2. Angioplasty balloons

Peripheral arteries normally undergo large deformations, such as twisting, bending, and shortening. Therefore, stents experience high biomechanical stresses, leading to high fracture rates and restenosis.

Angioplasty balloons are a robust tool to treat PAD. The working principle is to open mechanically an occluded vessel using the inflated balloon.
The balloon is assembled on a catheter and can be inflated internally, with a pressure > 10 atm [5]. After inserting the catheter into the femoral artery, the surgeon moves the catheter through the vessel until the balloon reaches the area of plaque deposition.
Balloons are designed to inflate and conform to the arterial wall to apply a counter-pressure to the fatty or calcified lesions and prop open the artery. After inflation for several seconds pushing the plaque against the wall and opening up the artery, the balloon is deflated to allow returning blood flow to travel downstream. It is then refolded and retracted out of the artery through the delivery system [6].

Because of pressure against the arterial wall and tissue damage during the procedure, scar tissue could develop within some months, causing restenosis of the treated vessel. To avoid that, drug-coated balloons (DCB) could be a solution. DCBs are angioplasty balloons coated with an antiproliferative therapeutic drug and an excipient (drug carrier) [3].
They act by transferring the drug from the coating to the vessel lumen, combining the advantage of opening the blood vessel and the release of the drug to treat lesions. In comparison with DES, DCBs provide a larger contact area to the arterial wall, resulting in a more homogeneous drug-tissue transfer [7].

Since the balloons need to be inflated to open clogged vessels, they must withstand internal pressure on the order of tens of atmospheres. Moreover, the balloon material must provide a strong interface to the coating without compromising mechanical properties, such as strength and burst pressure [6].

1.2.1. Drug coated balloons

In recent years, drug-coated balloons (DCBs) have emerged as a therapeutic alternative to drug-eluting stents (DES) in the field of vascular intervention. These balloons provide a short-term transfer of antiproliferative drugs, such as paclitaxel (PTX), to the arterial wall.

DCB reduces the complications of in-stent restenosis and late stent thrombosis associated with stent implantation by providing a high dosage of the drug to the vessel wall initially with little impact on long-term healing. Furthermore, the absence of a

remaining foreign body in the artery and high deliverability is opening the opportunity for their use in small vessels, bifurcations, or long lesions, which are hardly accessible by stents [8].

Clinical use of DCB has focused mainly on scenarios where stent implantation is not desirable or effective. The most encouraging data with DCB have been obtained in the coronary arteries, for treatment of in-stent restenosis and to a lesser extent in large peripheral vessels, such as in the femoro-popliteal artery segment [9].

Coating the angioplasty balloons' surface with drugs is a challenging task. It must ensure homogeneous distribution of the antiproliferative agent and adherence to the balloon membrane when it is inflated and traced through the artery [5].

Moreover, it must be sufficiently stable on the balloon surface to prevent premature release during passage through a hemostatic valve, a blood-filled guiding catheter, and flowing blood in the artery on the way to the targeted vessel. In addition, it should enable immediate and complete release during balloon inflation, to guarantee that the time between drug delivery and endothelial uptake is 30-60 seconds [9]. Finally, the drug must be suitable and provided in a sufficient dose, in order to ensure the inhibition of neointimal proliferation [5].

Coating methods include dipping, air spraying, ultrasonic spraying, micro pipetting, and others (Figure 2) [10].

The most common technique to apply coating on the balloon's surface is by micro-pipetting the drug-excipient solution. In this process, the folded balloon is rotated while a micro-pipette applies the solution along the surface of the balloon. Micro pipetting offers some advantages, such as homogeneity and controllable application, specific localization of the drug/excipient solution, and complete dose control.

The spray coating technique gives a more homogenous distribution of the drug on the balloon compared to micro pipetting, but the amount of drug loss during refolding remains unclear [9].

The least controlled coating method is the dip coating technique, which consists of the immersion of the balloon into the drug/excipient solution. This method leads to having a lower dose control, and low drug distribution homogeneity compared to micro-pipetting [9].
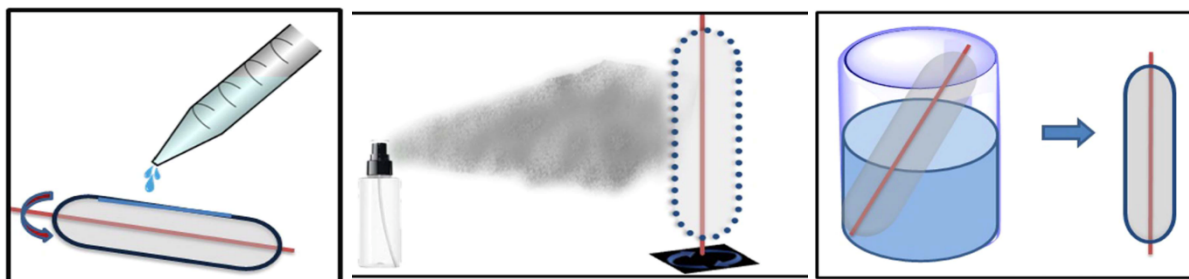

Figure 2: Coating methods: (a) micro-pipetting, (b) spray coating, (c) dip coating [11].

There are several well-known issues with DCBs based on their function. Most of these are related to the coating integrity of the balloon and the distribution of the drug to off-target organs. In addition, particulate matter may be generated from the delamination of the coating on the balloon-catheter and may cause occlusion of downstream blood vessels. Excess drug dosage to the target area will induce cytotoxicity. Furthermore, drug loss from the coating on the balloon may occur during device handling and tracking of the lesion.

To minimize these problems, companies have tried different drug-to-excipient combinations and ratios [11]. The excipient improves the adhesion of the drug to the balloon surface, increases the stability of the drug coating during handling and delivery, and maximizes drug retention to the targeted arterial segment [3]. DCBs in the current market use excipients like polysorbate and sorbitol, urea, polyethylene glycol (PEG), and butyryl-tri-hexyl citrate (BTHC) [3]. Excipients such as polysorbate and PEG act like cosolvents of paclitaxel, which can alter the vessel interaction of the drug with the DCB device. On the other hand, urea acts to increase paclitaxel release at the lesion and PEG has been shown to bind to hydroxyapatite, a primary component of calcified atherosclerotic lesions, in that way local pharmacodynamics is improved [3].

Regarding antiproliferative drugs, the most used nowadays is Paclitaxel (PTX), due to its high lipophilicity and efficient uptake by and extended retention in vessel walls. Other drugs that have been considered are the ones belonging to the limus-family, such as Sirolimus (SRL) and Zotarolimus (ZLS) [9]. In general, both PTX and limus-family drugs act by arresting cell cycle progression. Their therapeutic effect is mostly related to transportation efficiency and tissue distribution after delivery [9]. PTX, SRL, and ZLS are lipophilic. This means that they can cross the inner hydrophobic core of cell plasma membranes in the endothelium and get transported easily to the arterial wall.

1.3.   Aims of the project

The major limitation of currently available DCBs is the lack of effective control of drug delivery, thus causing drug loss and low efficient therapeutic levels. It has been found that up to 80% of the medication is lost in the bloodstream before the balloon reaches the treatment site [2].
Additionally, the drug is not released fast enough from the balloon to the tissue during the balloon's inflation time. Consequently, only a subtherapeutic level of medication is administered at the treatment site. Therefore, there is a critical need to manage drug delivery from balloons to reduce the amount of medication lost while being transported to the treatment site. Thus, it is crucial to evaluate the mechanical characteristics of the balloon material and the drug coating, in order to understand the loading conditions that may cause the drug to fracture and delaminate from the balloon substrate. However, to understand the working of angioplasty balloons it is first necessary to know their multi-axial mechanical response at various scales. Moreover, the mechanical evaluation of angioplasty balloon materials is essential for ensuring their safety, efficacy, and durability. Only a few previous studies attempted to characterize this polymeric material mechanically, which is why this thesis project started.

The long-term objective of this work is to provide quantitative information on materials used for angioplasty balloons and to develop a better understanding of the mechanical behavior of polymer substrates with and without excipient-drug layers.

The short-term objective of the thesis is to investigate the mechanical properties of the polymer substrates and assess the mechanical integrity of the excipient layer and of the excipient-drug system upon straining the underlying substrates.

The above-mentioned purposes are achieved through in-situ mechanical testing; i.e. uniaxial and multiaxial straining with simultaneous confocal laser scanning of the surface.
The uniaxial tensile tests were performed with an in-house developed loading system, suitably developed for miniaturized samples, from which the material parameters have been obtained. On the other hand, the multiaxial loading is achieved through a bulge loading system, which provided the correlation between the applied pressure and the deflection experienced by the sample.
Finite element simulations with Abaqus/STANDARD are run to validate the experimental results finding a suitable analytic model that describes the material's behavior.

The mechanical tests are carried out on uncoated (polymer substrate only) and coated samples. Uncoated specimens are of two types, including thin films and balloons.

Boston Scientific and L2Mtech provide commercially available Nybax and polyamide balloons respectively, while the University of Montpellier provides the heat-pressed Pebax thin films.

Coated samples, both those with excipient only and those with excipient and drug, are provided by Montpellier University.

2 State of the art

2.1. Balloon materials

Materials that are currently employed in the production of angioplasty balloons are polyvinyl chloride (PVC), polyethylene (PE), polyethylene terephthalate (PET), Nylon (polyamide), reinforced polyurethane (PU), or poly(ether-block-amide) (Pebax ®) [6] [9].

PVC shows a moderate degree of compliance even at nominal balloon inflation pressures. PVC balloons also deform and elongate with increasing inflation pressure [12]. They rupture at significantly lower inflation pressures than balloons composed of other materials [13], [14]. As result, PVC has mostly been given up as a balloon material.

Balloons made of PE are less compliant than those made from PVC. When inflated to the working pressures, they exhibit small diameter increases and minimal deformity [12] [14]. PE balloons have higher burst pressures and almost twice as much dilating force as PVC balloons of the same size [13],[15].

PET gained popularity with its use in small vessel balloon catheters. Balloons made from PET are much less compliant than both PVC and PE balloons and can usually be made with a lower profile. Despite PET balloons having very thin walls, they can withstand very high inflation pressures. However, PET balloons are less scratch resistant than PE balloons in that they tend to perforate more frequently in calcified lesions and stents.

Based on their specific composition, nylon-derivative balloons have variable inflation pressure and compliance characteristics. In general, Nylon balloons are more compliant than those made from PET, but less or similar in compliance to PE balloons. Moreover, they are more scratch resistant than PET and PE balloons, are softer and have proved to be suitable balloons on which to mount stents. Additionally, the deflation profiles of Nylon balloons are typically good [16].
To take advantage of the various properties of balloon materials, the industry has created coextruded copolymers, as well as balloons made of multiple layers of the various polymers [17].
An example is provided by the Conquest and Atlas balloons (Bard Peripheral Vascular, Tempe Ariz.). They have a unique three-layer design. The inner layer is constructed of noncompliant PET material. Around it, ultrahigh-molecular-weight PE fibers are wrapped circumferentially and longitudinally. The PE fibers are affixed to

the inner PET material by an extremely thin covering layer of polyether–block–amide (Pebax) material. As a result, these balloons have a rated burst pressure equal to 30 atm and they are relatively puncture resistant [16].

Another type of multilayer balloon material is NyBax, a coextrusion of Nylon and Pebax thermoplastic elastomer, which is currently used in the Mustang and Coyote Balloon Dilation Catheters (Boston Scientific Corp., Boston) [18]. Like PET, NyBax balloons can tolerate very high inflation pressures, despite being thin-walled. A material with thin walls has a lower profile and generally better sheath performance than a thicker-walled balloon material of the same diameter, meaning that it's easier and smoother for the balloon catheter to be inserted and withdrawn from its protective sheath during the medical procedure. A coextruded balloon made of Nylon and thermoplastic elastomer is also softer and more flexible than one composed only of PET or PE [16].

2.2. Manufacturing process

The most common manufacturing process of angioplasty balloons consists of the balloon-forming technique, a specific blow-molding (Figure 3). It takes place in various stages, starting from polymer granules which are heated and extruded into a tube. These tubes are then blow-molded into angioplasty balloons with the help of heated jaws and compressed air.

The main production steps, can be summarized as follows: (i) during extrusion, the dried granular raw material is fed into a screw-driven and heated extruder with a shaping dye, and then it is extruded into tubes; (ii) while necking, chilled and cropped tubes get stretched into parisons with necked ends; (iii) in the actual balloon forming process, the parison is inserted into a hollow glass mold and heated up to the specific glass-transition temperature Tg while being pressurized [19].

It has been assumed that the morphology of balloon membranes changes several times during the manufacturing process. It often happens that molecular chains of molten polymer tend to align in the machine direction (MD) inside the extruder [19]. Due to the complexity of the production process, the material responses of the balloons are different from the ones of the raw material, because of the intentional reorientation of the crystalline regions and molecular chains of the polymer [19]. Moreover, the characteristics of formed balloons are dependent on the kind of raw material, the extrusion method, and the balloon forming program [20].
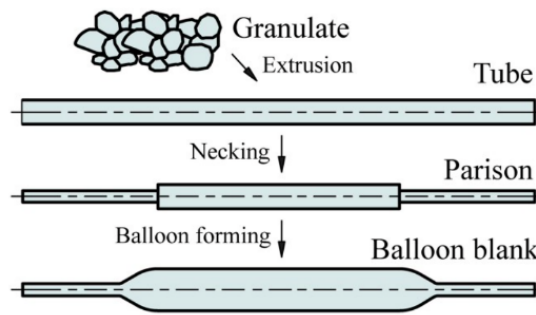
Figure 3: Schematic production cycle of balloon catheter blanks [20].

Blow molding offers several advantages for manufacturing angioplasty balloons, including the ability to produce balloons with consistent size and shape, high production rates, and lower costs compared to other manufacturing methods [21]

Another common method used is heat molding, also known as thermal forming. This method involves heating a sheet of material until it becomes pliable, and then forming it into the shape of a balloon using a mold or die. The balloon is then cooled and trimmed to the desired size and shape [22]. Various benefits come with heat molding, including the ability to produce balloons with a high degree of precision and control over wall thickness, as well as the ability to produce complex shapes. However, this method may be more expensive and time-consuming than blow molding, and it may be more difficult to achieve consistent quality and dimensional accuracy. As a result, heat molding is often used for producing custom or specialized balloons, while blow molding is more commonly used for producing high volumes of standard balloons[21], [22].

2.3. Mechanical evaluation of angioplasty balloon materials

The mechanical evaluation of angioplasty balloon materials is an essential component of ensuring the safety and efficacy of these medical devices. The mechanical properties of the balloon material can significantly impact its ability to perform the necessary functions during the procedure and maintain lumen patency over time. Therefore, it is crucial that these materials are thoroughly evaluated before clinical use.

One of the primary reasons why mechanical evaluation is critical is safety. The balloon material must be able to withstand the mechanical stresses involved in the procedure without rupturing or failing, as this could result in serious harm to the patient. Additionally, the mechanical properties of the balloon material can impact its efficacy. The balloon material must be capable to generate the necessary radial force to dilate

the vessel and maintain lumen patency. If the balloon material cannot do this effectively, the procedure may not be successful [23].

Another important aspect of mechanical evaluation is durability. During the procedure, angioplasty balloons are subjected to repeated inflation and deflation cycles. The balloon material must be able to withstand these repeated cycles without degrading or failing, as this could affect the durability of the balloon and its ability to maintain lumen patency over time.

Finally, regulatory requirements make mechanical evaluation essential. Regulatory bodies such as the FDA require medical device manufacturers to demonstrate that their products are safe and effective. The mechanical evaluation of angioplasty balloon materials is a critical component of this regulatory process and is required to obtain approval for clinical use [23], [24].

Some common mechanical tests used to evaluate angioplasty balloon materials include:

- **Burst Pressure Test**: it measures the maximum pressure that the balloon can withstand before it bursts. A balloon is inflated until it bursts, and the pressure at which it bursts is recorded. This test helps to determine the strength and durability of the balloon.
- **Compliance Testing**: it measures the change in balloon diameter with changes in pressure. Compliance is the ability of the balloon to conform to the shape of the vessel. The compliance test measures the pressure and diameter of the balloon at different inflation pressures. The compliance of the balloon is calculated as the change in diameter per unit change in pressure.
- **Fatigue Testing**: is used to evaluate the durability of the balloon under repeated inflation and deflation cycles. The balloon is inflated and deflated a specified number of times, and any changes in its mechanical properties are recorded. This test helps to determine the lifespan of the balloon.
- **Tensile Testing**: it measures the strength and deformation properties of the balloon material under uniaxial loading. The balloon material is cut into a rectangular strip and pulled in a uniaxial direction until it breaks. The force required to stretch the material is recorded, and the elongation or deformation of the material is measured as well.
- **Adhesion Testing**: is used to evaluate the adhesion strength between the balloon material and the coating or drug on the balloon surface. It measures the force required to separate the coating or drug from the balloon surface.
- **Radial Force Testing**: it measures the force exerted by the balloon on the vessel wall when it is inflated. The balloon is inflated to a specified pressure and the radial force is recorded. This test helps to determine the ability of the balloon to dilate the vessel and maintain lumen patency.

- **Trackability and Pushability Testing**: they evaluate the ability of the balloon to be guided through the vasculature to the target lesion. Trackability measures the ability of the balloon to follow the desired path, while pushability measures the force required to push the balloon through the vessel. These tests help to ensure that the balloon can be navigated through the tortuous anatomy of the vasculature.
- **Abrasion Testing**: is used to evaluate the durability of the balloon material when subjected to friction. The balloon is rubbed against a surface repeatedly, and any changes in its surface properties are recorded. This test helps to determine the wear resistance of the balloon material.
- **Hydrolytic Testing**: evaluates the stability of the balloon material when exposed to water or other fluids. The balloon material is immersed in a fluid and the changes in its mechanical properties are recorded over time. This test helps to determine the biostability of the balloon material.

2.3.1. Uniaxial tensile test

Angioplasty balloon materials have been mostly characterized by focusing on the physical and chemical properties of the material surfaces.

The physical characteristics of the balloon surface that might affect coating adhesion were examined using atomic force microscopy (AFM), transmission electron microscopy (TEM), scanning electron microscopy (SEM), and small-angle X-ray scattering (SAXS) [6].

Emphasis was placed on better defining the morphological features of poly(ether-block-amide) materials. Samples were studied by the techniques of dynamic scanning calorimetry (DSC), wide-angle X-ray diffraction (WAXD), and small angle light scattering (SALS) [25],[26].

Mechanical properties were evaluated by Dynamic mechanical analysis (DMA), and tensile tests [25].

However, there are only a few publications that describe the mechanical behavior of finished balloon catheter membranes composed of polyamide or other polymers under uniaxial extension or biaxial extension [27].

Experimental quantification and modeling of the multiaxial mechanical response of polymeric membranes of balloon catheters are not carried out frequently[27].

Geith *et al.* performed various uni and biaxial extension tests with quasi-static and dynamic loading patterns, using specimens of balloon catheter for coronary interventions. For both small and big stretches in the radial direction, the membrane responds with a noticeably stiffer reaction. In the longitudinal direction, the specimens are extremely ductile, particularly at very small and large stretches, whereas an increase in stiffness is visible in the stretch range 1.02-1.04 [27]. The results are shown in Figure 4.
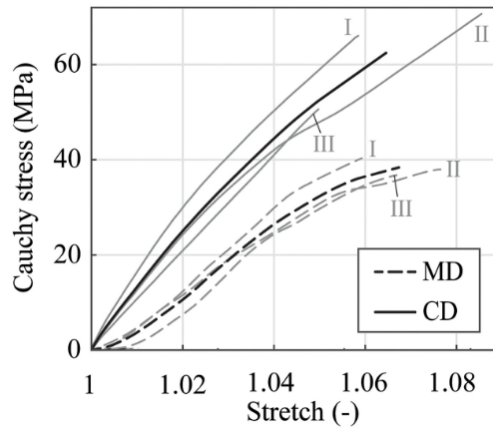
Figure 4: Uniaxial Cauchy stress-stretch relationship in Machine Direction (MD) and Circumferential Direction (CD). The diagram shows the results of respectively three specimens (I, II, III). The bold solid and bold dashed curves represent the corresponding median curves [27].

Sheth *et al.* used the uniaxial tensile test to evaluate the influence of Pebax composition on stress-strain curves [25]. They tested 5 different ratios of hard segments in the material (PEBAX 2533, 3533, 4033, 6333, and 7033). Samples with small quantities of PA segment contents (P2533 and P3533) behave like elastomers; they have a low Young's modulus and an incredibly high elongation at break.

On the other hand, P6333 and P7033 both have a sharp yield point. They display a greater Young's modulus and significantly less elongation at break (Figure 5). Such behavior indicates that the hard phase connectivity of the Pebax materials increases as the PA concentration rises [28].
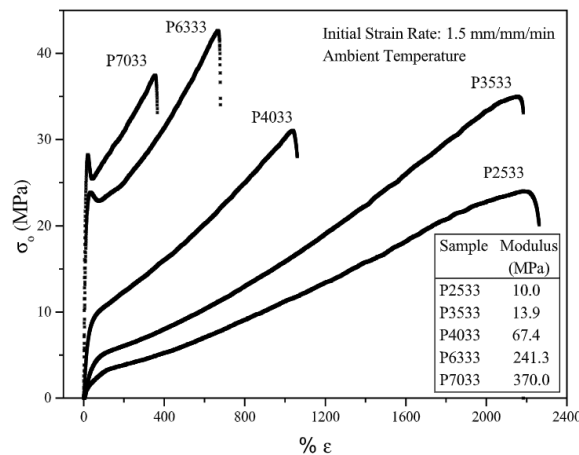
Figure 5: Stress-strain behavior of slowly cooled melt compression molded PEBAX films [29].

Sadeghi *et al.* in 2013 showed, by means of uniaxial stretching test, that physical and mechanical properties of Nylon are related to the degree of polymer stretching [29]. Additionally, they demonstrated a correlation between the stretching ratio and the molecular orientation of polymer chains.

Rhee *et al.* examined the morphology and crystal structure of biaxially stretched Nylon 12, showing that room-temperature aging of Nylon 12 increases the glass transition temperature (Tg) making the samples stiffer [30].

Sadeghi and Le tested both the balloons and tubes made of Nylon-12 and Pebax. Usually, balloons are formed by stretching extruded tubes in both the axial and radial directions using a balloon-forming machine (blow molding). The properties of formed balloons are dependent on the type of material, extrusion process and balloon-forming program [26]. They investigated the differences in the crystalline structure, in the physical and mechanical performance.

By means of tensile tests, it has been found that, overall, the balloon's strength is greater in the radial direction than in the axial direction (Figure 6 (a)). This is useful for biological applications since the radial burst raises the chance of difficulty in balloon removal and is therefore considered a higher-risk failure mode.

Moreover, they observed that Pebax balloons have a hybrid structure made up of hard segments scattered with soft segments and amorphous phases. The hard segments are made of crystalline polyamide that is biaxially oriented in the balloon and has higher radial than axial molecular orientation. As a result (Figure 6 (b)), the radial direction of the material has a higher tensile strength than the axial direction [26].
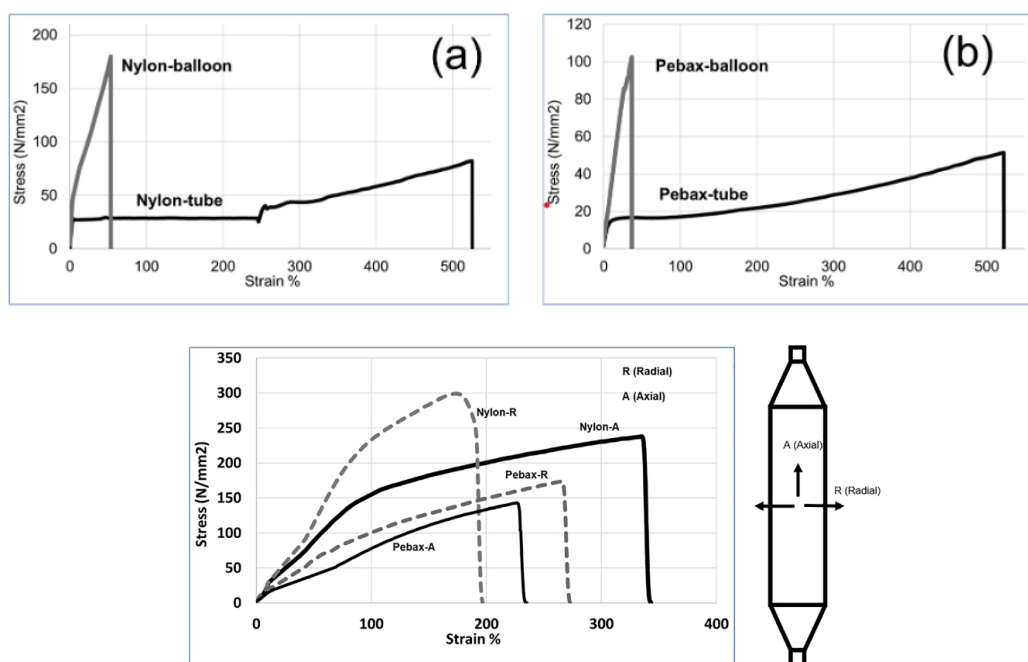
Figure 6: Stress–strain curve for tube and balloon, (b) Stress-strain curve in axial and radial directions [27].

Table 1 shows how the experiments have been carried out by the authors.

Material	Shape	Dimension [mm]	Speed [mm/min]	Ref
Grilamid L25 (Nylon 12)	Tubes	-	127	[26]
Pebax®6333 SA01 MED	Balloons	6×100 (diameter × length)		
PEBAX 2533, 3533, 4033, 6333 and 7033	Dog-bone	2.9 x 0.33	1.5	[25]
Nylon 12	Rectangular	10x4	1	[19]

Table 1: Uniaxial tensile tests performed in literature.

2.3.2. Bulge test

For films that are only a few microns thick, it is particularly challenging to characterize them mechanically. An effective experimental method for evaluating the mechanical properties of thin film samples is the bulge test [31]. However, there is no literature evidence on its use on angioplasty materials.

By applying pressure, either with fluid or gas, to one side of a sample and measuring the resulting deflection, the bulge test can provide valuable information about a material's strength, stiffness, and other mechanical properties from the pressure/deflection relationship according to bulge equations [32].

The purpose of this experiment is to indirectly determine the stress at the apex of the inflated specimen using the thin membrane theory. This theory expresses the relationship between the applied pressure and the stresses in the two main directions also stressing the influence of radius of curvature and material thickness [33]. Consequently, the key step is the conversion from pressure-deflection to stress-strain of the material.

The sample geometry is shown in Figure 7. The central deflection (h) is directly related to the strain experienced by the sample, while the applied pressure (p) is related to stress.
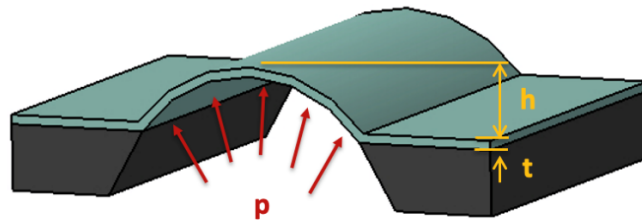
Figure 7: Schematic illustration of bulge test geometry.

The device for performing this type of test generally features a plate that allows the specimen to be attached, a system for pressurization connected to a chamber containing the pressurizing medium, and a system that allows measurement of the applied pressure and displacement of points on the surface of the specimen.

The bulge test is a unique testing method with several benefits above conventional techniques. It is precise, non-destructive, simple, and portable. The sample is clamped along the boundaries of a cavity of a given shape, called bulge window. This can take different geometries: circular, elliptical, rectangular, and square [33].
By tuning the bulging window's shape and size, which determines the specimen's geometry, it can reproduce various kinds of stress and strain states. This makes it a very cost-effective testing method [32].
In the case of using a circular window to test an isotropic material, by increasing the pressure, the specimen swells and assumes a spherical shape that induces an equi-biaxial stress-strain state at the point of maximum displacement [33].

Even in the case of a rectangular window, a biaxial stress state can be obtained however it is no longer equi-biaxial. Additionally, if the ratio of the lengths of the window sides is greater than four, a quasi-plane strain state is obtained, characterized by a uniform, one-dimensional radius of curvature away from the edges. Indeed, the deformation in the short-side direction is relatively large, while the one in the orthogonal direction can be neglected [33], [34].

Elliptical windows behave similarly to the previous ones. An example of the use of this geometry is given in the work of Plancher *et al.* [35] and Jayyosi *et al.* [36].

The square window is not among the most frequently used since it requires a more complex analytical treatment [33]. However, it is used in the work of Trabelsi *et al.* [37] and Romo *et al.* [38].

The system that supplies the pressure for the bulge test is made up of two different types: gas suppliers and liquid providers. To accommodate the higher pressure demands for stiffer materials, liquid suppliers are used. It is more challenging to apply this solution since the filling process for the setup with liquid providers is typically

linked to the problem of air-bubble entrapment, leading to uncertain results. Despite that, the incompressibility of hydraulic systems means that pressurization is slow but stable, making it easily controllable [32], [39].

The pressurization can generally be done in a variety of methods, including the use of a manual valve [36], a syringe [40], [41], a manual sphygmomanometer [42], or a piston pump [37], [38].

Among liquids, water represents one of the most frequently adopted solutions, as it is easy to handle [43], [44]. Alternatively, phosphate-buffered saline is used in some work [41].

The most commonly used pneumatic systems take advantage of air as a means of pressurization [32], [45]. An alternative is also nitrogen, which has the benefits of having low density, requiring low driving force, and allowing rapid membrane deformation [39].

A key element of the setup is the systems for pressure acquisition. Sensors are therefore generally placed within the device, selected based on the maximum pressure being achieved and taking into consideration compatibility with the data acquisition system [46]. As an alternative to sensors, pressure can also be measured using pressure gauges [47].

3 Materials and methods

3.1. Materials

In this section the polymeric materials that have been tested are described. All the specimens evaluated are provided by third parties and they are divided into two main categories: uncoated and coated samples.

3.1.1. Uncoated samples

Name	Origin	Materials	Characteristics
Mustang (long)	Boston Scientific	NyBax®	**Long unfolded balloons** length: 60 mm - 200 mm diameter: 5 – 10 mm
Mustang (short)	Boston Scientific	NyBax®	**Short unfolded balloons** length: 20 mm - 60 mm diameter: 5 – 10 mm
Mustang	Boston Scientific	NyBax®	**Folded balloons**
Flexitrack	L2M Tech	Polyamide (Nylon)	**Folded balloons** length: 150 mm diameter: 3 mm
Pebax film	University of Montpellier	Pebax®	**Heat-pressed films** size: 74 mm x 74 mm

Table 2: Uncoated samples tested.

Pebax films

Pebax® is a thermoplastic poly-(ether-block-amide) that consists of linear chains of hard polyamide (PA) blocks covalently linked to soft polyether (PE) blocks via ester groups. The molecular weight of the PE blocks varies from approximately 400 to 3000 g/mol, while that of the PA blocks ranges from about 500 to 5000 g/mol [25].

Different types of nylons, such as Nylon 6, Nylon 11, and Nylon 12, have been employed as the PA block. On the other hand, PE block has been constituted by PTMO, polypropylene oxide (PPO), or polyethylene oxide (PEO).

The morphology of the Pebax® balloon surface consists of hard segments dispersed in soft segments and amorphous phases, as shown in Figure 8. The hard segments are crystallized polyamides that are biaxially oriented in the balloon, with a predominant molecular orientation in the circumferential direction. This leads to a higher tensile strength along the radial direction than the axial direction for the balloons [20].
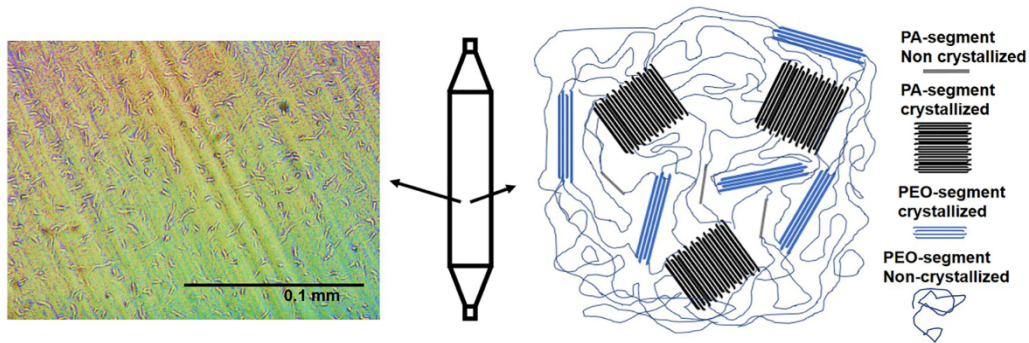
Figure 8: Optical microscopy of the Pebax balloon surface at magnification of 40x.

Pebax films provided by the University of Montpellier are heat-pressed and have a squared shape (74mm x 74mm). It has been tested by cutting small samples from several regions along the whole surface (Figure 9).

Figure 9: Pebax film - University of Montpellier.

Unfolded balloons

Boston Scientific supplied Mustang balloons made of Nybax. This material consists of a co-extrusion of Nylon and Pebax, where Nylon provides flexibility, while Pebax imparts strength, resulting in a lower profile and high-rated burst pressure. For the sake of simplicity during the experimental phase, the Mustang unfolded balloons have been grouped on the basis on their length: long balloons (60 mm - 200 mm) and short balloons (20 mm - 60 mm).

Long balloons (Figure 10) were tested in three different points, namely at the center and at the two apexes, on either side. It is imperative for the samples to be collected from regions where the balloon was not held during manufacturing, as gripping can produce grooves on the surface of the balloon.

Figure 10: Mustang unfolded long balloon - Boston Scientific.

Short balloons (Figure 11) were tested in the center part, on both sides, avoiding the lines due to the manufacturing process.

Figure 11: Mustang unfolded short balloon - Boston Scientific.

Folded balloons

Folded balloons are provided by Boston Scientific (Figure 12) and L2MTech (Figure 13). The folding process involves wrapping the balloon around a catheter shaft, which is connected to the guiding wire outside the balloon. To extract the samples to be tested from the folded balloons, they need to be primarily unfolded with a pressure of 1-3 atm using an inflation pump.

Figure 12: Mustang folded balloon - Boston Scientific.

Figure 13: Flexitrack folded balloon - L2MTech.

3.1.2. Coated samples

These sample types have Pebax film as substrate and coating on top of it (Table 3).

Origin	Coating	Coating method
University of Montpellier	Polymer (Pluronic P123)	Spray-coating
University of Montpellier	Polymer (Pluronic P123)	Micro-pipetting
University of Montpellier	Polymer + drug (Pluronic P123 + Everolimus)	Spray-coating

Table 3: Coated samples tested.

The coated samples are provided by the University of Montpellier. They consist of a Pebax substrate on which the coating is deposited by the spray-coating or micro-pipetting technique. The coating solution can either be only the excipient (Pluronic 123), as shown in Figure 14; or an excipient matrix with a drug embedded in it (Pluronic123 + Everolimus) in Figure 15. In both cases, 5 ml of coating solution is used to cover the whole sample's surface ($2374,625$ mm^2). The tested sample has an area of $3,14$ mm^2; so, under the assumption of homogeneous thickness of the coating, there is $0,0066$ ml of excipient on it.

Pluronic P123 is a symmetric triblock copolymer comprising poly(ethylene oxide) (PEO) and poly(propylene oxide) (PPO) in an alternating linear fashion, PEO-PPO-PEO. The nominal chemical formula of P123 is $HO(CH_2CH_2O)_{20}(CH_2CH(CH_3)O)_{70}(CH_2CH_2O)_{20}H$, which corresponds to a molecular weight of around 5800 g/mol. Triblock copolymers based on PEO-PPO-PEO chains are known generically as poloxamer.
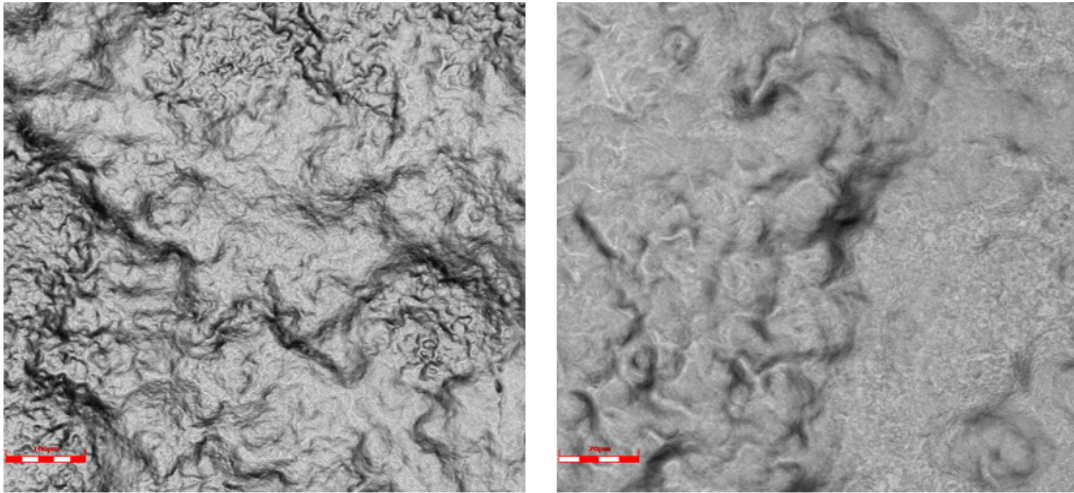
Figure 14: Polymer (Pluronic 123) coated Pebax film - University of Montpellier
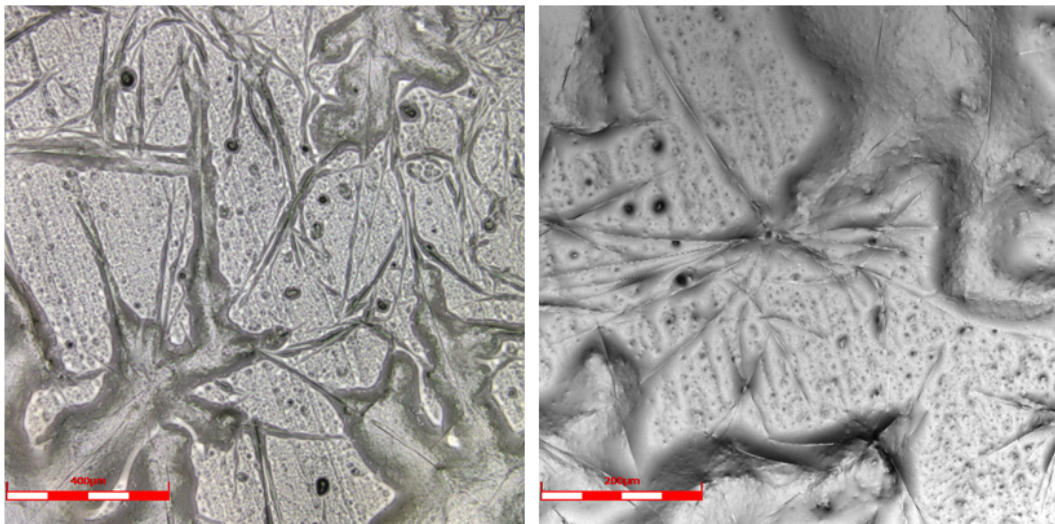
Figure 15: Drug-polymer (Pluronic 123 + Everolimus) coated Pebax film - University of Montpellier.

3.2. Methods

Polymeric membranes are tested in two configurations: uniaxial and biaxial.

The uniaxial tensile test is performed in order to evaluate mechanical properties of the materials. The main goal is to find the analytic model that better describes the specimen behavior under uniaxial loading. Using the stereomicroscope, it was possible to evaluate the sample's stretch during the test. Moreover, it is useful to determine whether the material is isotropic or not, testing it in both axial and circumferential directions [20].

The bulge test is used to carry out the biaxial loading. The material is inflated with water, and the vertical deflection of the sample in proportion to the applied pressure is assessed using a confocal laser microscope. Once again, the material isotropy is investigated, but this time in relation with the applied pressure [48].

All the experimental data are then used to carry out finite element simulations of the bulge test.

3.2.1. Uniaxial testing

3.2.1.1. Setup

Uniaxial tensile tests have been performed using the micro-biaxial machine (μBTM) in uniaxial configuration (Figure 16). It has two 15 mm translational stages, a DC gear motor, and a high-resolution encoder (M-111-1DG1, 200 nm motion resolution, Physik Instrumente, Karlsruhe, Germany). A load cell of 50 N maximum load and 0.1% of nominal sensitivity (model 8417- 5050, Burster) has been used to measure the force [48].

The samples have been subjected to two opposite longitudinal displacements in order to keep the central part of the sample in a steady position during the test below the objective of a stereomicroscope. This allows the recording of a real-time video of the test execution. As a result, the analysis of the material's stretch can be performed.

The samples have been tested along the circumferential and axial directions with a displacement rate of 0.01 mm/sec.

LabVIEW, a programming language developed by National Instrument, is the control software employed.
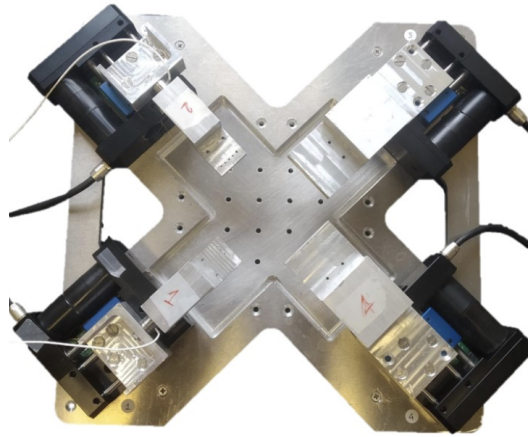
Figure 16: Micro-biaxial machine (µBTM).

3.2.1.2. Experimental protocol

Here, the experimental protocol is explained step by step.

1. <u>Sample preparation</u>: a scalpel has been used to cut the balloon cross-sectionally and shape it into a rectangular sample of size 7 mm x 23 mm (Figure 17).
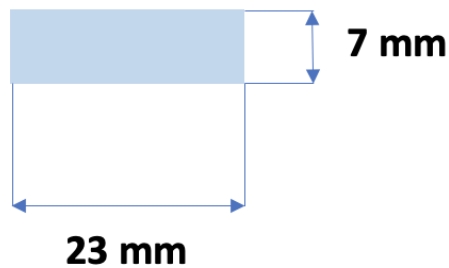
Figure 17: Schematic illustration of the sample.

2. <u>Markers' representation</u>: four markers are drawn on the sample to calculate the Poisson's ratio (Figure 18).
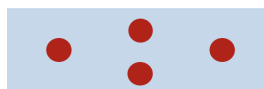
Figure 18: Schematic illustration of the sample with markers.

3. <u>Sample mounting</u>: the sample is glued to the cantilevers for a length of 5 mm on each side (Figure 19). The amount of glue on each cantilever should be sufficient to attach the specimen, but not excessive to propagate within it.
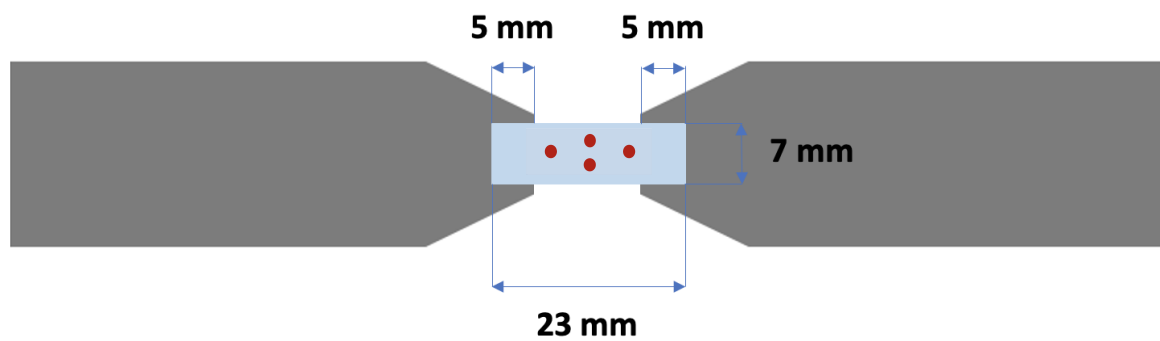
Figure 19: Schematic illustration of the sample on the cantilevers.

4. <u>Machine parameter set</u>: the displacement on both stages is set: the final position is the maximum allowed and the displacement rate of each is 0.01 mm/s.
5. <u>Focusing the specimen with the microscope</u>
6. <u>Beginning of the test</u>: the test and microscope's video recording start simultaneously.
7. <u>Execution of the test</u>
8. <u>End of the test, disassembly</u>

The final setup is shown in Figure 20.
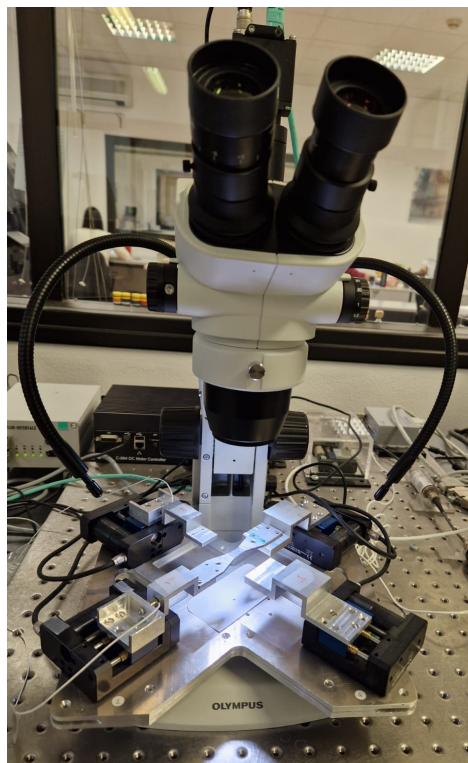
Figure 20: Biaxial machine placed under the stereomicroscope (SZ61 Olympus).

3.2.1.3. Data analysis

After conducting the uniaxial test, a *.txt* file is generated, containing M_1 [mm] and M_2 [mm], which are the displacement of the cantilevers, and C_1 [N], which represents the recorded force.

As the samples exhibited wrinkling in the initial configuration, the force displacement data were selected only above a cut-off threshold value for the measured force. The force threshold is set to 0.1 N. This cut-off is performed in the post-processing phase carried out using a suitably developed MATLAB® script. The total displacement is then calculated by summing the individual cantilever displacements.

Using the force and displacement values obtained from the uniaxial test, engineering stress, strain and Poisson's ratio values are calculated. These are then utilized for theoretical analysis of the material behavior and as an input for the consecutive equations to derive the material parameters.

The video recording through the stereomicroscope allows to capture the performance of the test (Figure 21). Using Fiji software, the video has been transformed into a set of frames. After that, the distance between the barycenters of the markers for each frame has been calculated with a MATLAB® code. By making the ratio between the deformation of the markers in the transverse direction and that in the longitudinal direction, Poisson's modulus has been obtained, using the formula:

$$\nu = -\frac{\varepsilon_{trasv}}{\varepsilon_{long}}$$
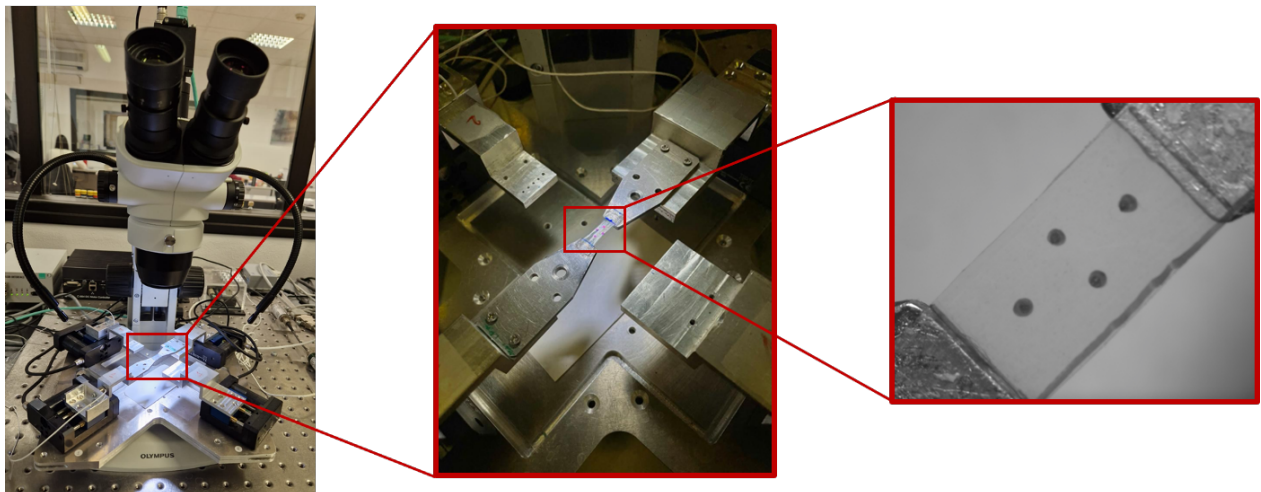
Figure 21: Markers' representation on the sample to analyze the stretch.

3.2.1.4. Yeoh hyperelastic constitutive model

In general, the behavior of hyperelastic materials is expressed in terms of strain energy function. Currently, there are over 40 different constitutive models available, including the Mooney-Rivlin model, Yeoh model, Arruda-Boyce model, Ogden model, and Neo-Hookean model, which are widely used. After an initial screening, among all the analytical models present in the literature, Yeoh model has been chosen for this work, as it is the most suitable and simple.

The Yeoh model is a hyperelastic material model used to describe the mechanical behavior of elastomers, rubbers, and other soft materials, under large deformations. It is based on the strain energy function that relates the deformation of the material to the stress it generates. The Yeoh model uses a series expansion of the strain energy function in terms of the principal invariant I_1 of the strain tensor, and it can be tailored to fit experimental data for a specific material [49].

The hyperelastic strain energy density function of Yeoh model is defined as follows:

$$W = C_1(I_1 - 3) + C_2(I_1 - 3)^2 + C_3(I_1 - 3)^3$$

where I_1 is the first strain invariant, and C_1, C_2, C_3 are the material parameter of the model whose unit is MPa.

The Yeoh model is a third-order polynomial expansion of the strain energy function, which makes it a relatively simple and computationally efficient model compared to other hyperelastic models that use higher-order polynomial expansions.

The values of C_1, C_2 and C_3 in the Yeoh model can be determined by fitting the model to experimental data. Typically, they are obtained by using regression analysis to fit the model to stress-strain data from uniaxial tension tests or other types of mechanical tests. They depend on the material properties of the elastomer being studied, such as the crosslink density, the degree of strain-induced crystallization, and the presence of filler particles. These parameters can also vary with temperature and strain rate, so it is important to determine them under the specific conditions of interest.

The first term in the equation represents the linear elastic response of the material, while the second and third terms capture the nonlinear behavior at higher strains.

In detail, C_1, represents the coefficient of the linear term in the strain energy function, which reflects the material's resistance to stretching or compression and it is related to the initial shear modulus [49].

C_2 represents the coefficient of the quadratic term in the strain energy function, which reflects the material's nonlinear strain stiffening or softening behavior. This term captures the fact that the material's resistance to deformation may change as the deformation increases [49].

C_3 represents the coefficient of the cubic term in the strain energy function, which reflects the material's higher-order nonlinear behavior. For some materials, the value

of C_3 may be negligible, and the model reduces to a second-order polynomial expansion, which is known as the Ogden model [49].

Once force and displacement values are obtained from the uniaxial test, analytic calculations are done in order to obtain the material parameters.

For uniaxial extension in the n_1-direction, the principal stretches are $\lambda_1 = \lambda$, $\lambda_2 = \lambda_3$.

Under the hypothesis of incompressibility $\lambda_1\lambda_2\lambda_3 = 1$, hence $\lambda_2^2 = \lambda_3^2 = \frac{1}{\lambda}$.

Therefore, $I_1 = \lambda_1^2 + \lambda_2^2 + \lambda_3^2 = \lambda^2 + \frac{1}{\lambda}$ (1)

If the directions of the principal stretches are oriented with the coordinate basis vectors, one has:

$$\sigma_{11} = -p + 2\lambda^2 \frac{\partial W}{\partial I_1} \qquad (2)$$

$$\sigma_{22} = -p + \frac{2}{\lambda} \frac{\partial W}{\partial I_1} = \sigma_{33} \qquad (3)$$

Since $\sigma_{22} = \sigma_{33} = 0$, making a substitution one gets:

$$p = \frac{2}{\lambda} \frac{\partial W}{\partial I_1} \qquad (4)$$

Therefore, combining (2) and (4)

$$\sigma_{22} = 2\left(1 + \frac{1}{\lambda^2}\right) \frac{\partial W}{\partial I_1} \qquad (5)$$

The engineering stress is:

$$T_{11} = \frac{\sigma_{11}}{\lambda} = 2\left(\lambda + \frac{1}{\lambda^2}\right) \frac{\partial W}{\partial I_1} = 2\left(\lambda + \frac{1}{\lambda^2}\right)\left[C_1 + 2C_2(I_1 - 3) + 2C_3((I_1 - 3)^2)\right] \qquad (6)$$

One can calculate λ from the uniaxial tensile test results since L_0 is the initial length and d is the displacement of each cantilever:

$$\lambda = \frac{L_0 + 2*d}{L_0} \qquad (7)$$

The analytic force is calculated as:

$$F = T_{11} * A \qquad (8)$$

where A is the cross-section of the material sample. In this case, A is given by the side

(6 or 7 mm) and thickness (0.05 mm) of the sample.

The method used to evaluate Yeoh parameters describing the material during the uniaxial tensile test is obtained by minimizing the error between the experimental force F_e and the analytic force F.

$$Err = \sum (F_e - F)^2 \quad (9)$$

where is obtained from the uniaxial test and F_{11} is obtained using (8).

Using the solver Excel tool, one can get the best possible fit of the force-displacement curves and get C_1, C_2, and C_3 values that give the minimum error. These parameters have evidence only for uniaxial tensile tests, but not for a biaxial loading type. Therefore, they are used as a starting point to check the accuracy of Yeoh model in bulge testing. Several finite element simulations are run in order to find the parameters' triplet most suitable for describing material inflation.

3.2.2. Bulge test

In this work, during the bulge test, the balloon sample is bonded to a metal cap, which has a circular window in the center that exposes the material to the loading. A differential hydraulic pressure is applied from below using an inflation device. The shape of the deformed material is captured using a confocal laser microscope (LEXT OLS4100, Olympus®), and the image is post-processed using MATLAB® for pressure-deflection analysis.

The deformed material is assumed to exhibit a spherical shape and experiences approximately equibiaxial tensile stress and strain.

The bulge test has been performed on both uncoated and coated samples.

3.2.2.1. Setup

In this section, the setup used for the bulge test is presented.
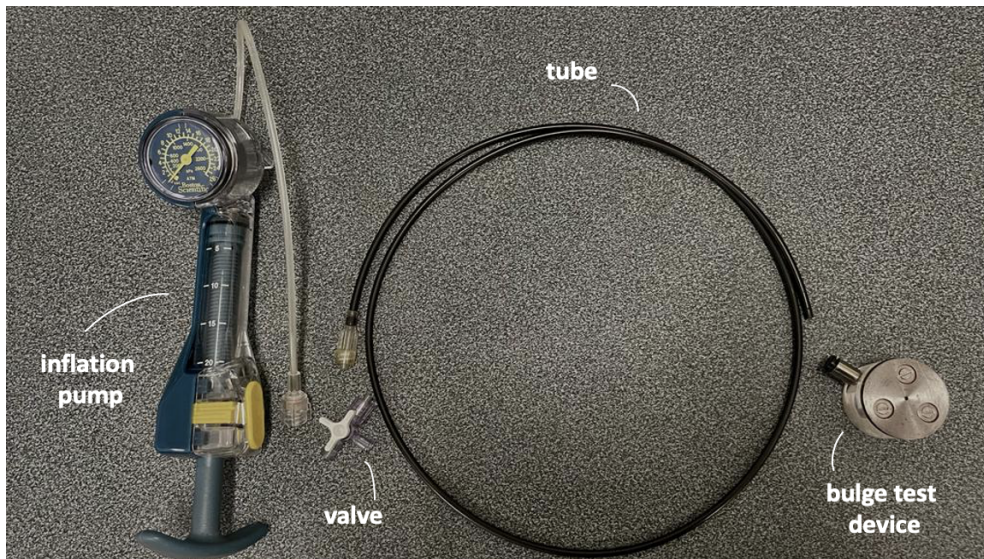
Figure 22: Bulge test setup.

The bulge test setup, shown in Figure 22, is composed of a pressure delivery system and a bulge test device. To ensure constant pressure, an inflation pump supplied by Boston Scientific is used.

The linkage system comprises a tube that connects a plastic valve and the bulge device. In turn, the valve is connected to the inflation pump too. In this work, water has been chosen to apply pressure for the inflation of the balloon during the procedure.

The device itself is composed of a cylindrical chamber, which is shown in Figure 23, and a metal cap.
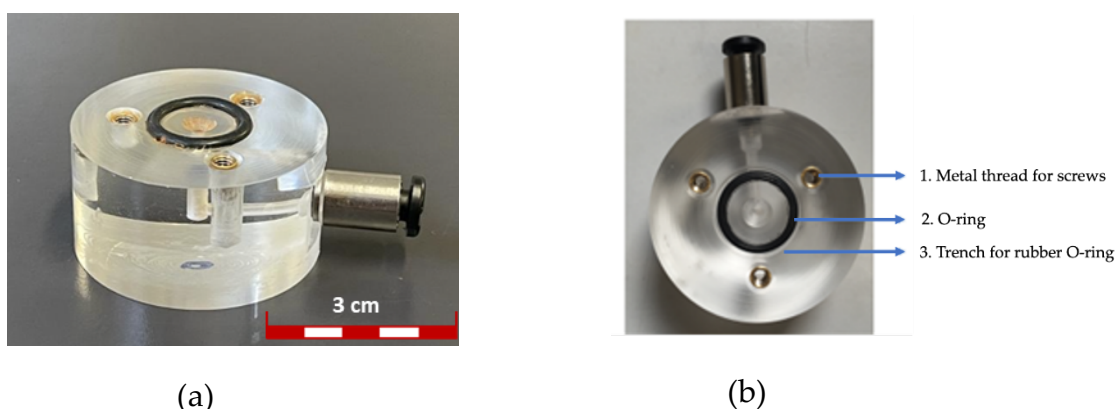
Figure 23: Main body of the bulge test device: front view (a) and top view (b).

PMMA, which is a cost-effective and easy-to-manufactured polymer, is used to fabricate the device. The main body of the device includes several components: an air chamber, a trench and O-ring, metal thread for screws, and a connector for tubes (Figure 23 (b)).

Two orthogonal cavities created with a 2 mm drill tip are intersected to create the air chamber in the center. Since the sample is mechanically confined by the metal cap, the air chamber does not have a size restriction. However, the chamber should be as narrow as possible to have more effective pressure build-up.

The base of the cylindrical chamber links to a rapid-fix pneumatic metal connector, featuring an O-ring on the thread, which provides excellent sealing.

To achieve conformal and tight contact (and subsequently sealing) between the connector and the device wall, a trench and a threaded hole are manufactured in the PMMA main body.

An O-ring is placed in a trench that is created outside the air chamber to improve sealing ability. The trench should be half of the O-ring thickness in-depth, and slightly smaller than the O-ring in diameter and width.

While the O-ring is being set, it should be stretched spherically and compressed along the width in order for it to be set in place.

The O-ring needs to be severely squeezed when the cap is fixed on top, and there shouldn't be any space between the cap and the device.

The threads on the screws were first obtained directly in the PMMA main body, however, after tightening and loosening the screws several times, the threads got significantly damaged. Therefore, a threaded metal sleeve was employed to improve the device's reliability concerning the task of fixing and unfixing the cap (Figure 23 (b)).

The metal cap has three trenches for washers to enhance a tighter seal between the screw head and the cap itself. The central holes of the washers are shaped slightly

conically to fit the conical screw heads and make them disappear below the surface of the cap when fixed, creating an even greater seal. The type of screws used in the device determines the outcome (Figure 24). In this work, conical-headed screws had been selected.

Figure 24: Metal cap (on both sides), washers, screws.

A schematic illustration of the alignment of screws, washers, and the metal cap is shown in Figure 25.
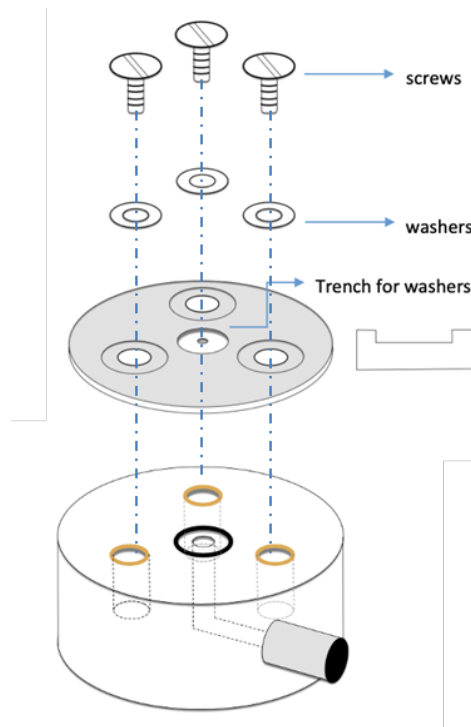
Figure 25: Schematic illustration of the alignment made up of the screws, the washers, and the cap.

The cap is made from a piece of metal, which is less than 2 mm thick. An opening blind cavity is fabricated in the central region of the cap to reduce the depth from the top to

the specimen, so that the device is suitable for experiments with equipment operating at a relatively close working distance with respect to the surface of interest, such as the laser profilometer and the optical microscope.

Since the laser profilometer has a working distance below 1.5mm, the opening is intentionally sloped to allow the laser head to get closer to the specimen without hitting the outer ridge fringe.

The decision to use metal over PMMA is based on the demand that the cap thickness is relatively thin in the area where the sample is clamped to meet the before mentioned requirements. As a result, using metal ensured higher stiffness of the constraint as compared to that of the sample (despite the slender geometry of the constraint). Another reason metal was chosen is to ensure compatibility with the screw head, otherwise, the cap would melt after a few times of use.

Although they exist in different shapes and sizes, the metal cap chosen for this work has a circular window of 2 mm.

Specimen preparation and mounting

The balloon sample is previously cut into circular shape samples with the help of 5 mm diameter leather stamps (Figure 27 (c)). The specimen configuration includes a 3-layer sandwich structure: 3 mm tape - sample - 2 mm tape (Figure 26). First, the 3 mm tape is mounted on the backside of the metal cap. Then, the balloon sample is applied over it, followed by the application of 2 mm tape. This configuration was chosen to ensure the balloon's grip on the metal plate and to prevent any leak due to high pressure being applied.
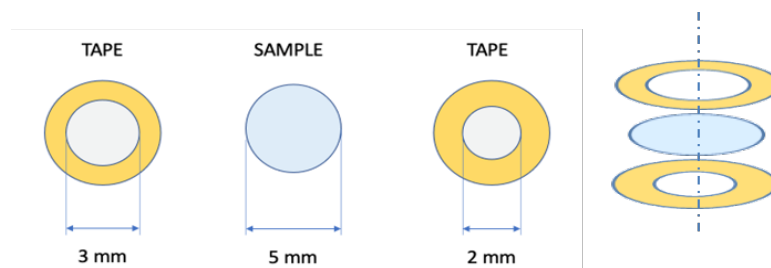
Figure 26: Schematic illustration of specimen configuration.

The tape is a double-sided tape (Figure 27 (a), (b)), where, in the case of the 3mm tape, the top side is for adhesion to the cap and the bottom side is for sticking the balloon sample. Both the central hole and the larger, external concentric circle are obtained by laser cutting.

(a)   (b)   (c)
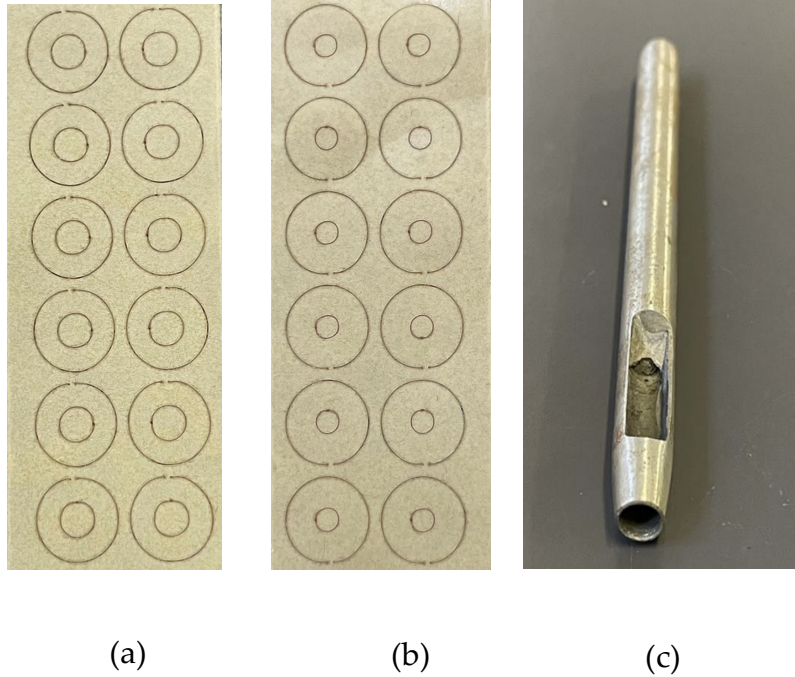
Figure 27: 3 mm tape, 2 mm tape, and 5-mm leather stamp.

After mounting the sample on the metal cap in the configuration mentioned above, the cap itself is mounted on the device and secured with screws.

The pump is filled with water. In this step, it is crucial to make sure that there are no air bubbles inside the pump itself.

After that, the valve is connected to the pump and the plastic tube, which in turn is connected to the device. At this point, the pressure is raised to 1 atm (not *always*) and the entire system is placed under the microscope.

Microscope

The sample under examination is analyzed using a confocal laser microscope (LEXT OLS4100, Olympus®) (Figure 28) to determine the out of plane displacement field caused by the inflation of the membrane. The use of LEXT does not require careful preparation of the specimen and the images can be obtained immediately after the sample is placed on the specimen-holding plane of the microscope itself. In addition, this device allows observation of the surface of interest without coming into contact with it, thus avoiding possible damage to the specimen.

Figure 28: Confocal laser microscope (LEXT OLS4100 Olympus®).

The objective selected for the acquisitions is the 20x, characterized by a working distance of 1 mm and a field of view (FOV) of 640 µm. The magnification is in the range of 432x – 3.456x.

The operation of the confocal laser microscope is to identify two planes along the vertical direction, bottom (lower level) and top (upper level), that bound the volume being scanned in the z-direction. This volume is scanned discretely by n planes in N steps between the two defined levels. The number of planes depends on the selected target and a scan parameter. The latter allows the selection of the separation distance between the n planes according to the desired level of accuracy.

In this thesis work, the acquisition procedure was characterized by a scan parameter of 0.8 µm. The choice was dictated by the need to find the right compromise between the quality of the acquisitions and the time required to perform them.

In addition to the upper and lower limit settings, the system allows the appropriate brightness level to be set according to the image to be captured, enabling height measurements without distortion of the image due to light intensity [50]. Moreover, it allows capturing points where the angles created between the sample and the metal cap are greater than the laser reflection angle of 85 degrees.

During the acquisition, the microscope extrapolates, for each point, the height in the scan volume to which the laser reflection peak corresponds. As a result, the 3D profilometry of the sample surface is obtained.

Considering the scanning procedure performed in this thesis work, using the 20x objective lens, the resolution in the vertical direction is 0.05 µm, while the ones in the

plane of the sample are equal to 0.625 μm.

To extract enough data to describe the behavior of a significant portion of the tested specimen, it is necessary to acquire an area larger than the field of view of the selected objective. To accomplish this, the stitching technique is applied, which entails the acquisition and subsequent merging of a sequence of images in order to have a larger single image with the same resolution as the individual ones.

Considering an overlap of the individual images equal to 10% of the FOV, the balloon surface that is acquired by the stitching procedure has dimensions of approximately 2.35 mm × 2.35 mm.

At the beginning of this work, stitching was performed on a 4 × 4 matrix, which was defined before starting the acquisitions and remained unchanged until the end of the test. However, the process of acquiring the area of interest for each pressure value takes about 25 minutes, for a total of about 6 hours, considering 14 pressure values. Therefore, as a matter of time, stitching with a 2 x 2 matrix has been chosen, which takes about 5 minutes for each acquisition.

It should be kept in mind that the acquisition time is not constant, but it increases with increasing pressure levels. This is due to the fact that the bottom is identified during the first acquisition and is no longer changed; in contrast, the top increases as the specimen is inflated.

In order to hold the device in place throughout the acquisition procedure, a stabilizer has been used, which is shown in Figure 29. In this way, tilting was introduced, but it has been corrected during the post-processing with MATLAB® (Section 3.2.2.3).
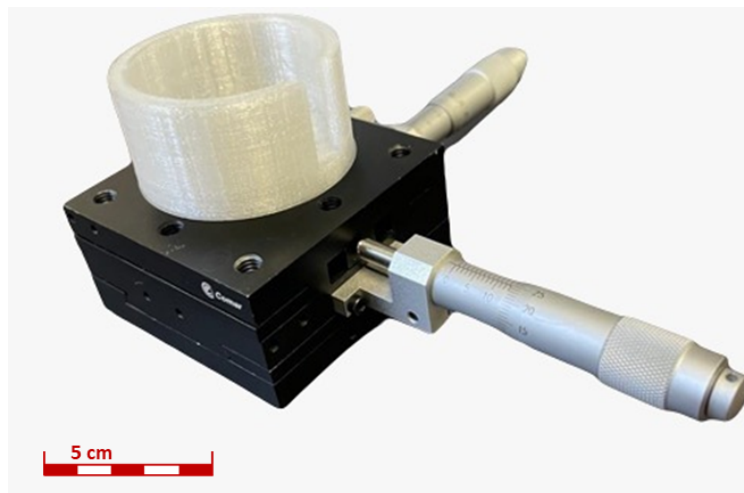
Figure 29: Stabilizer used to hold the device.

The pressure has been increased with each acquisition, to a maximum pressure of 14 atmospheres. Lower values have been reached in some cases, due to water leakage or sample rupture.

3.2.2.2. Experimental protocol

Here, the experimental protocol to perform the test is explained step by step.

1. <u>Sample preparation</u>: the balloon sample is cut out into a circular shape with a diameter of 5 mm.
2. <u>Sample mounting</u>: the sample is attached using bio-adhesive tapes to the metal cap of the device.
3. <u>Filling the pump</u>: the pump is filled with water. In this procedure, it should be checked that no air bubbles are formed inside the pump itself.
4. <u>Connecting the setup</u>: the pump is connected to the plastic valve. This is linked to the connector tube, which in turn is connected to the device. In this step, it must be checked that water flows out continuously, without interruption due to the presence of air bubbles.
5. <u>Mounting the device</u>: the metal cap is put on the device and the screws are tightened.
6. <u>Achieving initial pressure</u>: the pressure is raised from 0 atm to 1 atm.
7. <u>Mounting of the stabilizer</u>: the device is inserted into the stabilizer to minimize movement while performing the test.
8. <u>Placement of the setup under the microscope </u>(Figure 30).

Figure 30: Experimental setup under the microscope.

9. <u>Acquisition of the initial configuration</u>: stitching is performed on a 4 × 4 matrix (Figure 31). For each pressor increment, about 3 minutes should be waited between inflation and acquisition to ensure stabilization of the viscoelastic phenomenon.
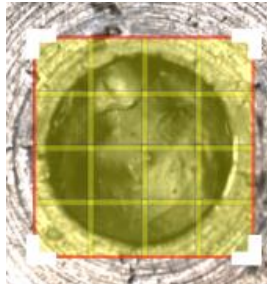
Figure 31: Stitching with a 4 x 4 matrix.

10. <u>Acquisition of the configuration at different pressure levels</u>: for subsequent acquisitions, stitching is performed on a 2 × 2 matrix as a matter of time (Figure 32). After each acquisition, the pressure is given a constant increment of 1 atmosphere until the maximum achievable pressure is reached (14 atmospheres).
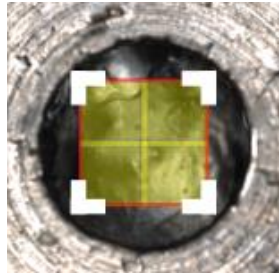
Figure 32: Stitching with a 2 x 2 matrix.

11. <u>Removal of the device from the microscope, emptying, and disassembly</u>.

The bulge test has been performed both on uncoated and coated samples. The only difference in the experimental procedure is that in the latter, glue is used between the tape and the specimen to ensure their attachment.

3.2.2.3. Data analysis

For each acquisition made with the microscope, a CSV file containing a matrix of values is saved. The first row and first column represent the x and y coordinates of the points, respectively, and for each coordinate pair, the corresponding value of the vertical displacement in z is found within the matrix.
These data are then analyzed using a MATLAB® script that allows the point cloud, representing the displacement, to be fitted with a grid.

The stabilizer, not being perfectly flat, introduces a tilt into the captured image (Figure 33, left column). Therefore, before proceeding with surface interpolation, it is

necessary to correct the tilt. First, the image is corrected with the OLS4100 Lext software, using a specific function that allows the selection of three points belonging to the metal part of the device on the captured image (Figure 33, right column).
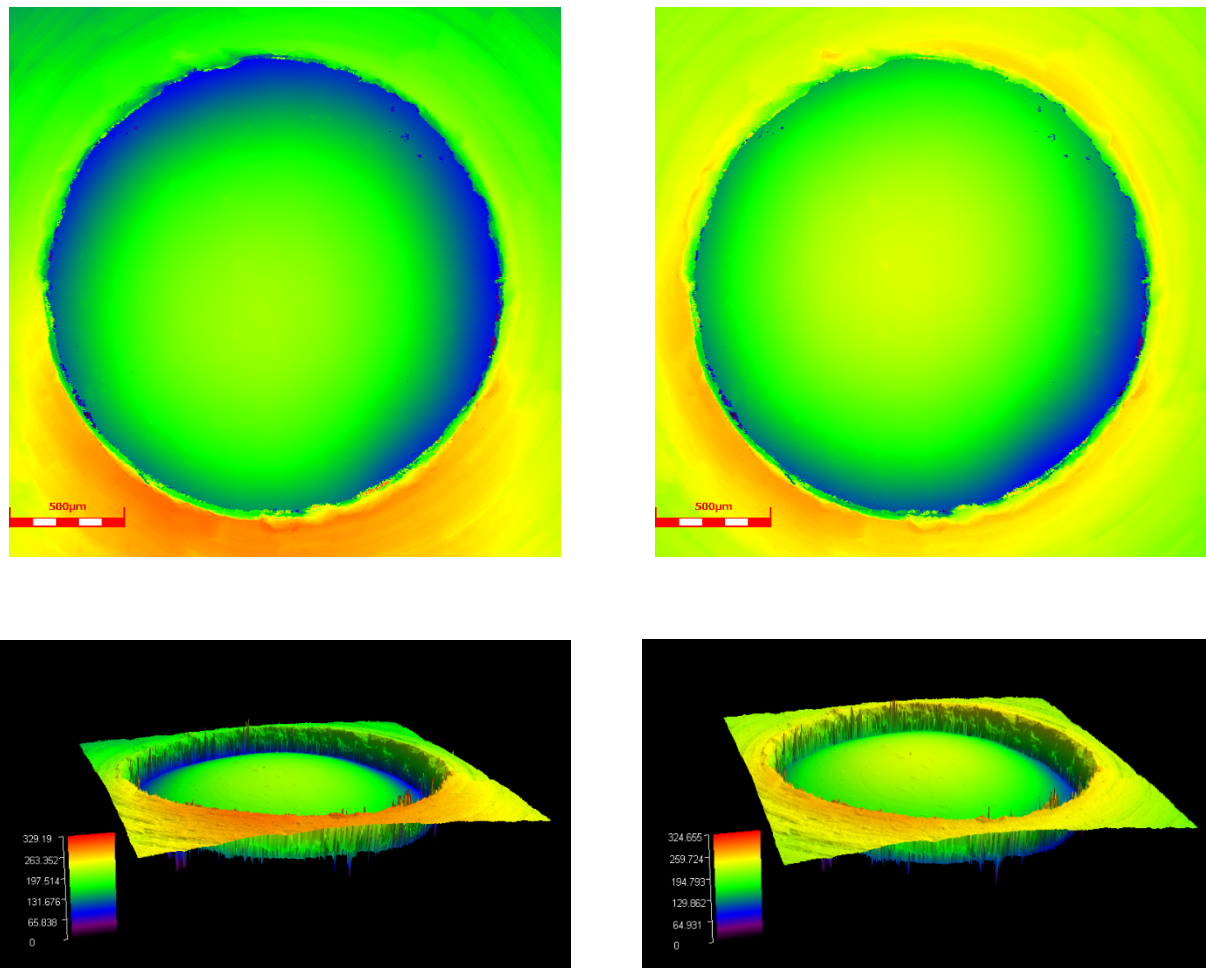
Figure 33: 2D surface (top) and 3D surface (bottom); left column: surface non-corrected; right column: surface corrected using three-point correction.

However, this can only be done for the first acquisition, where the matrix is large enough to include the metal, while it cannot be done for successive acquisitions, having used a smaller matrix.

Using MATLAB's `pcregistericp` function, it is possible to find a rotation matrix and translation vector that correlates the tilted image with the microscope-corrected image (Figure 34). The transform is then applied to all subsequent acquisitions.
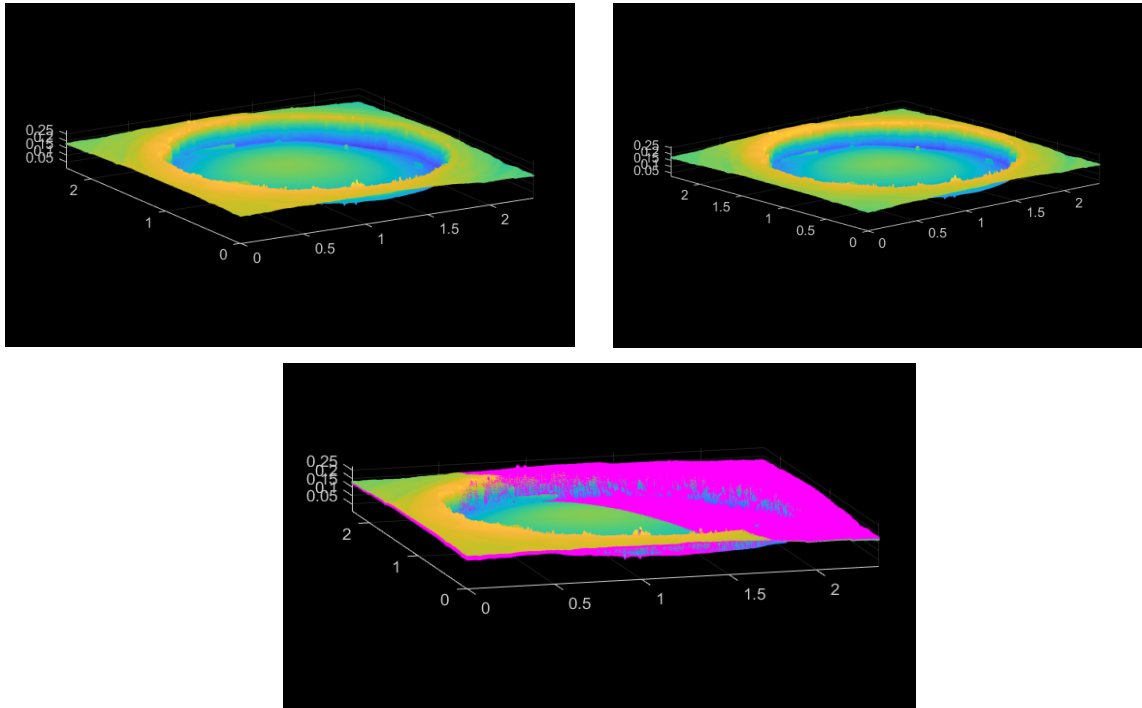
Figure 34: Surface non-corrected (left), surface corrected (middle), superposition of corrected and non-corrected surfaces (right).

The data in the files obtained from the microscope are fitted with a square grid, defined by 101x101 nodes, using the MATLAB® function `gridfit`. It is a surface modeling tool, fitting a surface of the form z (x, y) to scattered (or regular) data. As an example, the displacement map at initial pressure and maximum pressure reached is shown in Figure 35(a) and 35(b). Then, in Figure 36, it is presented the same experimental surface fitted in MATLAB®.

(a)

(b)
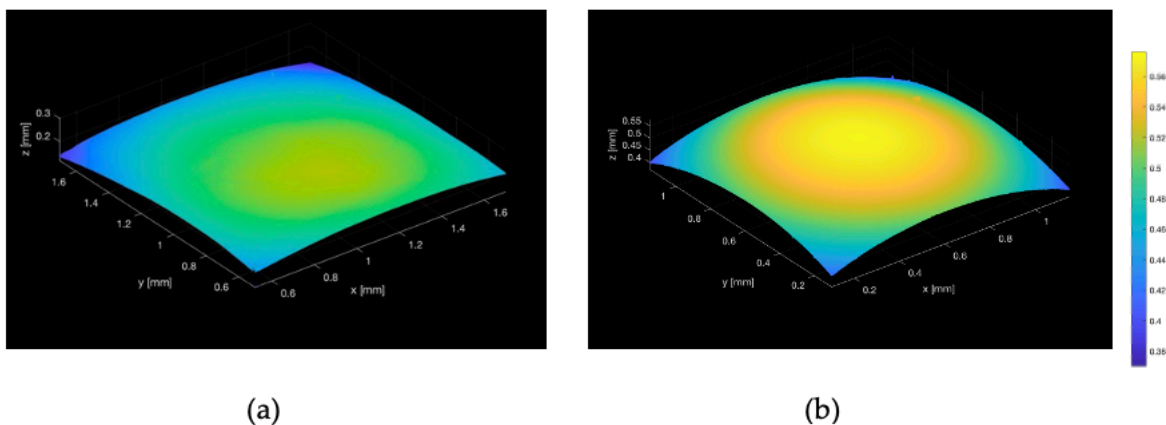
Figure 35: Color map of the displacement along vertical direction z (a) 1 atm (b) 14 atm.
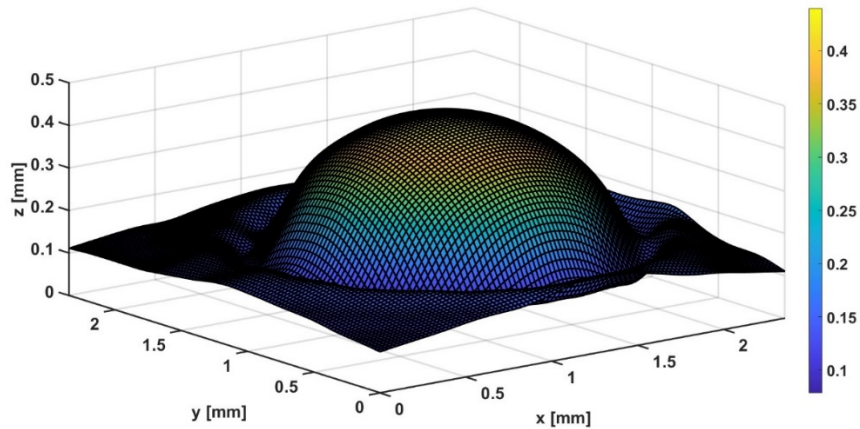
Figure 36: Color map of the displacement along vertical direction after grid fitting.

In order to avoid the metal part during curvature and maximum deflection calculations, the grid fitting is evaluated in a circular window of radius r = 0.85 mm (Figure 37).
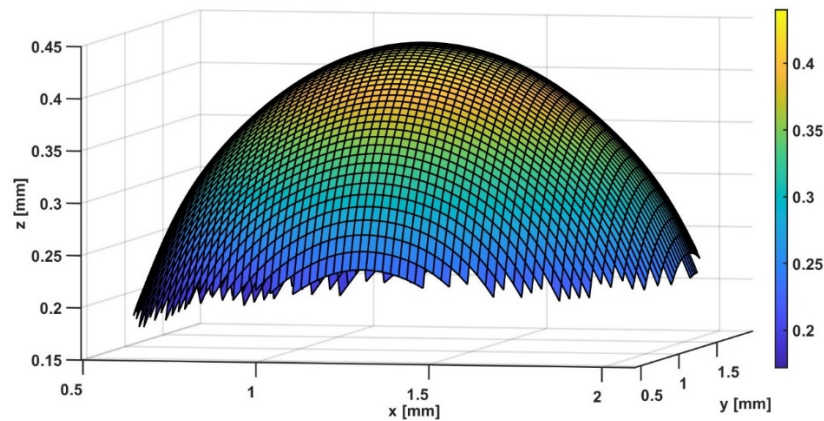
Figure 37: Gridfit approximant function referring to the surface obtained at the maximum pressure, evaluated in a circle or radius r=0.85 mm.

For each (x,y) point, the 2 × 2 curvature matrix, containing the second derivatives in x and y and the mixed derivatives, is calculated.

$$\begin{bmatrix} K_{xx} & K_{xy} \\ K_{yx} & K_{yy} \end{bmatrix}$$

Next, the eigenvalues of the curvature matrix are calculated, corresponding to the maximum (C_{max}) and minimum (C_{min}) curvature.

Values for the maximum vertical displacement and, at the same point, the principal curvatures were then extrapolated for each pressure level.

Since the configuration obtained with the first pressure level is considered the initial

one, for each pressure value, the vertical displacement was calculated by subtracting from the maximum displacement the one achieved with the first acquisition:

$$\Delta z_{pi} = z_{pi} - z_{p0}$$

where *i* ranges from the first pressure increment to the last one reached.

Regarding curvatures, a variable related to the degree of anisotropy (DA) was calculated for each pressor increment, as it was previously done in the work of D'Andrea *et al.* [48]:

$$DA_i = \frac{C_{max} - C_{min}}{C_{min}}|_i$$

DA turns out to be zero in the case where the two curvatures are equal, resulting in a isotropic deformed configuration, indicative of the isotropic behavior. Conversely, the more the value obtained deviates from zero, the greater the degree of anisotropy of the material under investigation, which is observed by an elliptical deformed configuration.

3.2.3. Finite element model of the bulge test

3.2.3.1. Setup

This section describes the finite element model implemented with ABAQUS/Standard software to simulate the experimental scenario. To realistically reproduce the experiment, two components were included in the simulation: the balloon sample and the metal cap of the device.

Thanks to the geometry and the isotropic behavior of the tested material, an axisymmetric assumption was operated. The shape is reproduced as a circular plate with a radius of 3.5 mm and a circular window of 1 mm radius. The polymeric sample, defined as a deformable solid, has a circular shape of radius 2.5 mm. The metal is placed above the material sample, covering 1.5 mm of its surface. The bulge window has a radius of 1 mm, where the metal leaves the material sample uncovered.
In Figure 38 is represented the final assembly.
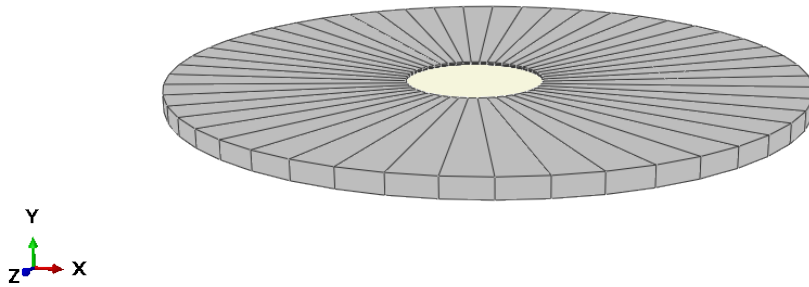
Figure 38: Metal cap assembled with the material sample.

The material assigned to the metal cap is steel, with a Young Modulus E = 200 GPa and a Poisson's ratio υ = 0.25.

To describe Nybax balloons from Boston Scientific and polyamide balloons from L2MTech, the polymeric sample is characterized by a hyperelastic isotropic material, described by the Yeoh constitutive model. The initial parameters (C_1, C_2, C_3) were calculated using stress-strain results from uniaxial tensile tests, as described in Section 1.2.3.

In the Figure 39 is shown how the analytical model fits the experimental data.
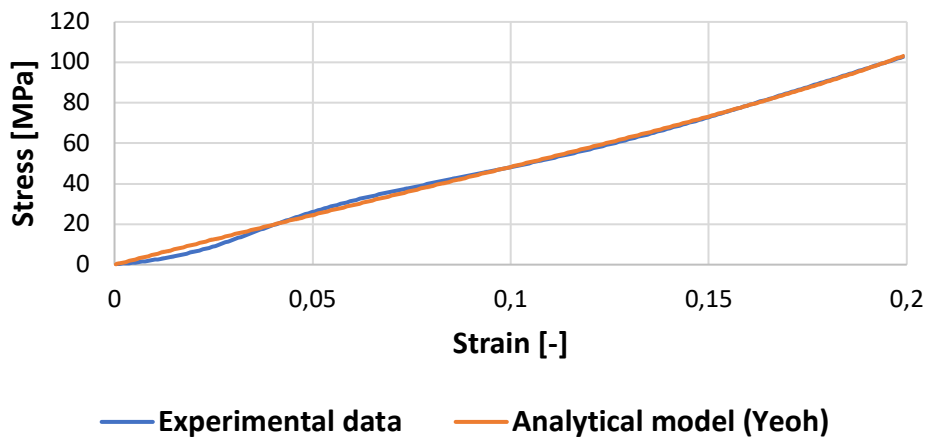
Figure 39: Experimental data of Nybax Mustang balloons fitted by the analytical model (Yeoh).

On the other hand, the experimental data shows that Pebax film samples from University of Montpellier exhibit different behavior (Figure 40). The stress-strain curve can be fitted by an elastoplastic model, setting E=300 MPa, υ=0.45 in the linear region, while σy= 27 MPa and εp = 0 in the plastic region.
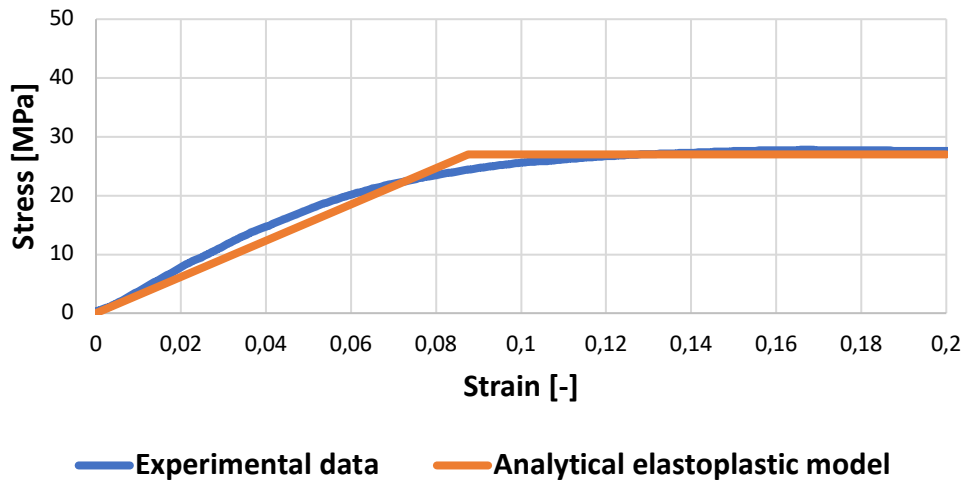
Figure 40: Experimental data of Pebax films fitted by the analytical elastoplastic model.

A surface-to-surface hard contact is set between the metal cap and the polymeric sample, with finite sliding. The metal plate is fully constrained, preventing vertical translation of the underlying polymeric sample. A reference point is created on the metal plate and constrained in vertical and horizontal translations and rotations about the z-axis. The polymeric material inside the bulge window is loaded with a uniform vertical pressure up to 0.14 MPa (Figure 42), along with–two other conditions: a symmetry in the center and a horizontal displacement (U1) constraint on the border (Figure 41).
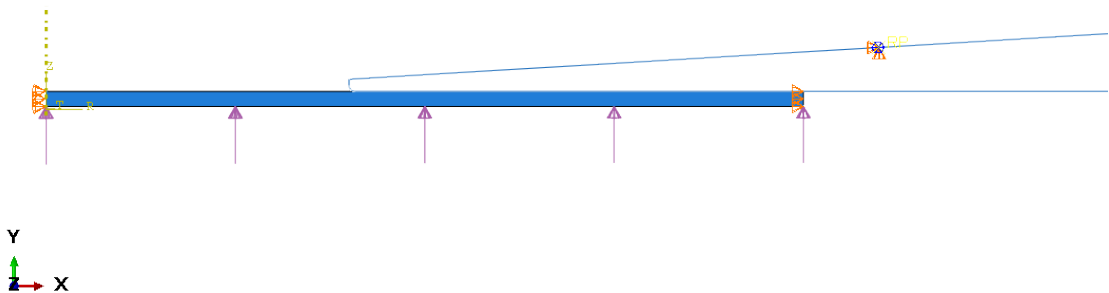
Figure 41: Schematic representation of loading and constraints in the initial configuration.
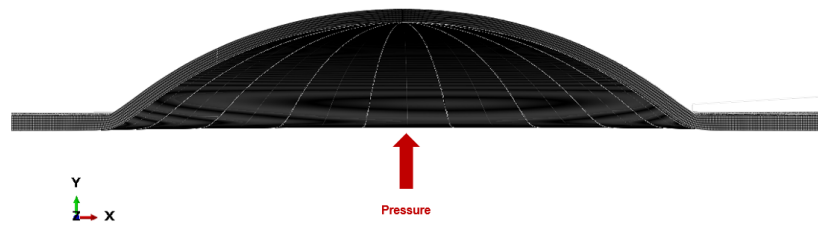
Figure 42: Schematic representation of the loading on the material specimen in the final configuration.
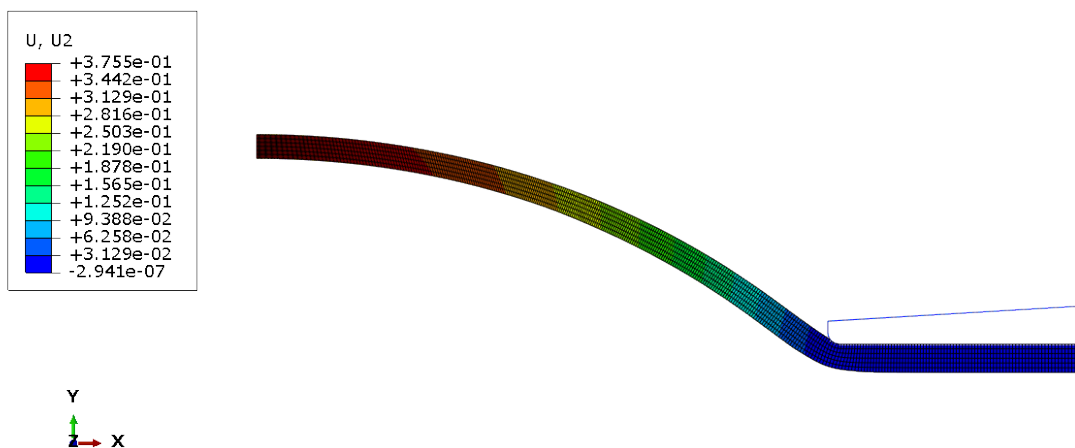
Figure 43: Vertical displacement of material section after applying maximum pressure.

Since the displacing part is the specimen, it is meshed with 3354 quadratic quadrilateral elements of type CAX8. To better investigate the behavior at the center of the sample, where the maximum vertical deflection is supposed to happen, the mesh has been densified (Figure 43). A bias is established, starting from the borders of the bulge window.

The simulation takes place in a single step, while the outputs are stored in evenly spaced time intervals, n=14, to correlate every time step to a 0.1 MPa increment of pressure. In order to compare the results obtained with this model with experimental results, the data were extracted from the minimum pressure to the maximum pressure in increments of 0.1 MPa.

For each simulation, the coordinates in the plane of the specimen and the vertical displacement U2 of the nodes belonging to the last layer of the mesh of the material sample were extrapolated (Figure 44). In particular, the only node whose vertical

displacement we are interested in is the one located in the center of the sample, where maximum inflation will occur.
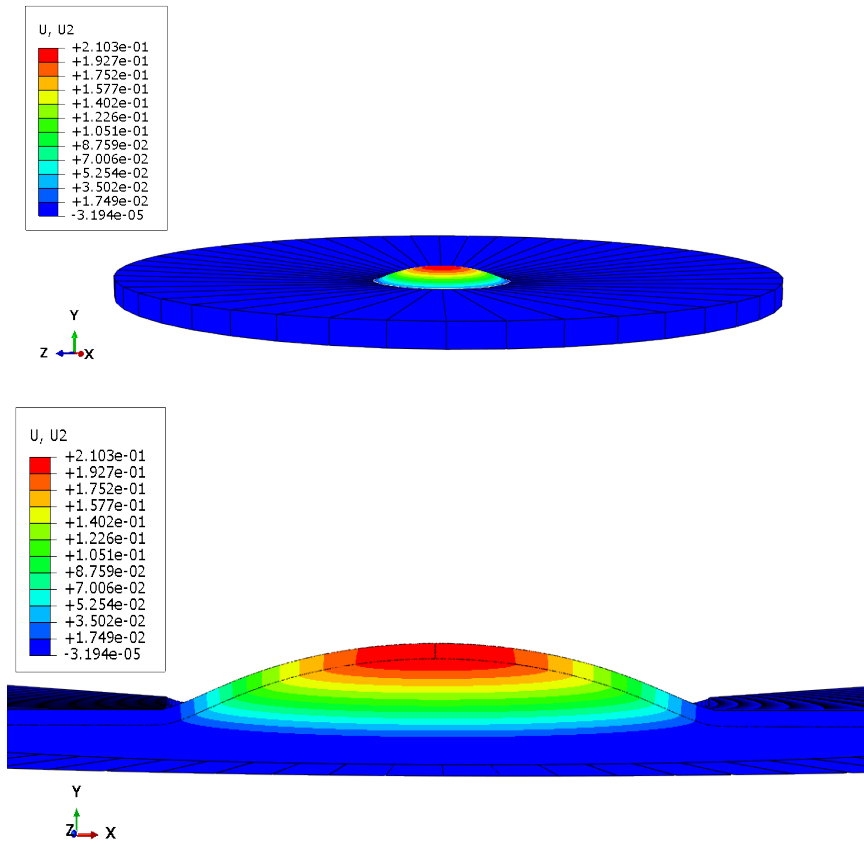
Figure 44: Maps of the displacement in the vertical direction of the points belonging to the polymeric material specimen.

3.2.3.2. Post-processing

For each simulation, the vertical displacement (U2) of the maximum unique node is extracted. As a result, a pressure-deflection curve is obtained and compared with the experimental pressure-deflection curve.

Initially, simulations were carried out using the average of material parameters obtained from uniaxial tests ($C_1^{ut}, C_2^{ut}, C_3^{ut}$). However, with these data, the analytical pressure-deflection curve could not best describe the experimental one. So, for this purpose, a range of variability was defined around the initial guess ($C_1^{ut}, C_2^{ut}, C_3^{ut}$). In this way, a new triplet of optimal parameters was obtained ($C_1^{fem}, C_2^{fem}, C_3^{fem}$) running numerous simulations. Finally, an error minimization criterion was defined, in order to find the best combination using MATLAB®.

The displacement in vertical direction (z) with respect to a reference point is calculated for each of the FEM (f^{FEM}) (Figure 46) and experimental (f^{exp}) (Figure 45) pressure – deflection curves. In this case, the reference is considered to be the displacement along the vertical direction at pressure 1 atm (z_{ref}).

$$f^{exp} = z_{i,exp} - z_{ref,exp}$$

$$f^{FEM} = z_{i,FEM} - z_{ref,FEM}$$

where i ranges from the initial pressure to the last one applied.
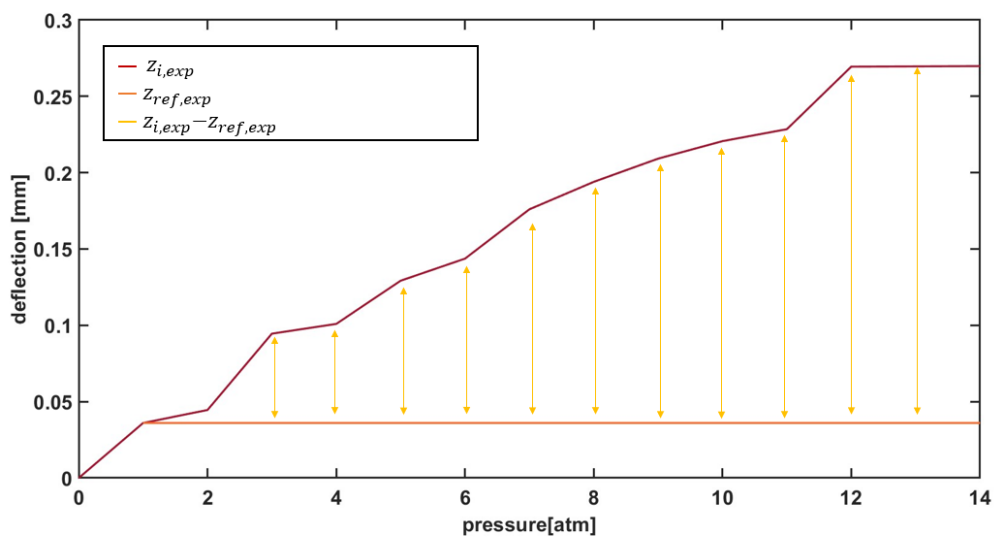
Figure 45: Deflection of the experimental mean ($z_{i,exp}$) and f^{exp} computation.
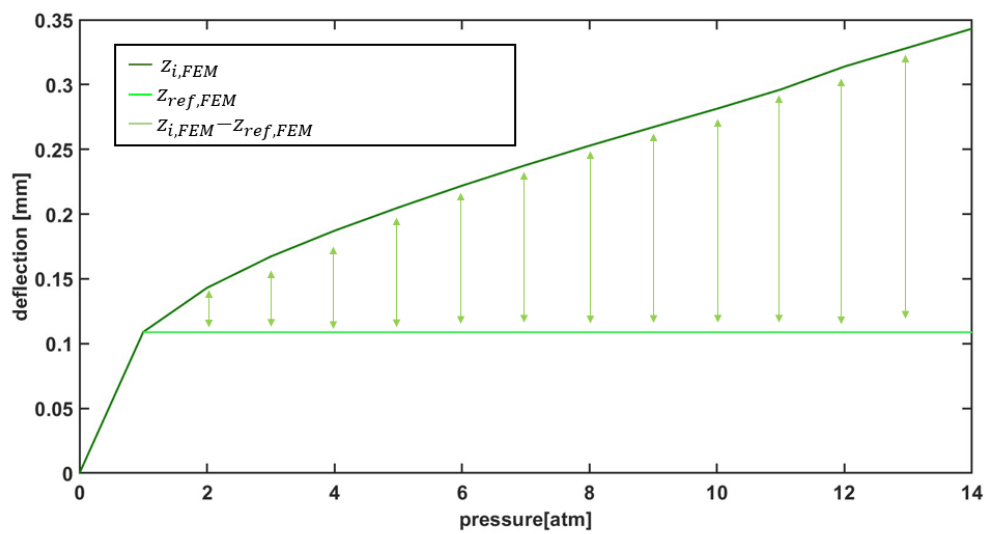
Figure 46: Deflection of the experimental mean ($z_{i,FEM}$) and f^{FEM} computation.

Once the vertical displacements are obtained, the error between each f^{FEM} and f^{exp} is calculated using the formula:

$$e = \sqrt{\frac{\sum_i \ (f^{FEM} - f^{exp})^2}{N}}$$

where N is the number of pressure steps, in this case N=14.

The simulation obtained using the parameter triplet that minimizes the error, is the one that best fits the experimental pressure-deflection curve.

3.2.4. Thickness measurement

Traditionally, the focal point of a laser microscope is set to the position where the reflected light intensity on the specimen is the highest (Figure 47 (a)). However, when dealing with transparent specimens, it can be difficult to accurately determine the correct specimen shape, as the laser beam can pass straight through it.

To address this issue, the LEXT OLS4100 confocal laser microscope has been utilized in this work. It is capable of detecting the peaks of reflected light intensities from multiple layers of the specimen and adjusting the focal point accordingly. As a result, it enables the observation and measurement of both the upper and lower surfaces of a transparent specimen, as well as the determination of its thickness using the *film thickness* tool. It is important to note that the knowledge of the refractive index of the material is necessary for accurate measurements.
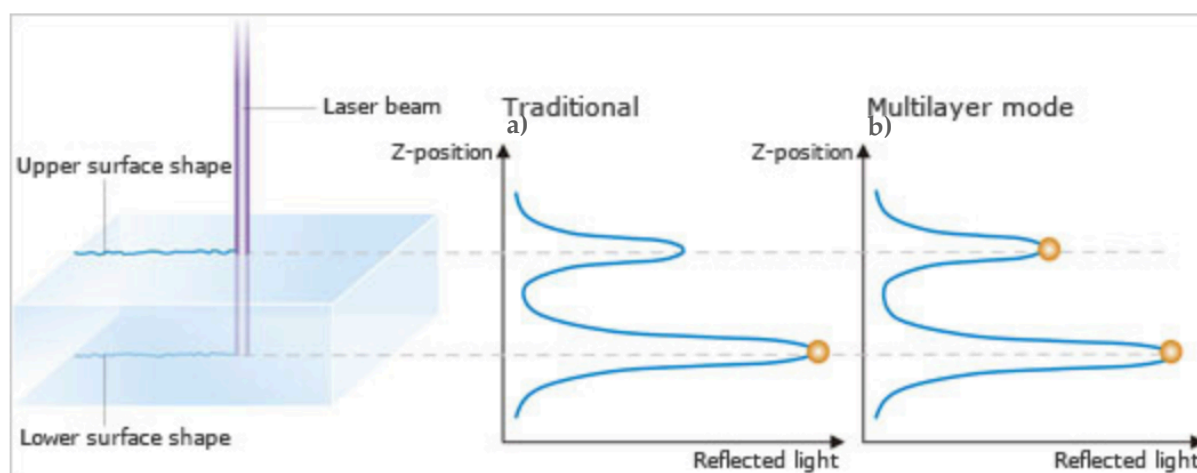
Figure 47: (a) Traditional laser microscope; (b) LEXT OLS4100 confocal laser microscope [50].

However, this method cannot be used for opaque samples, such as Pebax films. Therefore, in this case, the thickness is obtained by focusing on the upper and lower layers and taking the distance between them, without performing the acquisition of the image and employing the refractive index of the material.

4 Results and discussion

4.1. Uniaxial tensile test

The uniaxial tensile test was performed on Mustang Nybax balloons (both short and long), and Pebax films. Force and displacement values were recorded and used to compute the engineering stress and strain values.

The provided chart in Figure 48 illustrates the performance of Mustang Nybax short balloons (depicted in pink) and long balloons (depicted in green). For both, 8 samples have undergone 20% deformation at a displacement rate of 0.01 mm/s. It can be observed that the short balloons are capable of withstanding stresses ranging from 90 MPa to 115 MPa, while the long balloons exhibit a broader range, specifically between 110 MPa and 140 MPa.

For the sake of simplicity and for lacking knowledge on the material behavior upon unloading, hyperelasticity was assumed in material modeling, thus neglecting time dependence of the material.
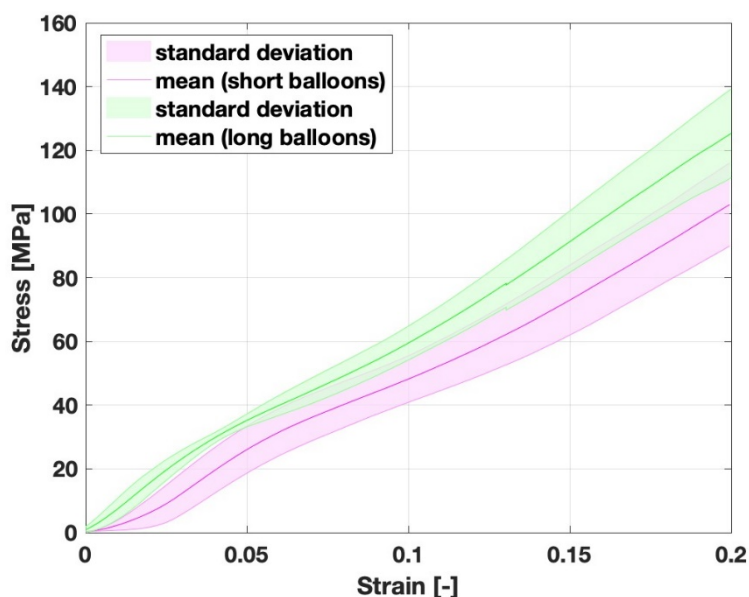
Figure 48: Graph referring to the average trend and relative standard deviation of stress-strain of Mustang Nybax short balloons (in green) and long balloons (in pink).

The results obtained from the uniaxial tests on 6 samples of Pebax film indicate that Pebax exhibits a non linear material response with the achievement of a maximum stress at increasing applied strain. Even if unloading protocol was not applied, the hypothesis of elasto-plasticity is made, characterized by a yield stress of approximately

27 MPa (Figure 49). Beyond this point, the material undergoes plastic deformation, with stress levels remaining relatively constant as the strain increases.
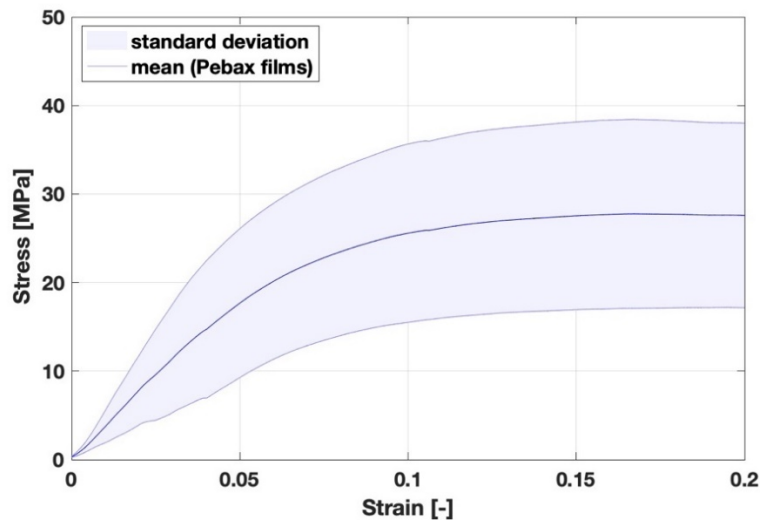
Figure 49: Graph referring to the average trend and relative standard deviation of stress-strain of Pebax films.

In summary, the uniaxial tensile tests conducted on Mustang Nybax balloons and Montpellier Pebax films were able to provide insights into the mechanical properties of these materials. The results obtained indicate hyperelastic and elastoplastic material behaviors, respectively, as presented graphically in Figure 50.
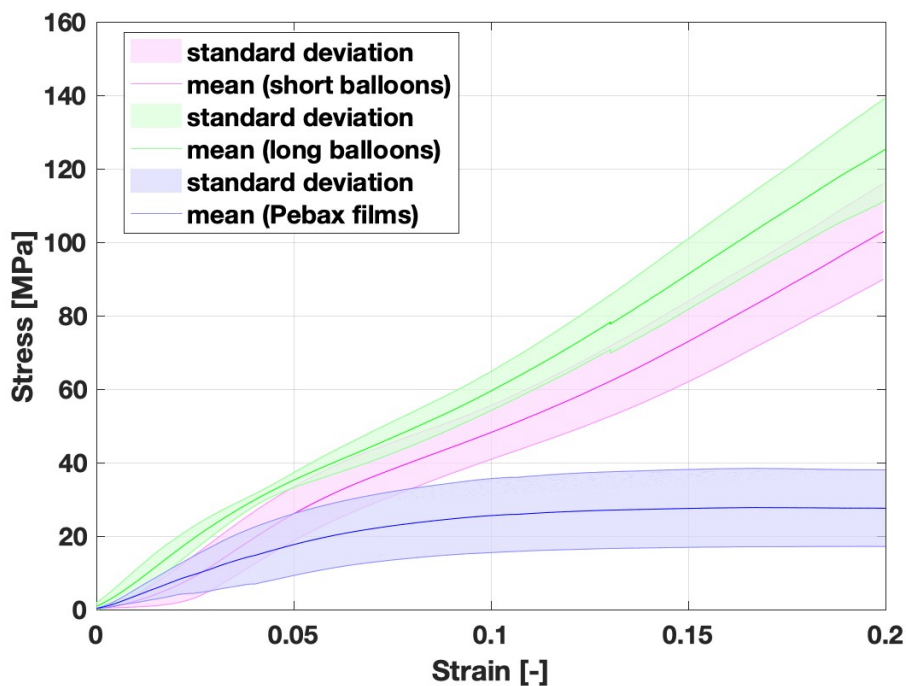
Figure 50: Comparison between Mustang Nybax short balloons (in pink), Mustang Nybax long balloons (in green) and Pebax films (in blue) stress-strain graphs.

The experimental stress-strain curves are then compared with the analytical ones, obtained using stress and strain computed with the Yeoh model (Section 3.2.1.4). The curves show similar behavior, with a slight difference in the initial part. This might be due to the fact that at the beginning of the experiment, the sample was not perfectly flat on the cantilevers, which is why the data have been cut-off with a force threshold of 0,1 N. However, this value might not be suitable for every test.

In Figures 51 and 52 the comparison between analytical and experimental stress-strain curves of Mustang Nybax short and long balloons is shown.
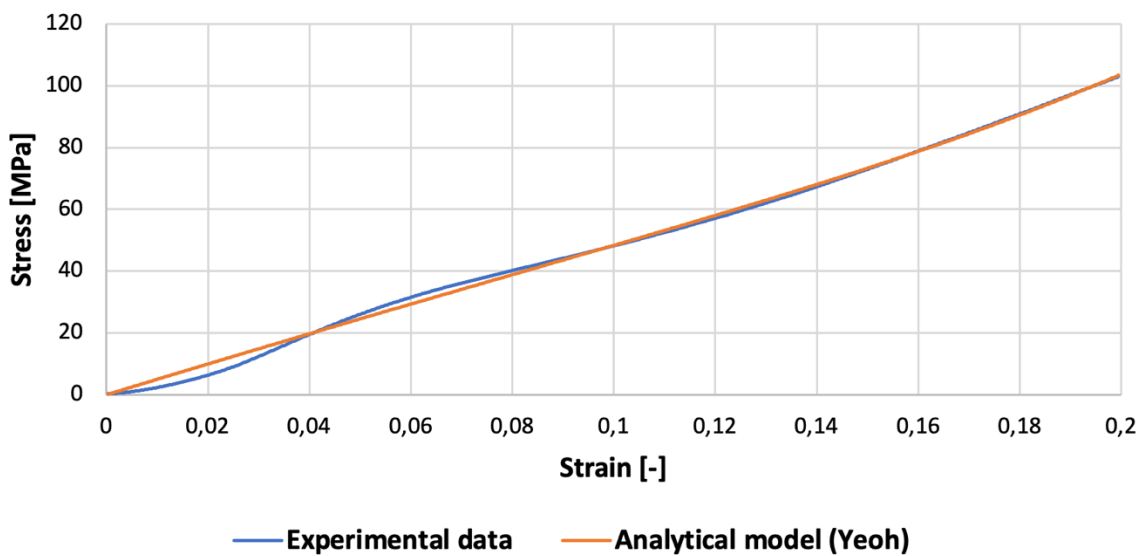
Figure 51: Comparison between analytical and experimental stress-strain curve of Mustang Nybax short balloons.
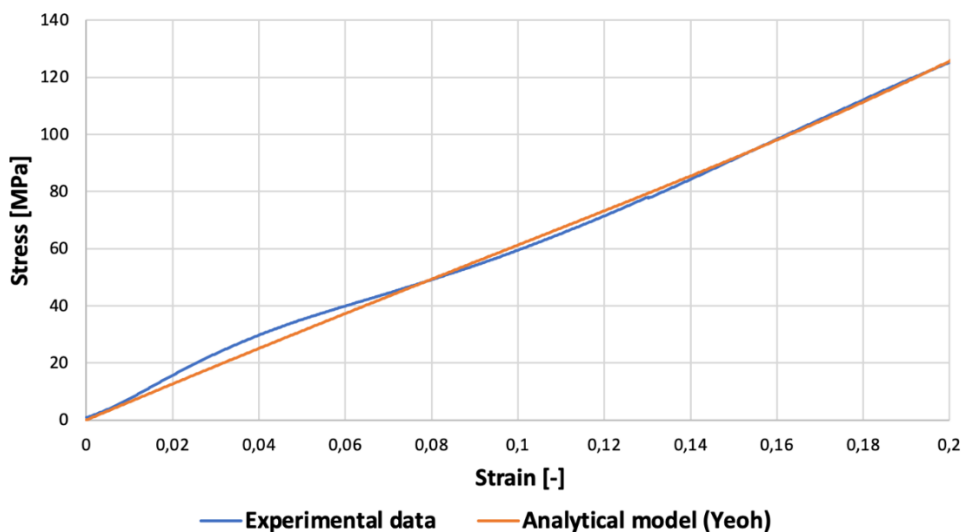
Figure 52: Comparison between analytical and experimental stress-strain curve of Mustang Nybax long balloons.

The excel tool performs an error minimization between the experimental and analytical curves and gives as result the material parameters C_1, C_2, C_3. This has been done for each test, and the minimum and maximum values are used as starting range to perform Abaqus simulation (Section 4.3.2).

In the case of the Pebax film, due to its elastoplastic behavior, a different procedure was followed to analyze the stress-strain curve. The experimental curve was divided into two regions: a linear and a plastic region (Figure 53). The linear curve was computed using the formula $\sigma = E * \varepsilon$, where E is the elastic modulus and ε is the experimental strain. Instead, the plastic region was computed using the yield stress σ_y and the plasticity strain ε_p. In this case, E is equal to 300 MPa, σ_y is equal to 27 MPa and ε_p is equal to 0. Overall, this approach allowed for a more detailed analysis of the behavior of Pebax under tensile loading and provided valuable insights into its mechanical properties.
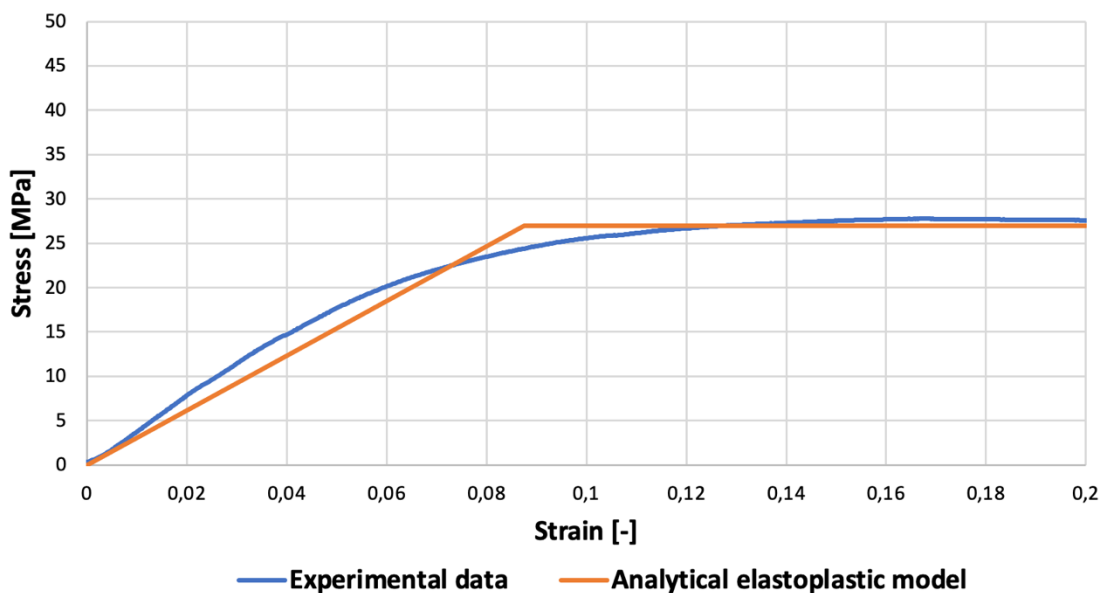
Figure 53: Comparison between analytical and experimental stress-strain curve of Pebax films.

4.1.1. Poisson's ratio calculation

As previously explained in Section 3.2.1.3, through the markers representation on the specimen undergoing uniaxial tensile testing, it has been possible to calculate the Poisson's modulus, as the ratio between the transverse strain and the longitudinal one:

$$\nu = - \frac{\varepsilon_{trasv}}{\varepsilon_{long}}$$

The video recording during the test (Figures 54 (a) and 54 (b)) has been converted into frames using Fiji (Figures 54 (c) and 54 (d)). The orange arrow represents the longitudinal strain, while the green arrow represents the transverse strain, both used to calculate the Poisson ratio.

(a)

(b)

(c)

(d)
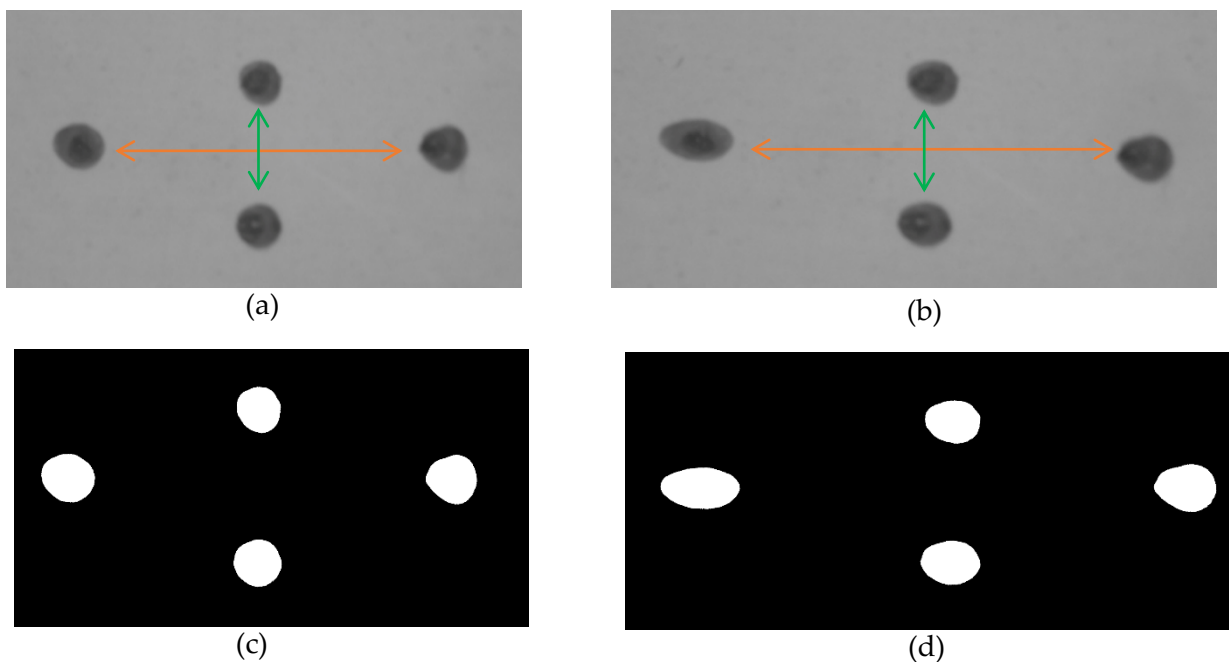
Figure 54: Undeformed (a) and deformed (b) configuration from the video recording during the test; undeformed (c) and deformed configuration (d) from the frame analysis using Fiji.

Making the average on 9 different tests, a Poisson ratio of $\nu = 0.45$ is obtained.

4.2. Surface characterization

4.2.1. Uncoated samples

Surface images were captured using the confocal laser microscope (LEXT ols 4100) employing a 20X magnification lens. In the figures are shown the surface of unfolded Mustang balloons (Figure 55), folded Flexitrack balloons (Figure 56) and Pebax films (Figure 57).
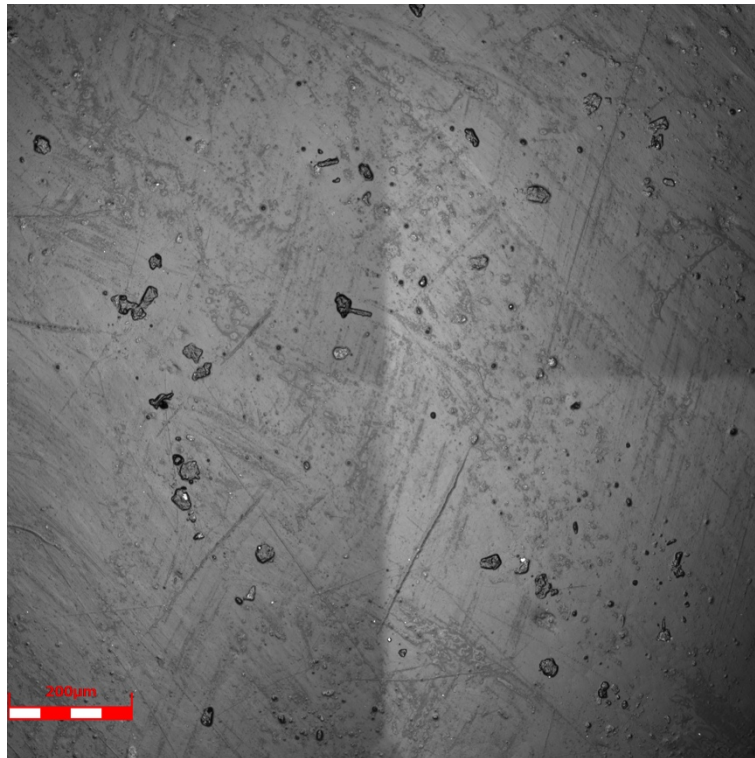
Figure 55: Unfolded Mustang balloons surface.
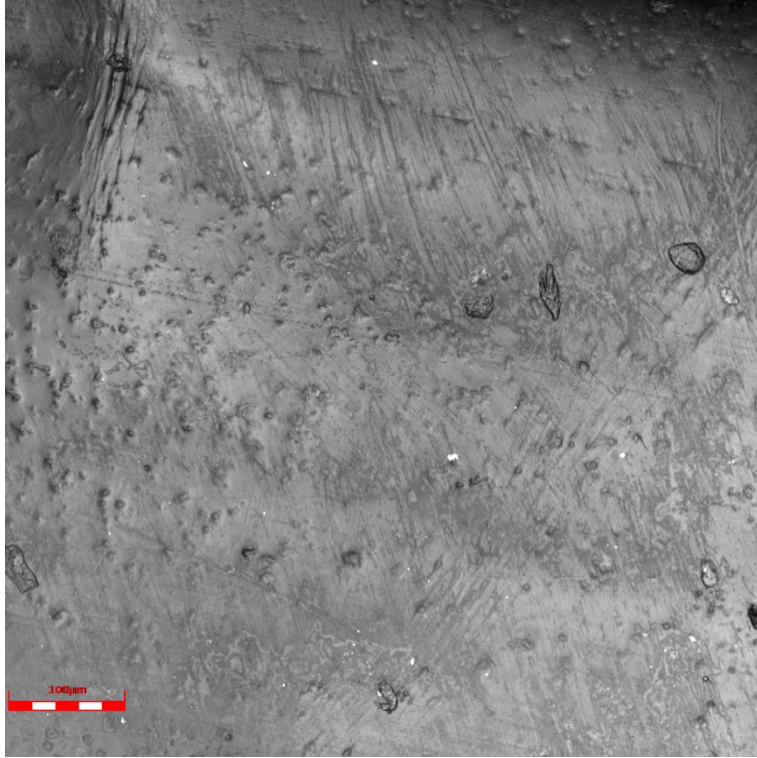
Figure 56: Folded Flexitrack balloons surface.
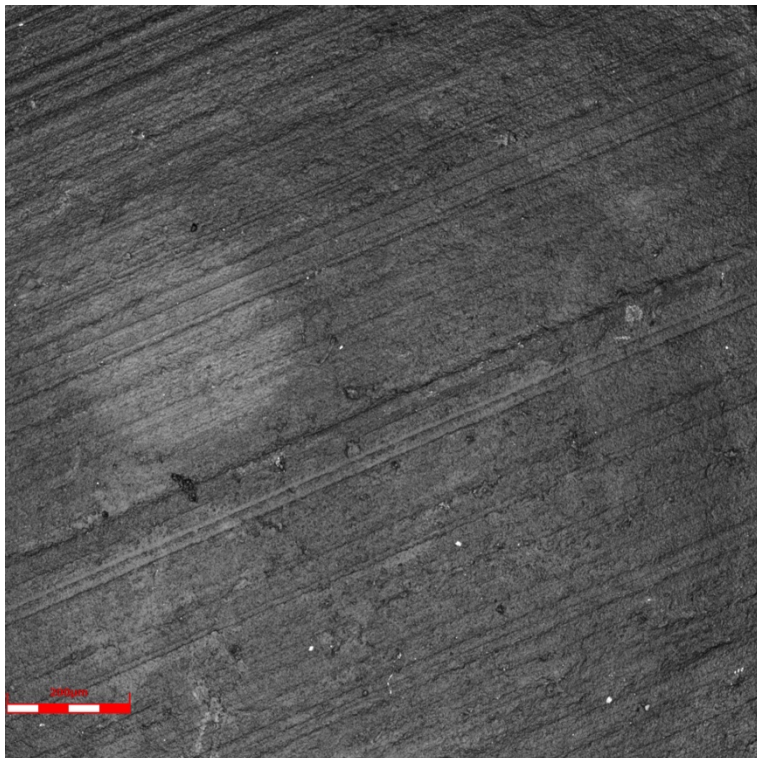
Figure 57: Pebax films surface.

4.2.2. Coated samples

Surface images were captured using the confocal laser microscope (LEXT ols 4100) employing different magnification lenses.

Polymer – spray – coated samples

In these samples, the excipient (Pluronic 123) is sprayed on the Pebax substrate (Figure 58(a), 58(b), 59(a), 60(a), and 61(a)). The coating displays heterogeneity with certain regions exhibiting greater prominence, as is evident from the observation of height images (Figures 59(b), 60(b), 61(b)).

(a)   (b)
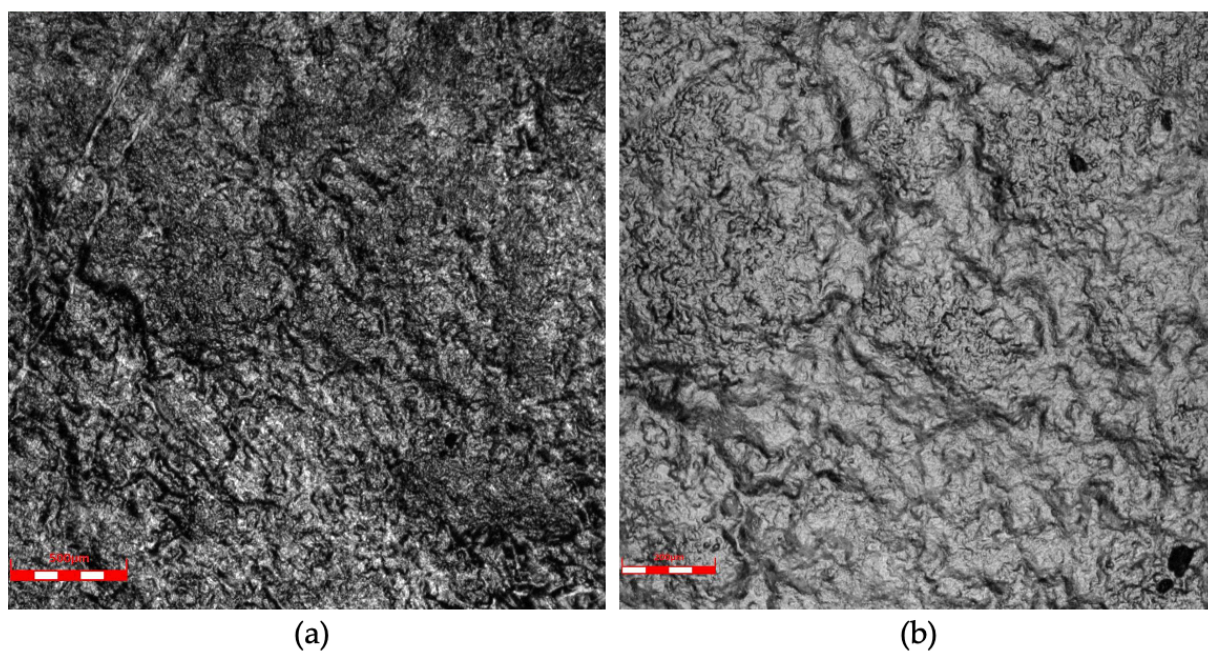
Figure 58: Laser intensity image of polymer-spray-coated Pebax film at 5X magnification (a) and 10X magnification (b).
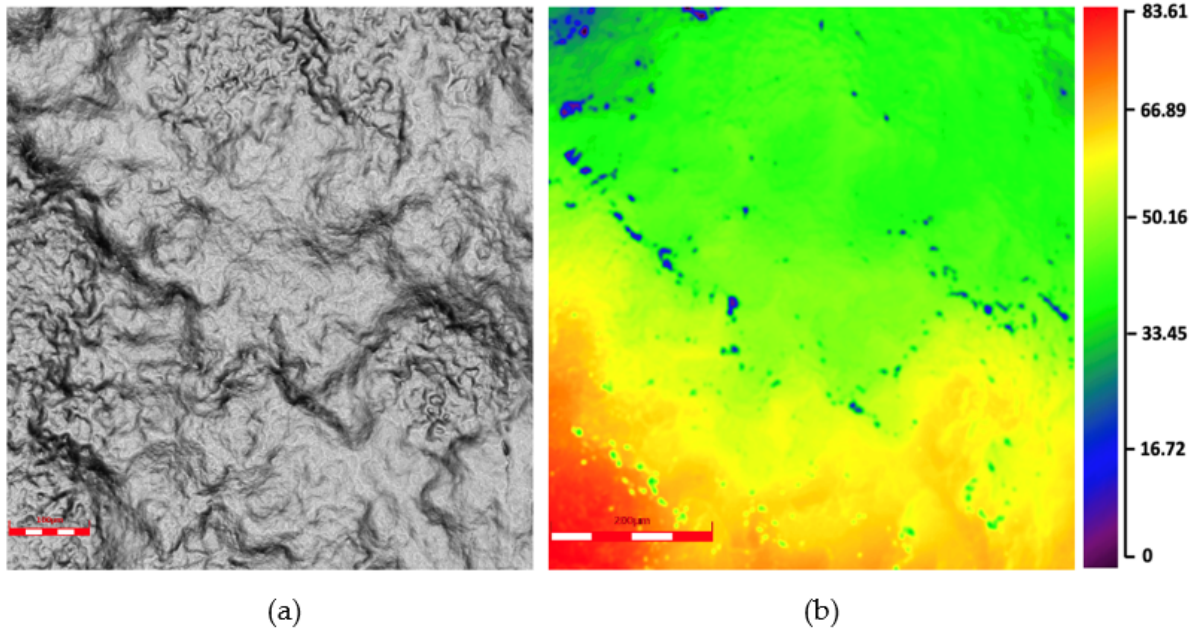
Figure 59: Laser intensity (a) and height image (b) of polymer-spray-coated Pebax film at 20X magnification.
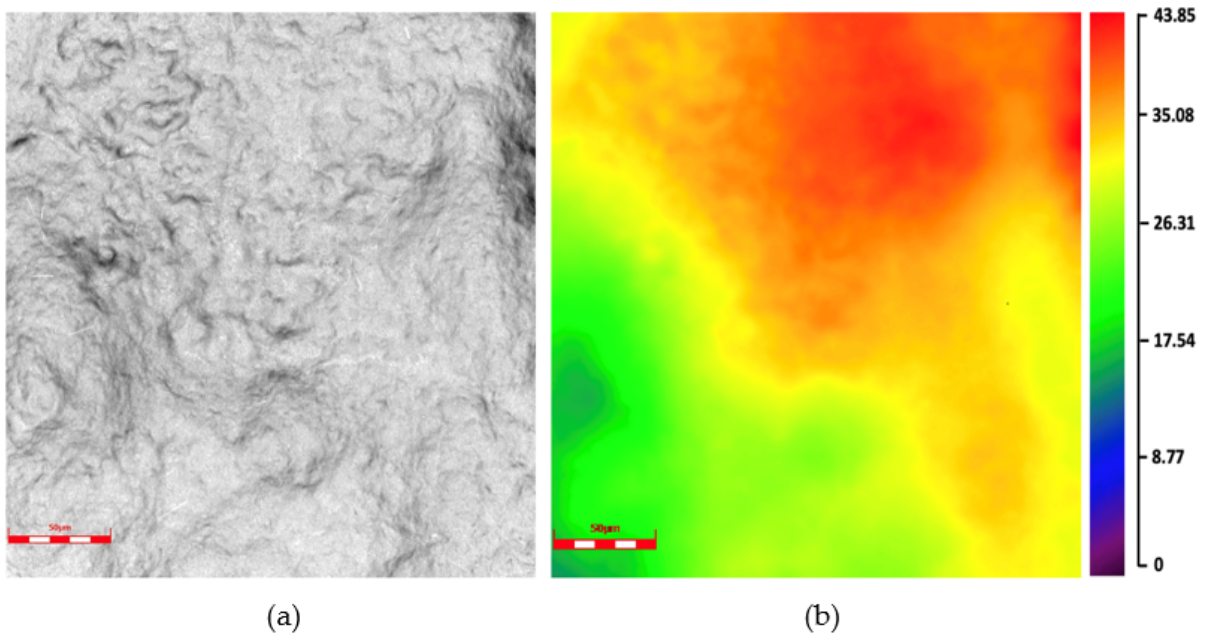
Figure 60: Laser intensity (a) and height image (b) of polymer-spray-coated Pebax film at 50X magnification.

(a)　　　　　　　　　　　　　　　　　　(b)
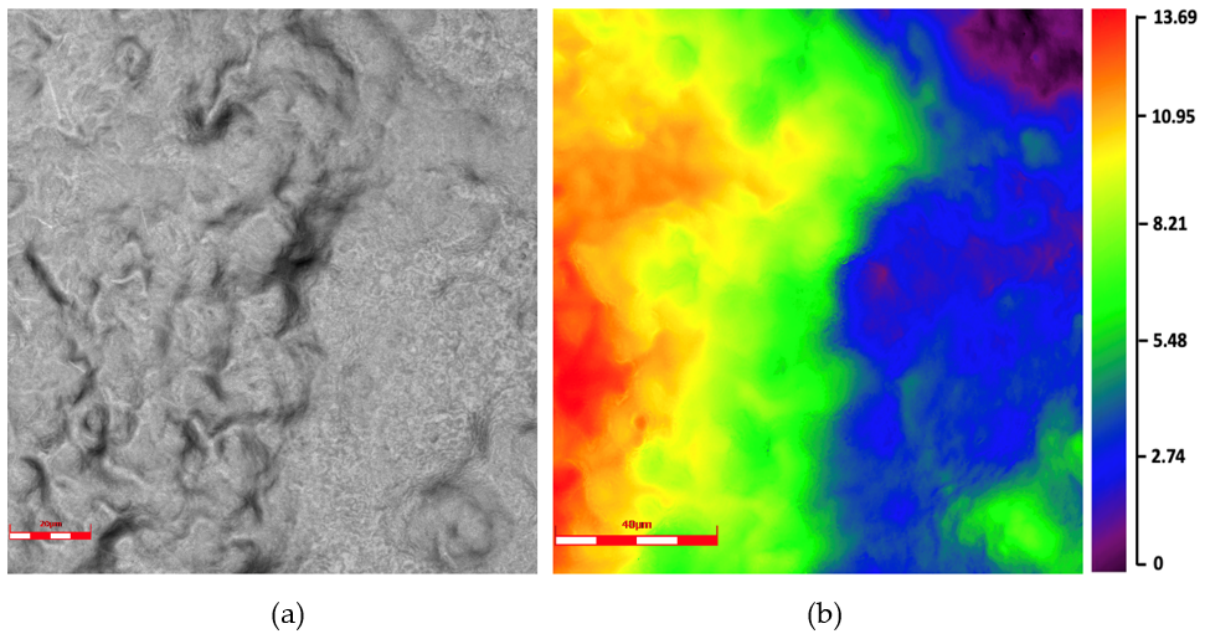
Figure 61: Laser intensity (a) and height image (b) of polymer-spray-coated Pebax film at 100X magnification.

Polymer – micropipette – coated samples

In these samples, the polymer is deposited onto Pebax substrate using the micro-pipetting technique (Figure 62, 63, 64). The use of this deposition method results in a less homogeneous substrate than that obtained through the spray-coating technique (Section 2.1). Indeed, excipient accumulation can be observed in certain regions of the sample.

(a)   (b)
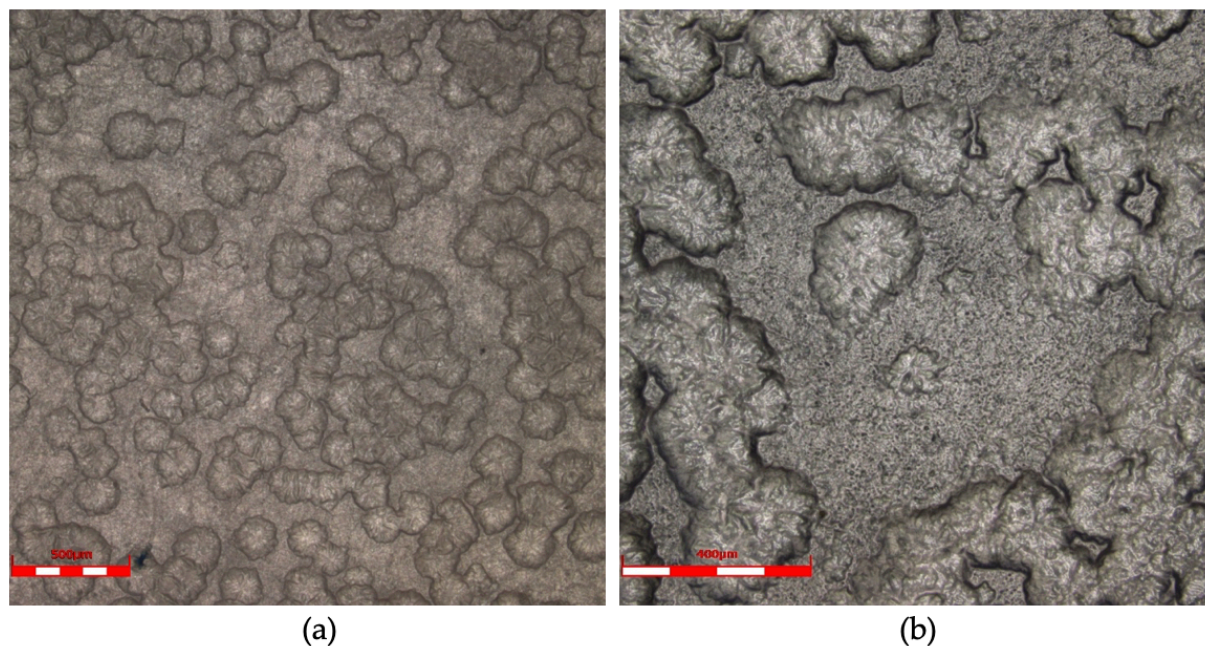
Figure 62: Laser intensity image of polymer-micropipette-coated Pebax film at 5X magnification (a) and 10X magnification (b).

(a)   (b)
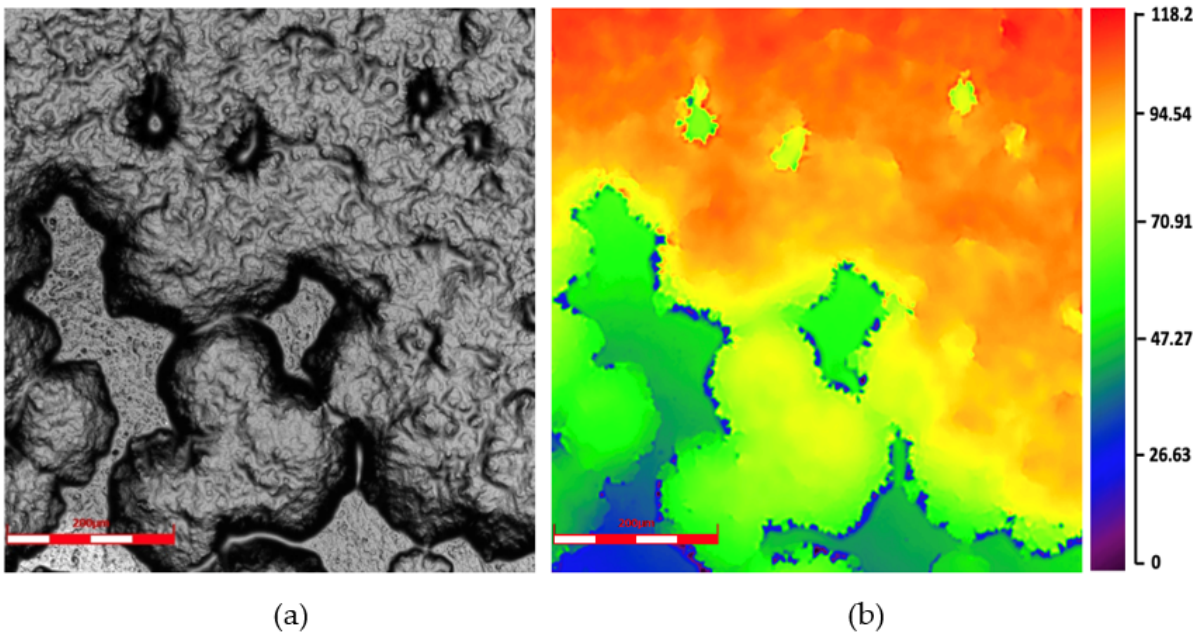
Figure 63: Laser intensity (a) and height image (b) of polymer-micropipette-coated Pebax film at 20X magnification.

(a)   (b)
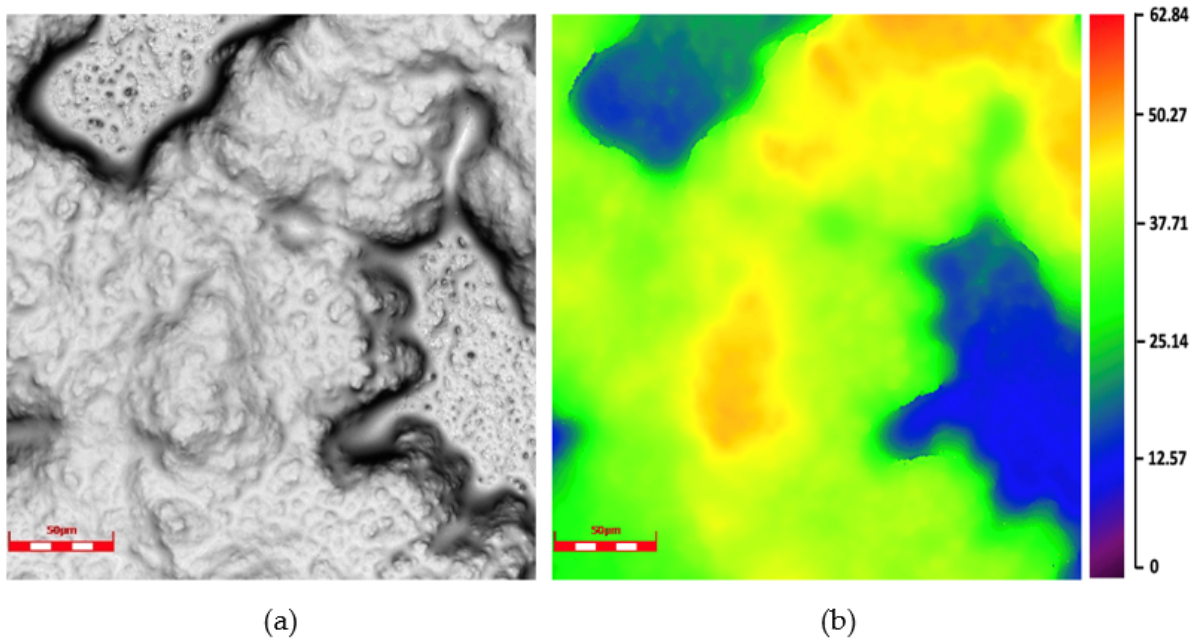
Figure 64: Laser intensity (a) and height image (b) of polymer-micropipette-coated Pebax film at 50X magnification.

After observing the whole specimen, it was noted that a specific area was characterized by the presence of polymer accumulations alongside a more uniform zone (Figures 65(a) and 65(b)). Upon further analysis, it was determined that the homogeneous zone did possess a coating, although its appearance was flatter compared to the uneven and

accumulated appearance of the coating in the discontinuous zone. Despite this difference in appearance, it was found that the thickness of the coating in the homogeneous zone was comparable to that of the polymer accumulations in the discontinuous zone (Figure 66).

(a)   (b)
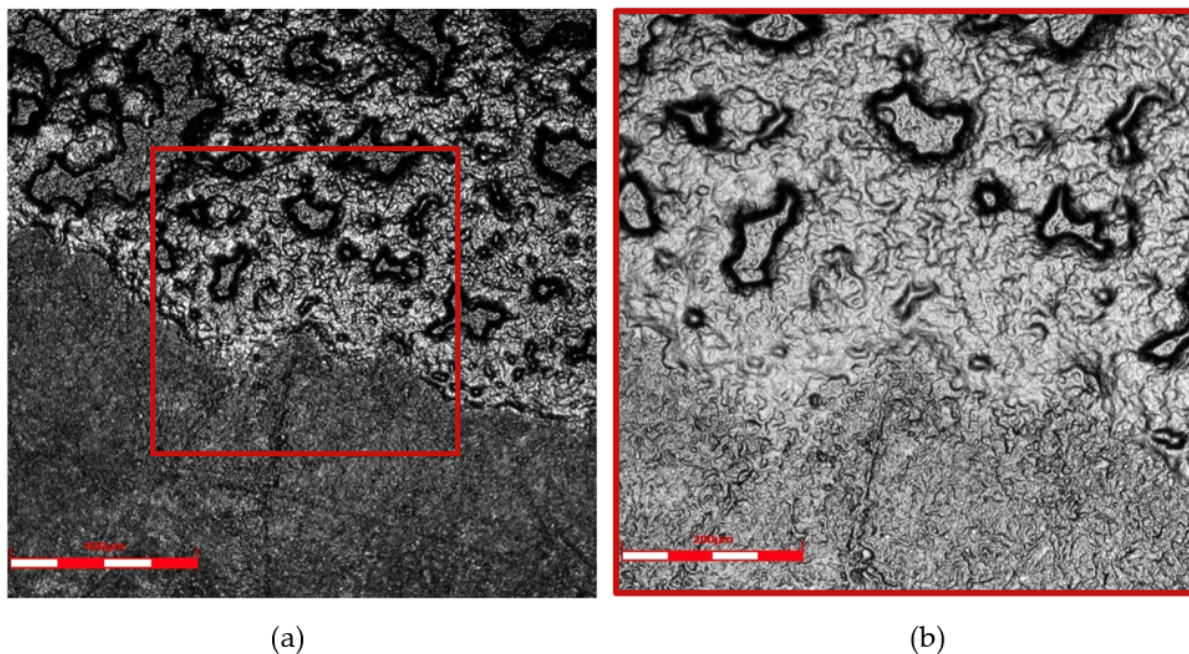
Figure 65: Laser intensity image of polymer-micropipette-coated Pebax film at 10X magnification (a) and 20X magnification (b).

(a)   (b)
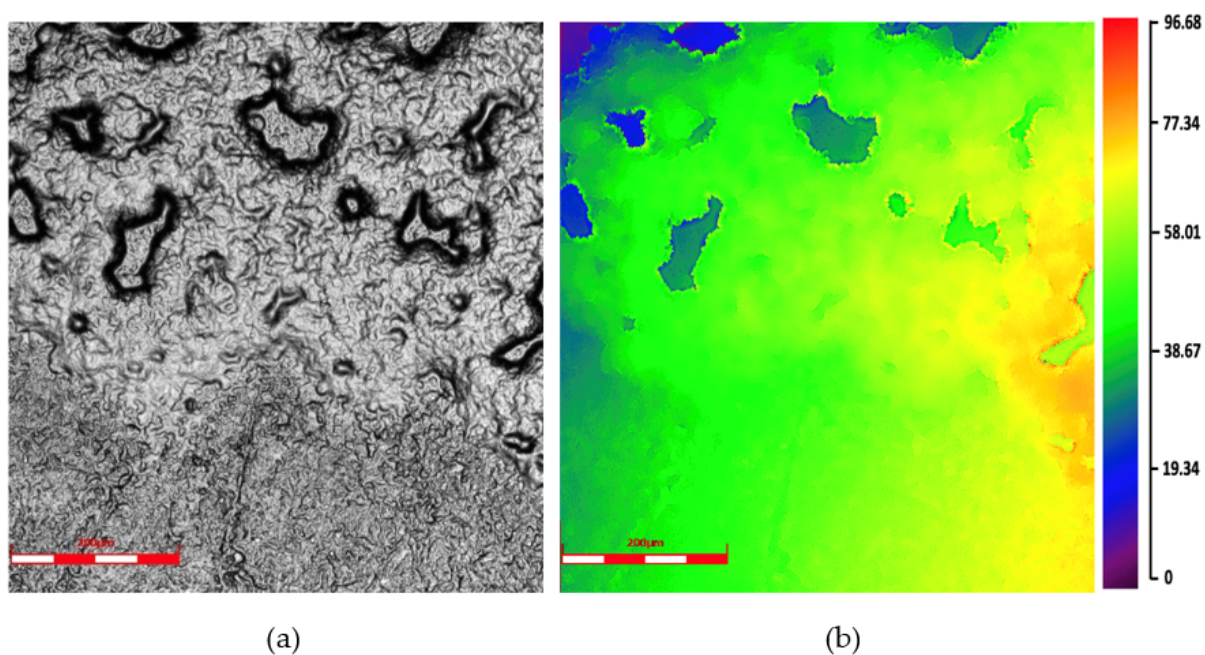
Figure 66: Laser intensity (a) and height image (b) of polymer-micropipette-coated Pebax film at 20X magnification.

Drug – excipient – coated samples

In the latest types of samples tested the coating solution is the excipient matrix (Pluronic123) with a drug (Everolimus) embedded in it (Figure 67, 68 and 69).

(a)   (b)
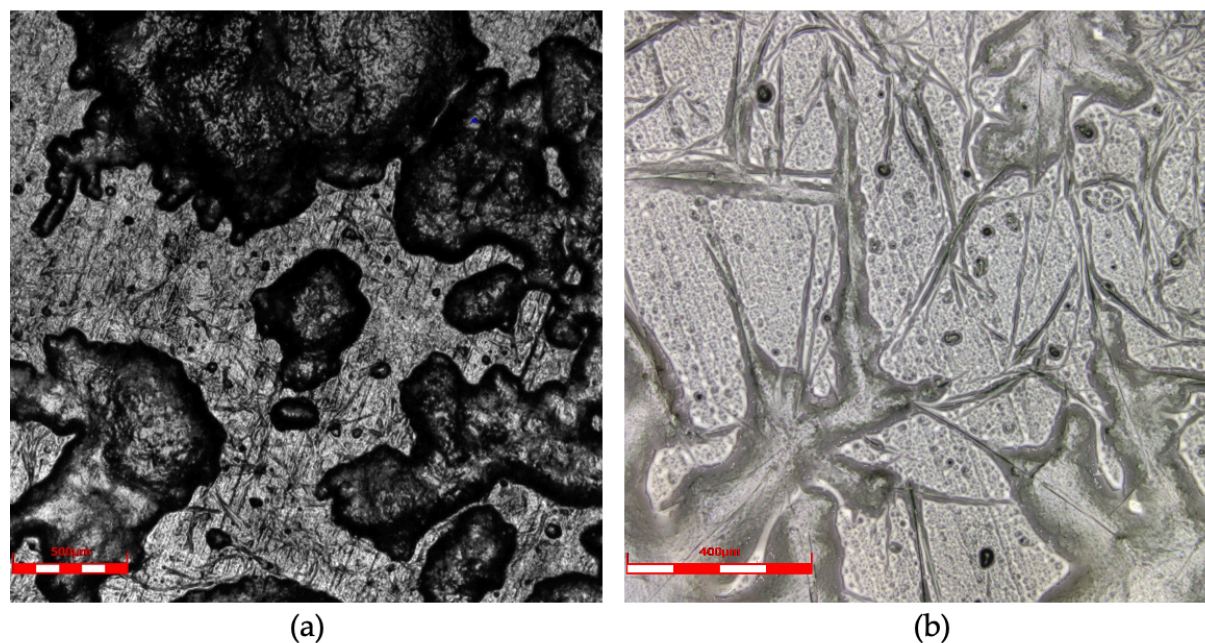
Figure 67: Laser intensity image of drug-coated Pebax film at 5X magnification (a) and 10X magnification (b).

(a)   (b)
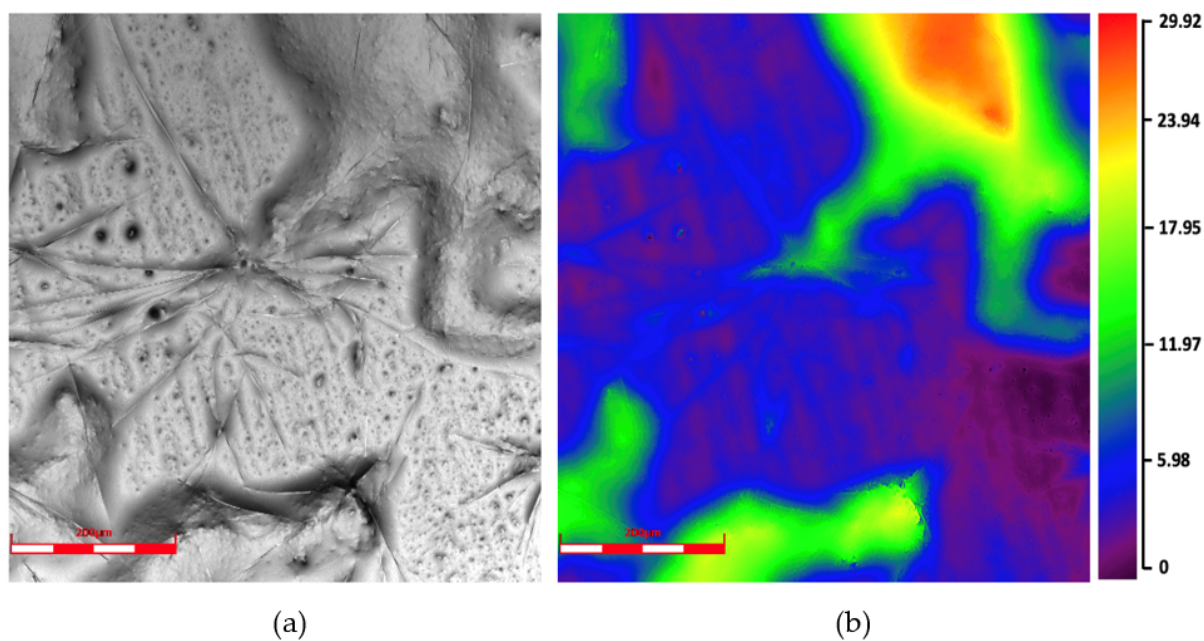
Figure 68: Laser intensity (a) and height image (b) of drug-coated Pebax film at 20X magnification (point 1).

(a) (b)
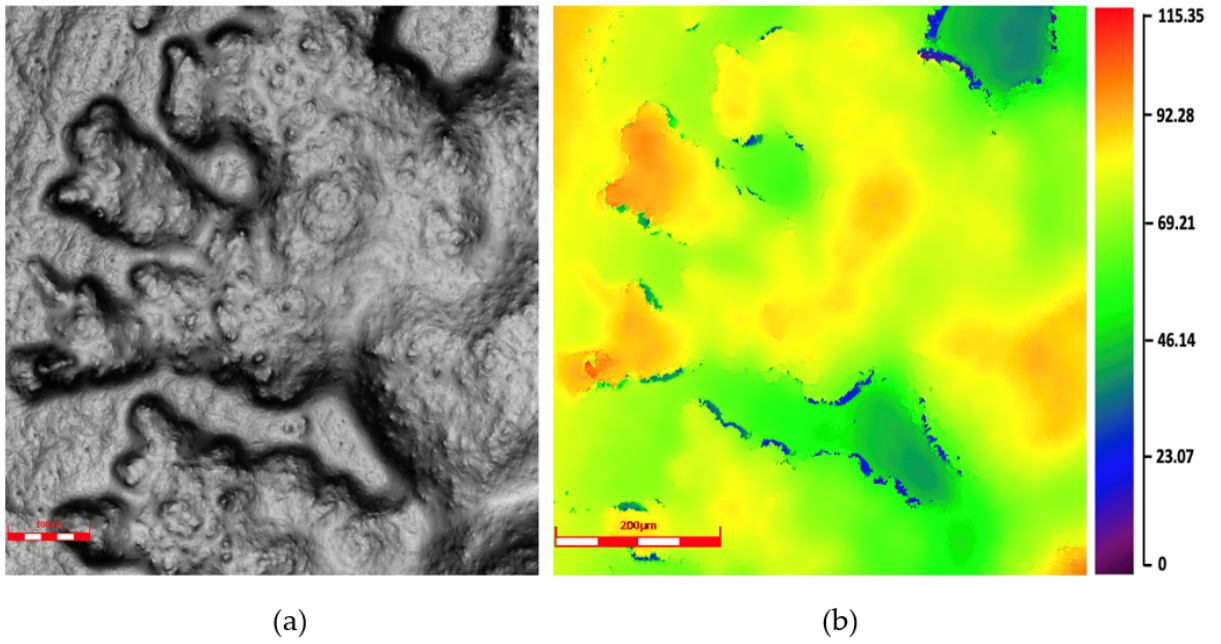
1

Figure 69: Laser intensity (a) and height image (b) of drug-coated Pebax film at 20X magnification (point 2).

4.3. Bulge test

In this study, during the bulge test, the polymeric sample is attached to a metal cap that has a circular opening in the middle that exposes the material to the pressure, as shown in Section 3.2.2.1. Utilizing an inflation device, a differential hydraulic pressure is delivered from below. The confocal laser microscope (LEXT OLS4100, Olympus®) captured the shape of the deformed material, and the image is then post-processed using MATLAB® for pressure-deflection analysis.

The results are presented in a pressure-deflection graph (Figure X). For every kind of material sample the deflection mean (in mm) at each pressure increment (in atm) is calculated. The pressures and the deflections are intended as differential with respect to the initial configuration:

$$\Delta z_i = z_i - z_0$$
$$\Delta p_i = p_i - p_0$$

in which i ranges from the first pressure increment to the last one achieved.

The initial pressure p_i=1 atm has been selected as the minimum pressure level at which wrinkles in the membrane patch disappear. Therefore, applying a pretension in the initial condition results the specimen surface is more regular.

4.3.1. Uncoated samples

The bulge test is performed on 14 samples of Nybax® balloons from Boston Scientific, 7 samples of polyamide balloons from L2MTech, and 5 samples of Pebax films from the University of Montpellier. It was not possible to test Nybax® folded balloons from Boston Scientific, due to their high circumferential stiffness, which did not allow them to be cut and glued on the setup.
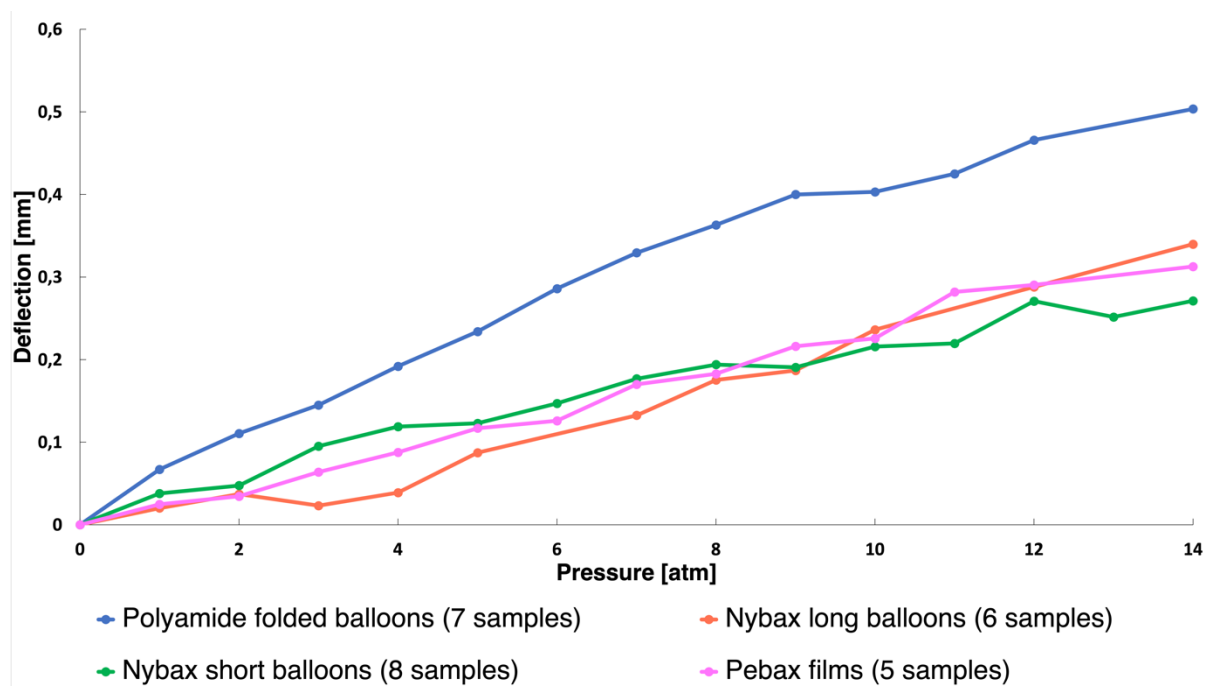
Figure 70: Mean of pressure-deflection curves obtained performing the bulge test on Nybax balloons (short and long), Pebax films and polyamide balloons.

The graphs in Figure 70 refer to samples with a thickness of 50 μm approximately for the unfolded balloons and the Pebax films, while 20 μm for the folded ones. The inflation test was performed until reaching the maximum pressure. It happened that the experiments had to be interrupted due to water leakage from the bulge window or sample bursting around 16 atm or 18 atm pressure. Therefore, to standardize the results, it was chosen to stop the test at a pressure of 14 atm, to be sure that all the samples analyzed reached the same pressure.

The Pebax and Nybax samples tend to have similar behavior during inflation, reaching a maximum deflection of nearly 0.3 mm at a pressure of 14 atm. Differently, the polyamide samples tend to inflate more and reach a maximum deflection of 0.5035 mm at the maximum pressure. This could be due to the difference in thickness. The 20 μm samples tend to be more compliant while inflated with the same pressure increments as the 50 μm ones. To quantify the dispersion of experimental data, the standard deviation relative to the set of experimental trials was calculated in addition to the mean. The results are reported in Figures 71, 72, 73 and 74.
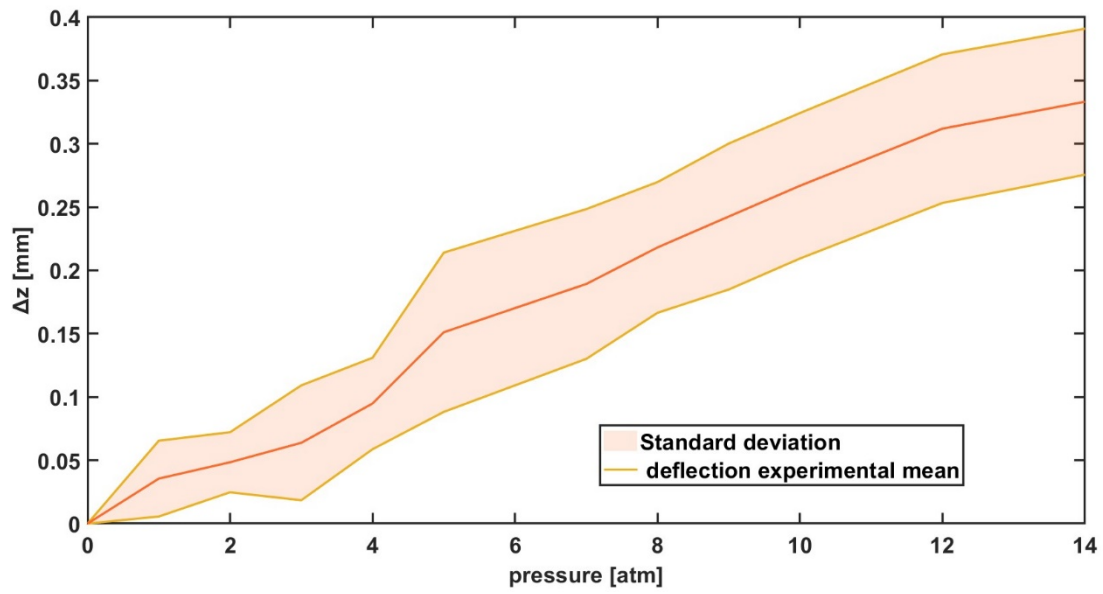
Figure 71: Mean and standard deviation for the pressure-deflection curve of Mustang Nybax® long balloons.
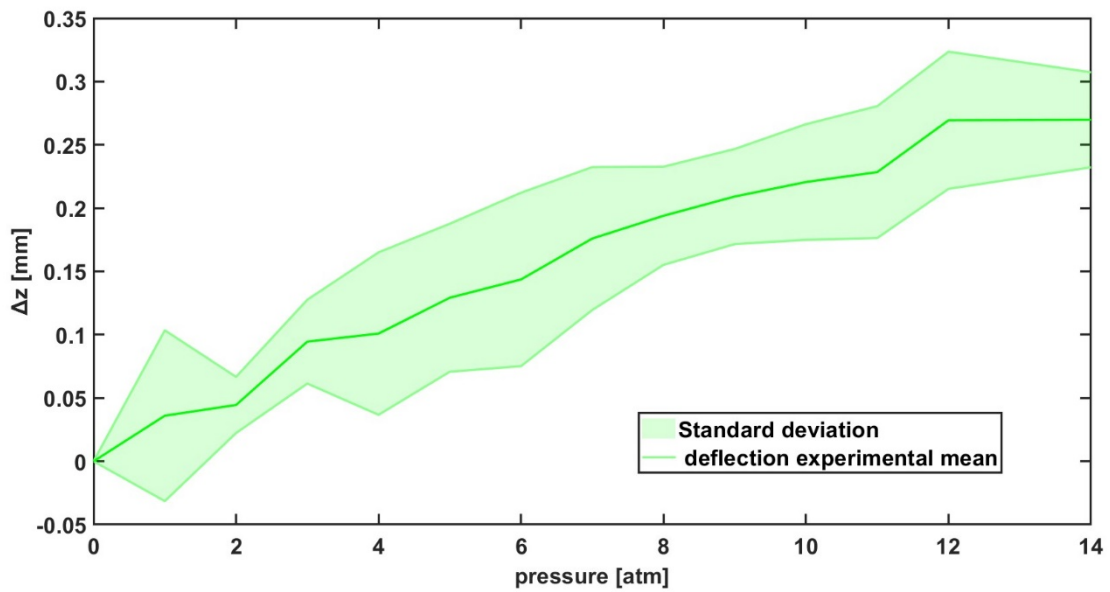
Figure 72: Mean and standard deviation for the pressure-deflection curve of Mustang Nybax® short balloons.
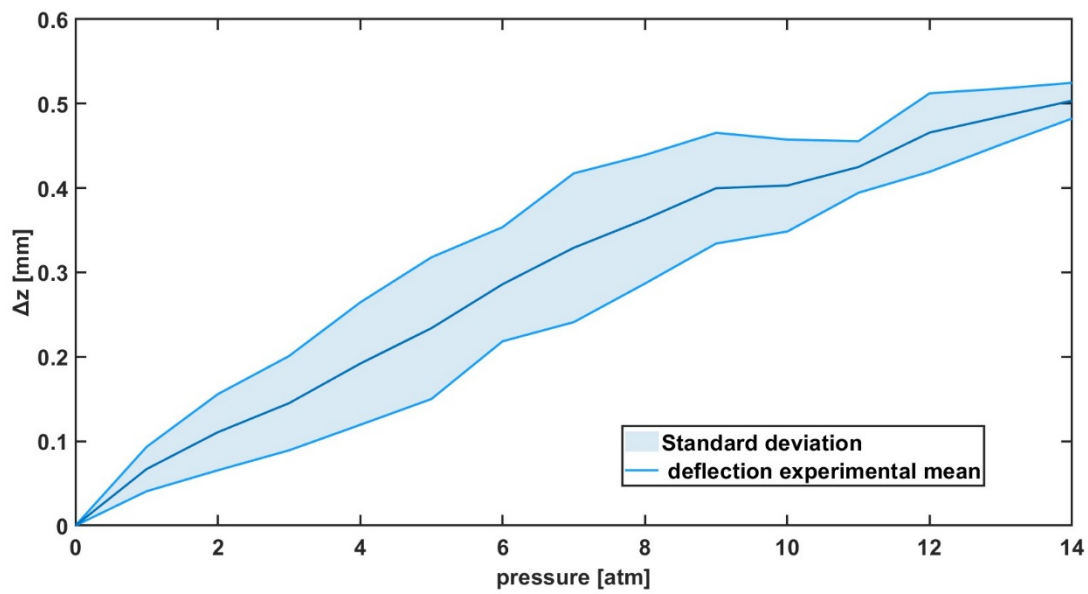
Figure 73: Mean and standard deviation for the pressure-deflection curve of polyamide (Nylon) folded balloons.
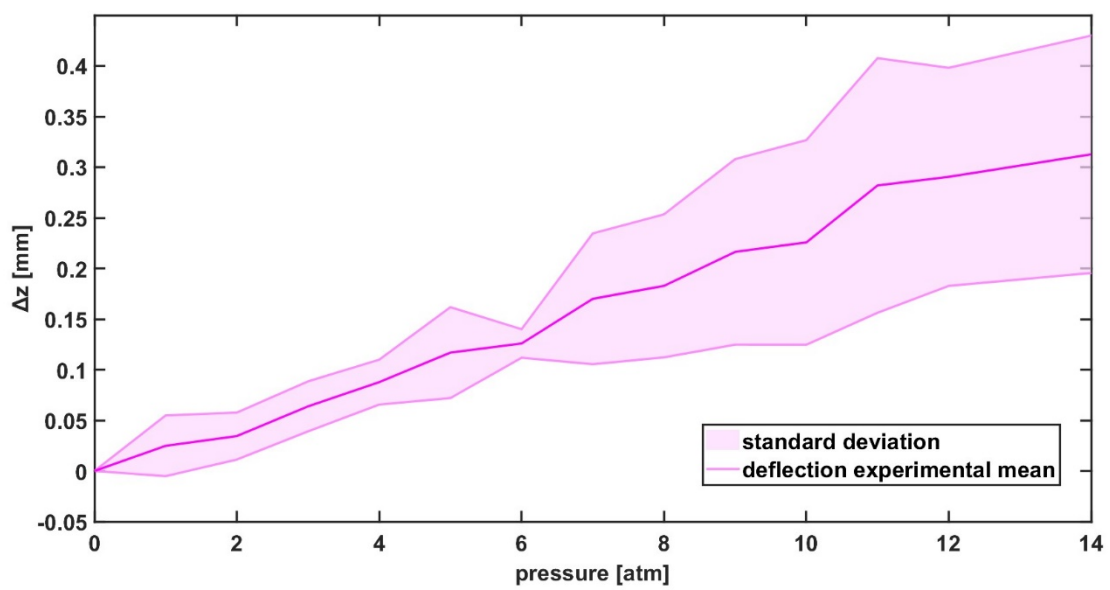
Figure 74: Mean and standard deviation for the pressure-deflection curve of Pebax® films.

4.3.2. Comparison between experimental bulge test results and FE simulations of uncoated samples

Starting from the Yeoh analytic parameters calculated by fitting the uniaxial tensile test data (Section 4.1), the maximum and minimum values of C_1, C_2 and C_3 are extracted for Nybax balloons from Boston Scientific. A range of parameter variation was set to start the finite element simulations, reported in Table 4.

Due to the small size and due to the high stiffness of the Flexitrack folded balloons from L2MTech, they were not subjected to uniaxial tensile tests. The finite element simulations of the bulge test on Flexitrack balloons were carried out by assuming the same constitutive parameters as that of the other balloons.

Sample	Min C_1 [MPa]	Max C_1 [MPa]	Min C_2 [MPa]	Max C_2 [MPa]	Min C_3 [MPa]	Max C_3 [MPa]
Nybax long	120.881	149.513	-959.821	112.952	-0.0003	16625.872
Nybax short	62.719	132.167	-116.849	178.603	-302.768	1701.053

Table 4: Yeoh parameters range for Nybax long and short balloons.

Approximately 500 simulations were conducted for each sample type of unfolded balloons using a MATLAB® code that runs Abaqus simulations sequentially after suitable changes of input parameters. The simulations involved varying the parameters C_1, C_2, and C_3 within the initial maximum-minimum range. If a satisfactory fitting was not obtained with the initial range of parameters, the minimum and maximum values were adjusted to explore larger ranges. A pressure-deflection curve was generated for each successful simulation and compared against the corresponding experimental curve. For simulations that were unsuccessful, the code generated a line with $\Delta z = 0$. An example is shown in Figure 75.
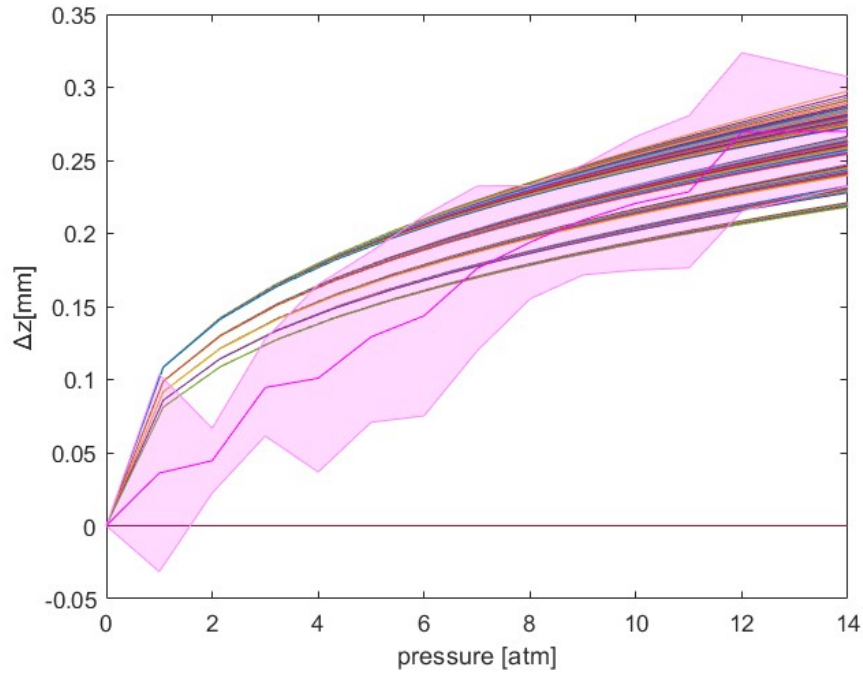
Figure 75: Example of 250 FEM simulations pressure-deflection curves (colored) compared with the mean and standard deviation of 8 experimental tests (pink).

For each FE pressure-deflection curve and the corresponding experimental curve, the differential deflection function $f(z)$, with respect to the reference state at 1atm, is calculated as:

$$f(z) = z_i - z(1\ atm)$$

Then, the error minimization criterion is computed as:

$$e = \sqrt{\frac{\sum_i (f_i^{exp} - f_i^{FEM})^2}{14}}$$

The numerical curve that exhibits the lowest error in relation to the experimental curve is selected as the most suitable fit. The Yeoh analytical parameters that correspond to this selected curve represent the behavior of the sample during the experimental bulge test.

Here, the final results of Nybax balloons (Tables 5,6 and Figures 76,77) are presented.

C_1 [MPa]	C_2 [MPa]	C_3 [MPa]	D_1 [MPa^{-1}]	D_2 [MPa^{-1}]	D_3 [MPa^{-1}]	e
52.7203	-366.6667	1500	0.000984	0	0	0.0034

Table 5: Yeoh analytic parameters of the fitting FE curve for Nybax long balloons.
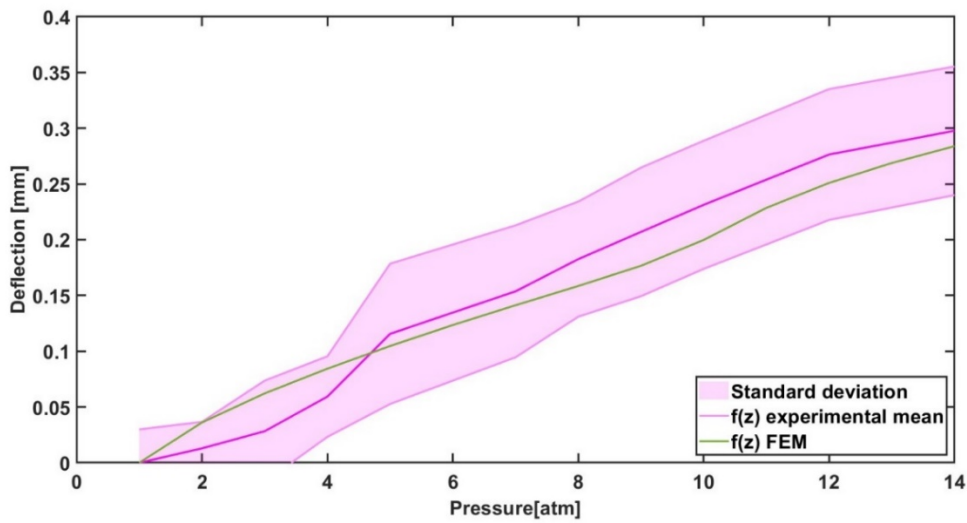
Figure 76: f^{exp} (mean of 6 samples) compared with the fitting f^{FEM} for Nybax long balloons.

C₁ [MPa]	C₂ [MPa]	C₃ [MPa]	D₁ [MPa⁻¹]	D₂ [MPa⁻¹]	D₃ [MPa⁻¹]	e
62.7198	-400	1422.2	0.000984	0	0	0.0035

Table 6: Yeoh analytic parameters of the fitting FE curve for Nybax short balloons.
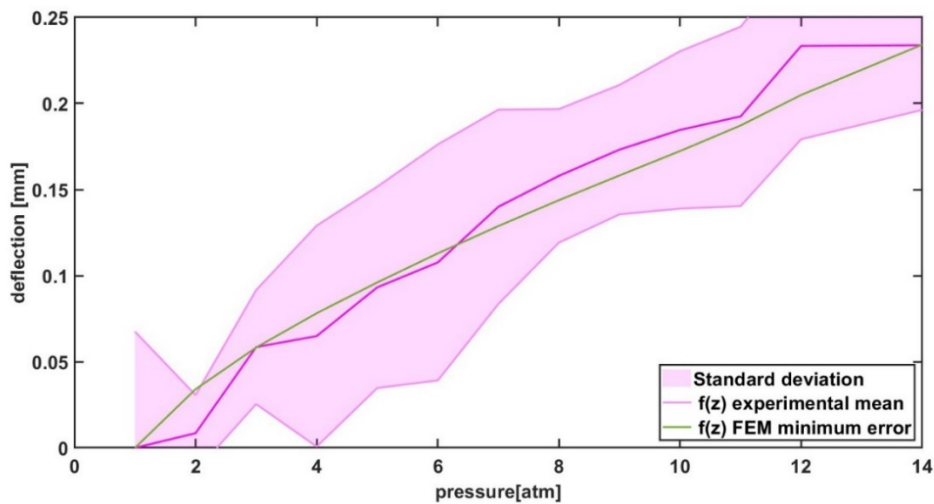
Figure 77: f^{exp} (mean of 8 samples) compared with the fitting f^{FEM} for Nybax short balloons.

It was decided to attempt using both of the parameter combinations chosen for unfolded balloon behavior to describe the responses of polyamide folded balloons. In the Table 7 are the results obtained in both cases, and in Figure 78 are presented the respective curves.

	C₁ [MPa]	C₂ [MPa]	C₃ [MPa]	D₁ [MPa⁻¹]	D₂ [MPa⁻¹]	D₃ [MPa⁻¹]	e
(1)	62.7198	-400	1422.2	0.000984	0	0	0.0100
(2)	52.7203	-366.6667	1500	0.000984	0	0	0.0131

Table 7: Yeoh analytic parameters of the fitting FE curve for polyamide folded balloons.
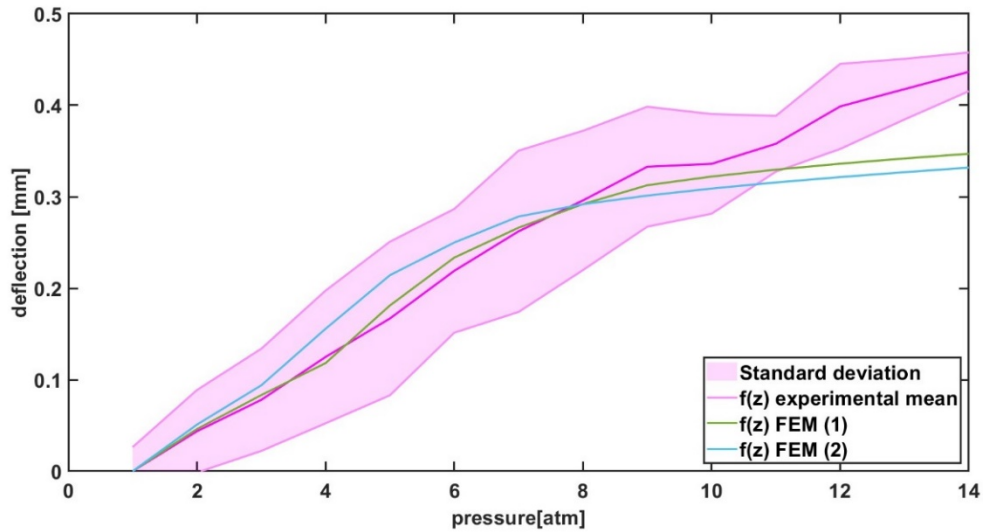
Figure 78: f^{exp} of polyamide folded balloons (mean of 7 samples) compared with the fitting f^{FEM} obtained using parameters combination (1) and (2) in Table 7.

By comparing the curves and calculating the minimum error, parameter set (1) (Table 7) turns out to be the best choice to approximate the behavior of Nylon folded balloons. However, the numerical pressure-deflection curve does not fit the experimental curve well for pressures greater than 8 atm.

Long balloons	C₁ [MPa]	C₂ [MPa]	C₃ [MPa]
Minimum	120.881	-959.821	-0.0003
Maximum	149.513	112.952	16625.872
Mean	128.440	-148.680	2735.705
Standard deviation	10.540	366.417	5689.280

Table 8: Mean and standard deviation of Yeoh parameters of Nybax long balloons.

The results obtained by fitting the FE curve with the experimental bulge test data show the values of C_1, C_2, and C_3 that provide the best fit for the given experimental data. These values are C_1=52.7203 MPa, C_2=-366.6667 MPa, and C_3=1500 MPa for Nybax long balloons. In this case, C_1 does not lie within the uniaxial test range, whereas C_2 and C_3 are within the anticipated range. One observation should be made about the value of C_3: the width of the minimum-maximum range found experimentally, is indeed very high, this could be due to the fact that this is a less sensitive parameter, so varying its value, even by a large amount, it will change a little the obtained curve (Table 8).

Short balloons	C_1 [MPa]	C_2 [MPa]	C_3 [MPa]
Minimum	62.719	-116.849	-302.768
Maximum	132.167	178.603	1701.053
Mean	98.626	60.681	239.363
Standard deviation	21.021	107.906	646.492

Table 9: Mean and standard deviation of Yeoh parameters of Nybax short balloons.

For Nybax short balloons, the values of C_1, C_2, C_3 are, respectively: 62.719 MPa, -400 MPa and 1422.2 MPa.

C_1 happens to be the same as the minimum value founded with uniaxial tensile tests, while C_3 lies in the anticipated range. However, C_2 is not consistent with the expected results.

Comparing these results to the initial ranges, mean, and standard deviations (Table 9), it is clear that the values obtained through fitting are significantly different from the initial ranges and mean values. This suggests that the initial ranges were too broad or that the model is highly nonlinear and sensitive to small changes in parameter values. The large standard deviation values also indicate that the model is highly sensitive to parameter values. C_1 tends to stay in a predefined range of values, about an order of magnitude smaller than C_2. It is also the one that has more influence on the slope of the curve. While C_2 and C_3, being higher degree terms are less sensitive, and their variation has less influence on the variation of the curve itself.

However, it is necessary to consider that the starting parameters were obtained by uniaxial tensile tests, which is different from the bulge test, as it loads the material in a biaxial configuration. This gives as results only indicative parameters because the material's loading and its subsequent response are different. This may partly justify why different values of Yeoh's model parameters were obtained.

Overall, it appears that the Yeoh hyperelastic model can fit the experimental data reasonably well. The present study did not reveal a discernible correlation between the variation of a single parameter and changes in the slope of the curve. Apparently, it is only the combination of the three parameters that give changings in the curve.

To evaluate the consistency of the results obtained, it was decided to compare the inflation profile of the surfaces obtained through finite element simulations with the surfaces captured by Lext during the bulge test.

The data obtained from the microscope is subjected to grid fitting using MATLAB®, which enables the determination of the function f(x,y). This function describes the displacement along the z-axis for each point (x,y) on the surface after fitting (Figure 79).
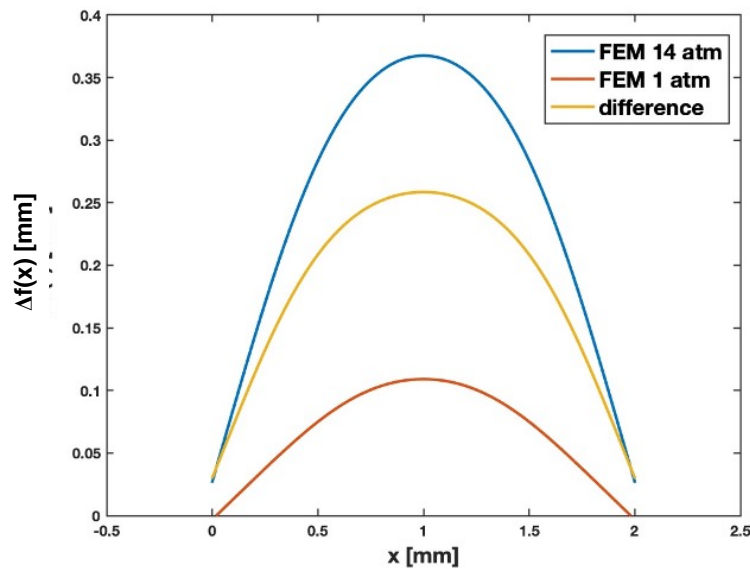
Figure 79: Example of f(x) at 14 atm (blue), f(x) at 1 atm (orange), $\Delta f(x)$ (yellow) computed from the surface obtained by Abaqus.

The comparison between $\Delta f(x)^{exp}$ and $\Delta f(x)^{FEM}$ is presented for long and short balloons in Figures 80 and 81, respectively.
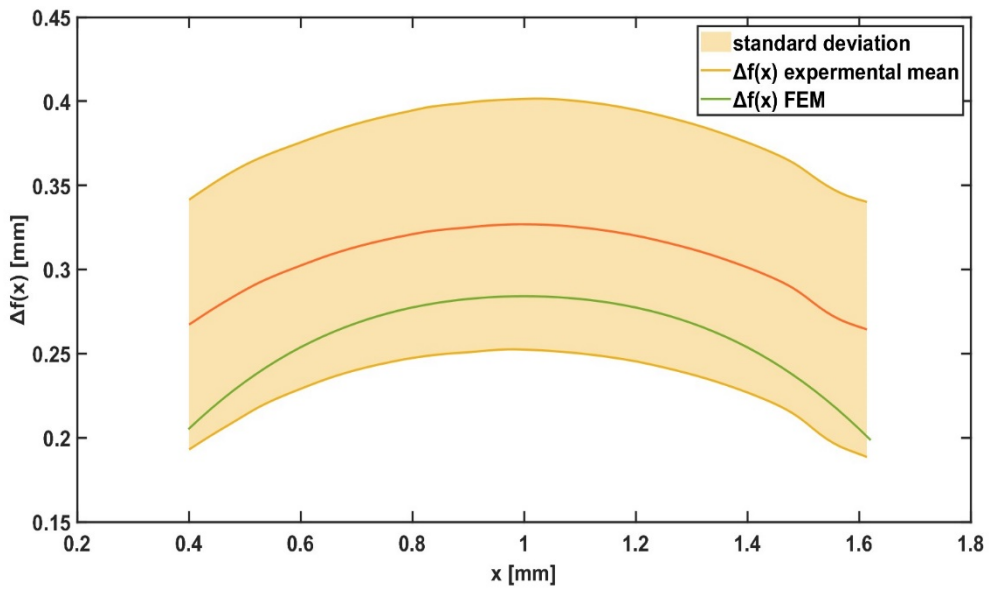
Figure 80: $\Delta f(x)^{exp}$ (mean of 6 samples) and $\Delta f(x)^{FEM}$ of Nybax long balloons.
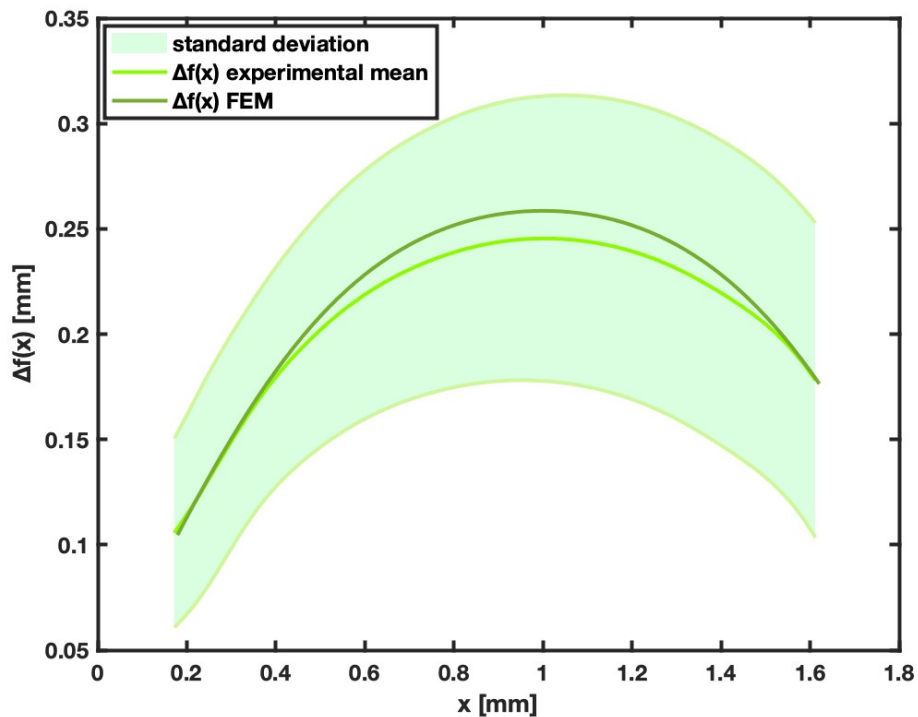
Figure 81: $\Delta f(x)^{exp}$ (mean of 8 samples) and $\Delta f(x)^{FEM}$ of Nybax short balloons.

From the graphs in Figures 80,81 it can be seen that the Yeoh model set with the selected triplets is indeed representative of the curvature profile for unfolded balloons.

As for the folded balloons, as already expected there is a mismatch of the curvature profiles starting from the 8-atmosphere configuration (Figure 82).
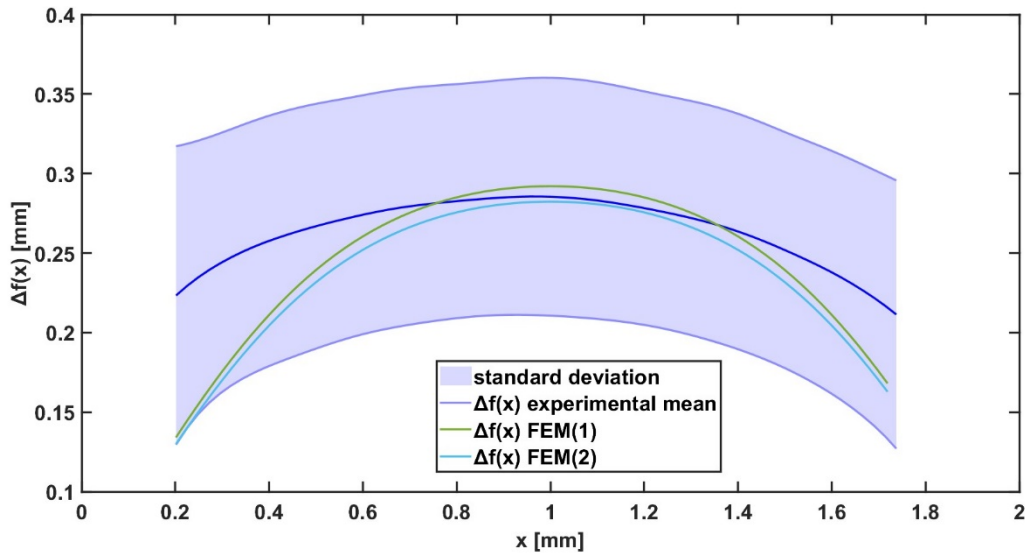
Figure 82: $\Delta f(x)^{exp}$ (mean of 7 samples) and $\Delta f(x)^{FEM}$ of polyamide folded balloons at 8 atm.

This inconsistency is present in both scenario (1) and (2). In fact, it becomes even clearer that the curves are badly approximated when examining what happens to the curvature profile for the 12-atmosphere configuration, as shown in Figure 83.
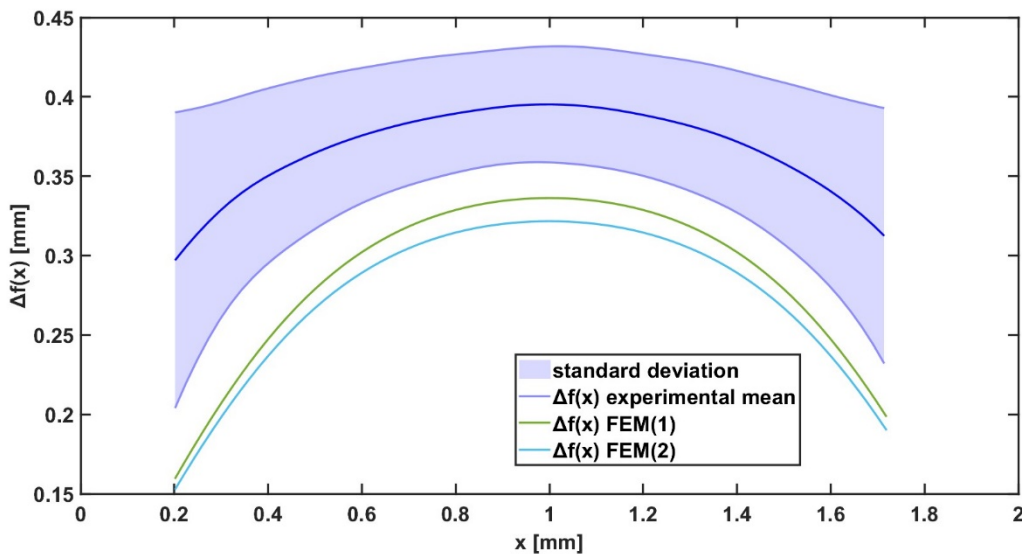
Figure 83: $\Delta f(x)^{exp}$ (mean of 7 samples) and $\Delta f(x)^{FEM}$ polyamide folded balloons at 12 atm.

Overall, the results obtained in this study demonstrate that the deflection profiles generated by the Finite Element Method are consistent with the experimentally determined mean and standard deviation, falling within an acceptable range of error. This finding is indicative of the reliability of the numerical model in predicting the deflection behavior of the structure under consideration.

Research should be improved with respect to the parameters chosen for polyamide folded balloons. Remember that the constitutive parameters of Yeoh's model discovered for unfolded Nybax balloons, are the same used for these samples. As a composite of Nylon and Pebax, it's conceivable that they aren't entirely accurate descriptions of Nylon alone.

Pebax films from the University of Montpellier have been described differently than balloons. Indeed, an elastic-plastic model has been used for this latter sample type, differently from the balloons which were modelled thorough hyperelastic constitutive equations see Section 4.1. Therefore, a distinct set of material input parameters were used to run the same Abaqus simulation that models the bulge test.

Material parameters are chosen by referring to experimental uniaxial tensile tests: E= 300 MPa, ν=0.45, describing the elastic behavior; Yield Stress= 27 MPa, Plastic strain=0, describing the plastic behavior, as stated in Section 4.1. These values were used to run the numerical simulation.

The comparison between the experimental curve (f^{exp}) and the numerical one (f^{FEM}) is shown in Figure 84.
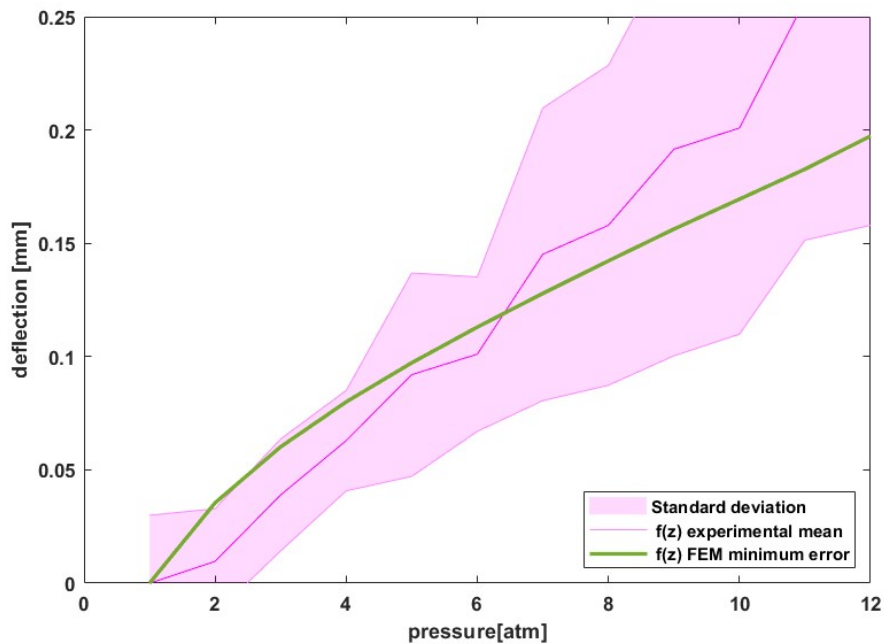
Figure 84: f^{exp} (mean of 5 samples) compared with the fitting f^{FEM} of Pebax films.

The calculated error of 0.0083 is comparable to the results obtained for the balloons (0.0035-0.0034). This suggests that the Abaqus model accurately represents the material inflation during the experimental bulge test.

As in previous cases, the inflation profile generated by the FEM simulation was compared to the experimental surfaces to verify the consistency of the results (Figure 85).
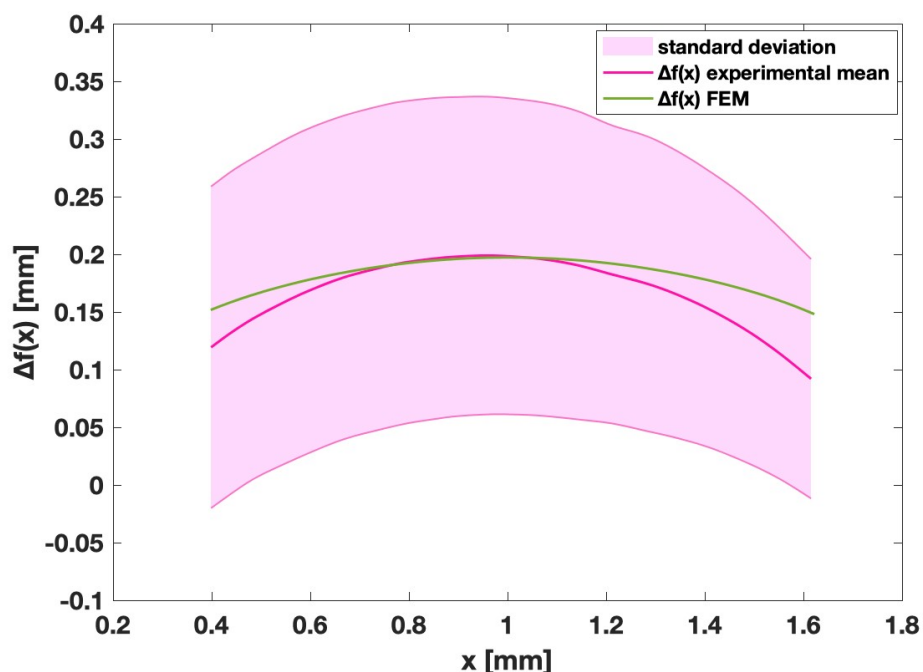
Figure 85: $\Delta f(x)^{exp}$ (mean of 5 samples) and $\Delta f(x)^{FEM}$ of Pebax films.

The results of the numerical simulation fall within the same range of variation as the experimental data, suggesting that the simulation is a reasonable representation of the physical system. However, there are some discrepancies between the two curvatures, suggesting that there may be some limitations or inaccuracies in the simulation. One possible explanation for this discrepancy is that the polymeric material in the simulation reaches plasticity (σ_y = 27 MPa) before the maximum pressure of 14 atm is reached. As a result, the simulation did not evaluate the behavior of the material up to the maximum pressure but stopped at 12 atm, since necking occurred at the point of contact between the material and the metal plate. Indeed, necking at the contact ridge implies strain concentration, which may substantially reduce the curvature in the central region of the circular patch.

In Figure 86 it can be seen that there is a concentration of shear deformations at the contact point, where the material has reached its yielding point. The stress in the same point (Figure 87) has reached the value 27 MPa, corresponding to the σ_y found in the uniaxial tensile tests.

80
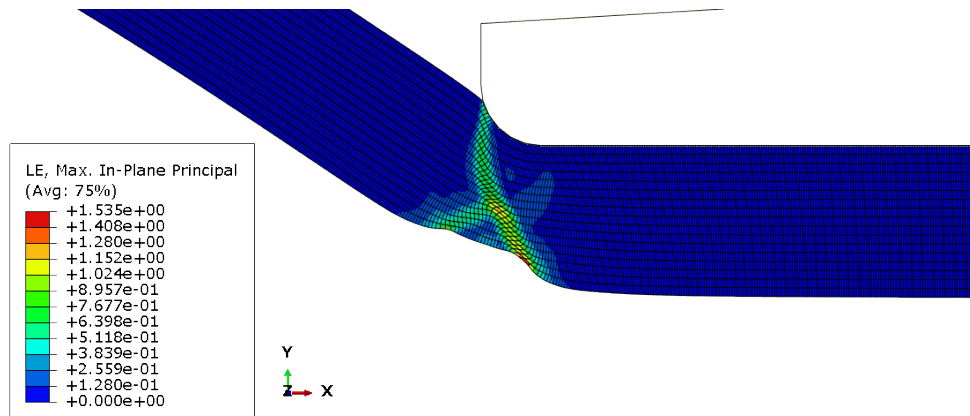
Figure 86: Shear deformation at the contact point between the material and the metal plate.
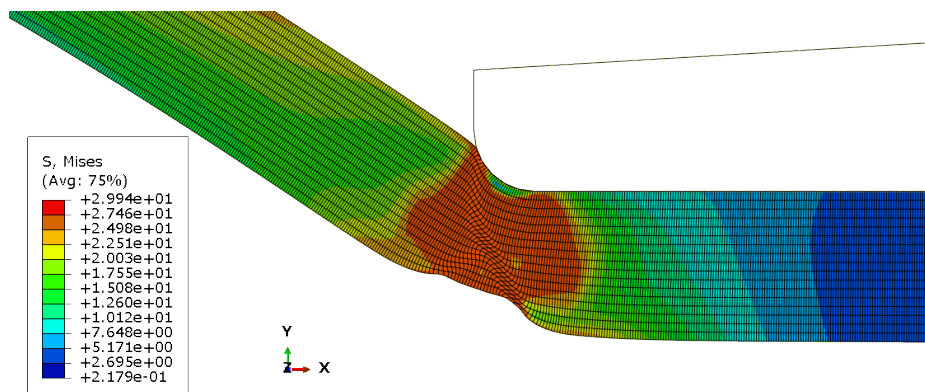
Figure 87: Stress concentration at the contact point between the material and the metal plate.

It was intended to confirm this observation through experimental analysis of the sample after the bulge test was completed. However, due to the strong cohesion of the multilayer structure (tape-sample-tape) and the small size of the specimen, the material sample could not be disassembled without peeling it off the tape. Therefore, it was not possible to examine the material alone and there is no experimental evidence to support the notion that the material undergoes plastic deformation at the contact edges between the sample and the metal plate.

Again, further refinement of the mesh in the area of interest, would be a possibility to improve the Abaqus model, but this hypothesis is left to future developments of the work.

Validated finite element models can provide information that cannot be gathered from the experimental measures. In this bulge experiments, the finite element models can be used to infer the stress and strain occurring in the central region of the patch in which a biaxial loading occur. In particular, the homogeneity of the strain distribution in the central area is relevant to study the coating behavior.

The strain (i.e. Logarithmic strain) profile along the radius of the bulge window (Figure 88), is roughly constant for $0 < r < 0.2$ (i.e., in the center). Therefore, it can be reasonably assumed that the central region with diameter 0.4-0.5 mm is subjected to a fairly homogeneous stress and strain.
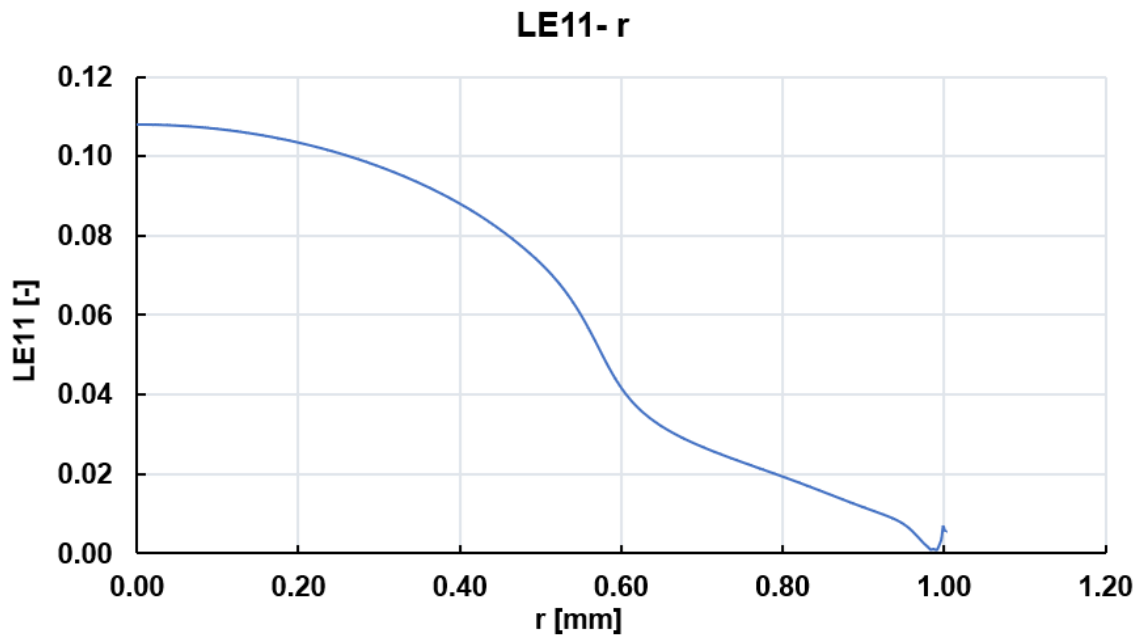
Figure 88: Logarithmic strain in x-direction (LE11) along the radius of the bulge window.

Given that the material is subjected to a biaxial loading, as shown in Figure 89, one must consider stresses and strains in both x- and z-direction.
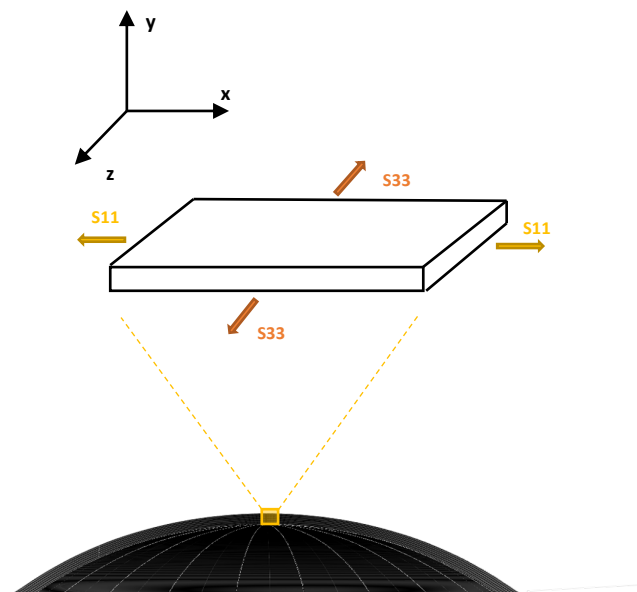
Figure 89: Schematic loading of an infinitesimal part of the polymeric material during the bulge test.

Logarithmic strains (LE11 and LE33) and Cauchy stresses (S11 and S33) are evaluated for the node in r=0 (Figure 90).

For the sake of simplicity, regarding the description of folded balloons it is decided to use the simulation (1) (Table 7).
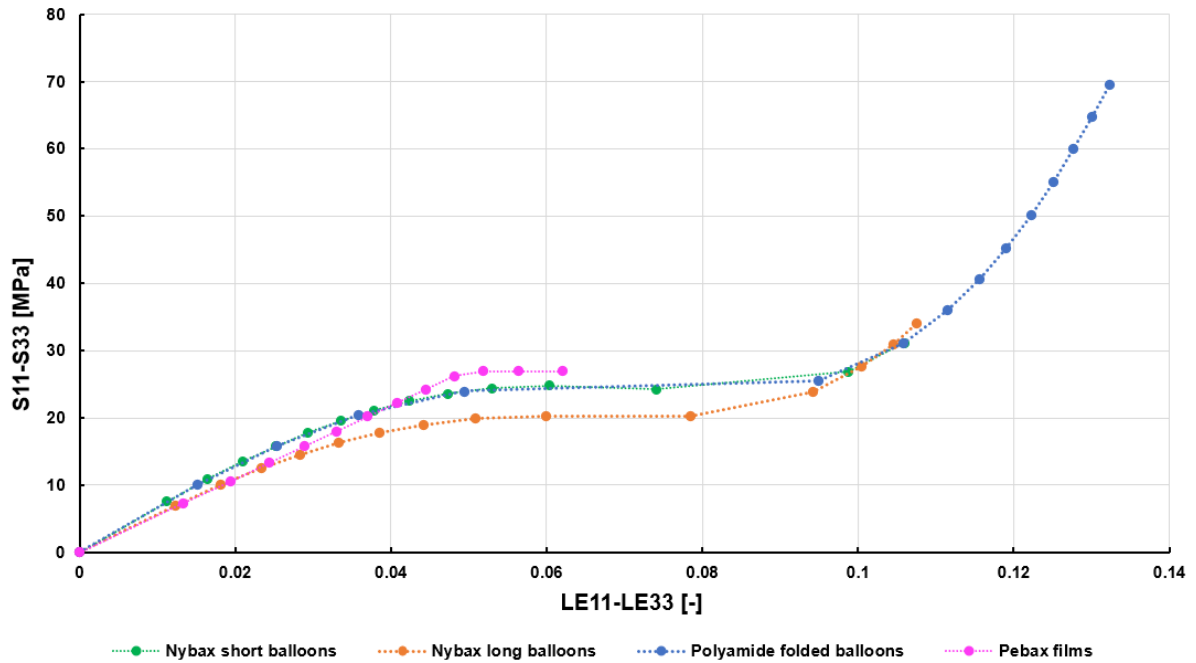
Figure 90: Logarithmic strains and Cauchy stresses evaluated on the center of the material's surface (r=0) in Finite Element simulations.

It is important to remember that the simulation corresponding to Montpellier's Pebax films stopped at 12 atmospheres for reasons of non-convergence.

Since the bulge test loads the material through hydraulic pressure, it is interesting to see how the surface strain varies with the applied pressure. The nominal strain is computed as follows: $\varepsilon_{11} = e^{(LE_{11})} - 1$ and reported against the pressure in the Figure 91.
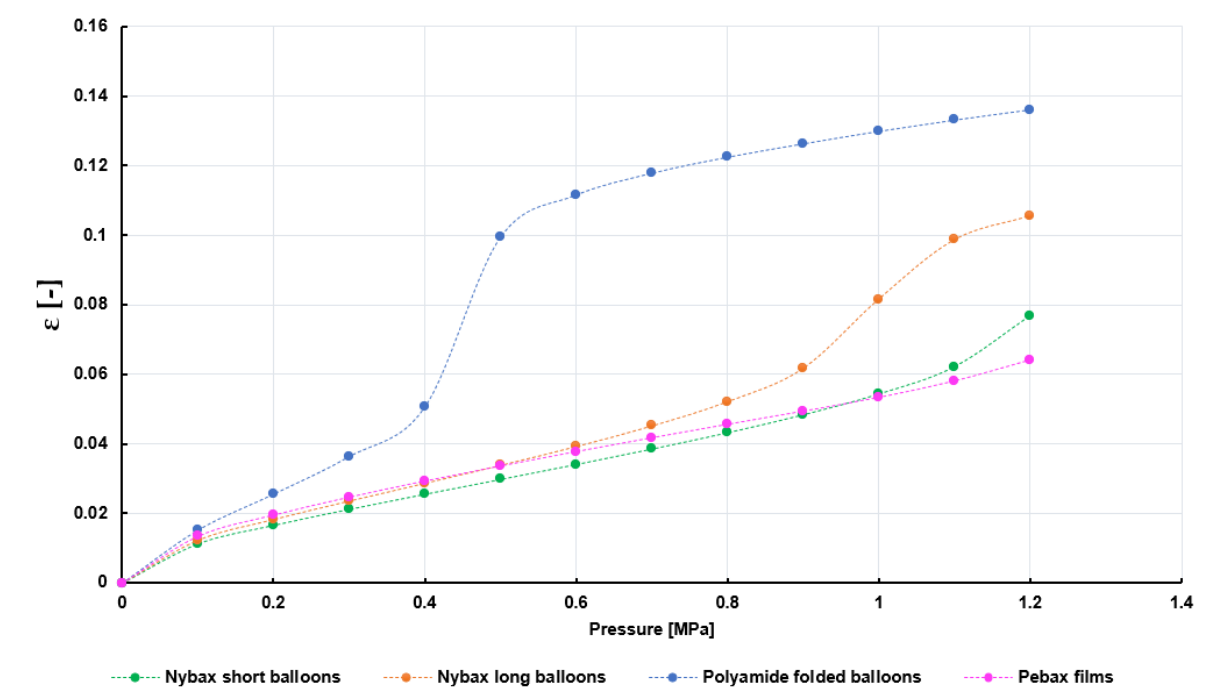
Figure 91: Nominal strain evaluated on the center of the material's surface (r=0) in Abaqus simulations.

To ensure consistency in the results, strain trends up to 1.2 MPa are reported in the graph in Figure. Among the different materials, the folded Nylon balloons exhibit the highest strain, reaching 14.14% at the maximum pressure, as they are the thinner samples. The long unfolded balloons show a strain of 10.5%, while the short ones reach 7.6%. On the other hand, the Pebax films display the lowest strain with 6.3%.

Since stress and strains are not available in bulge test experimental measurements, it is presumed that the simulations displaying an accurate pressure-deflection matching with experiments will provide the surface strain of the membrane upon bulging. This will make it possible to identify the critical strain at which coating fracture happens in coated samples.

84

4.3.3. Coated samples

The polymer-coated samples, both the spray-coated and micropipette-coated, as well as the drug-polymer-coated samples have been tested through the bulge test. The confocal laser microscope images that were recorded during the experiment are reported at each pressure level.

Polymer – spray – coated samples

The results indicate that the coating structure remained relatively stable between pressures of 1 atm and 6 atm, as depicted in Figures 92(a) and 92(b). However, the coating started to crack at 7 atm, as shown in Figure 92(c), where the deformation of the underlying material is 4.17%. Subsequently, a considerable number of fractures became evident in the upcoming configurations (Figures 92(d), 92(e), 92(f)), particularly in the final stage, where the pressure reached 11 atm and consequently a deformation of 5.8%, as illustrated in Figures 92(g).
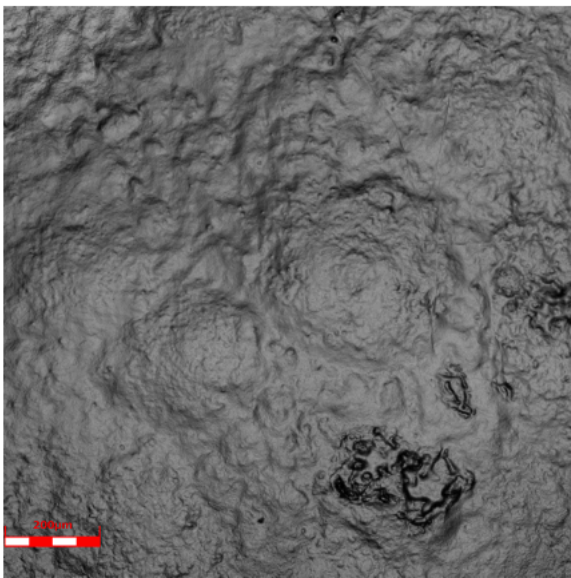
(a) 1 atm
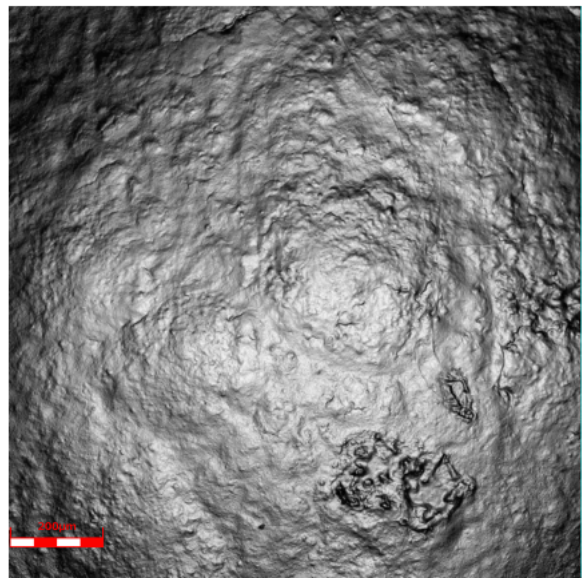
(b) 6 atm
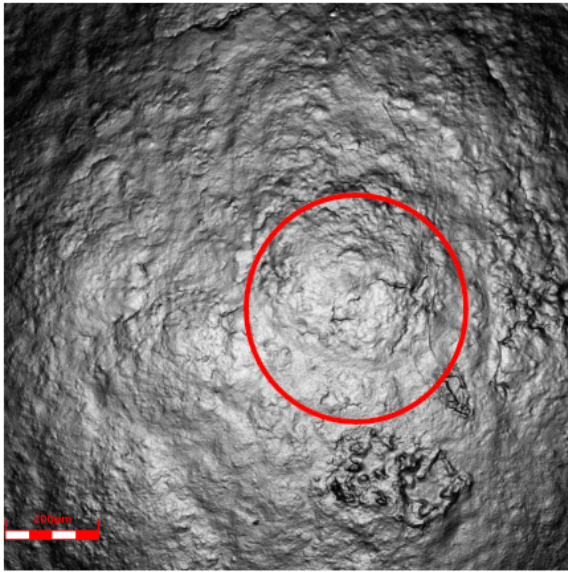
(c) 7 atm
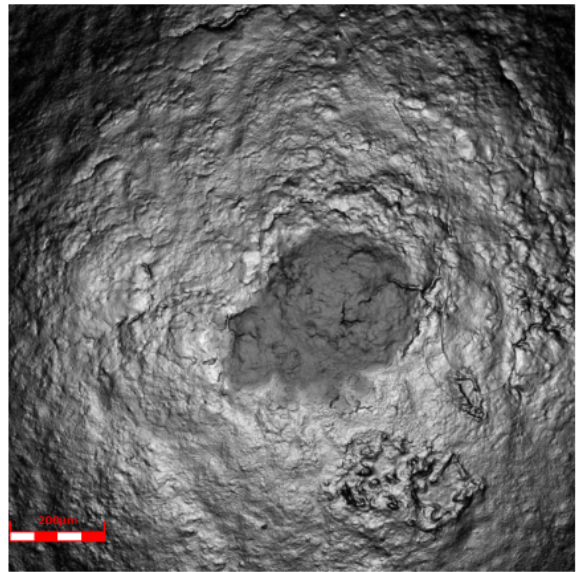
(d) 8 atm
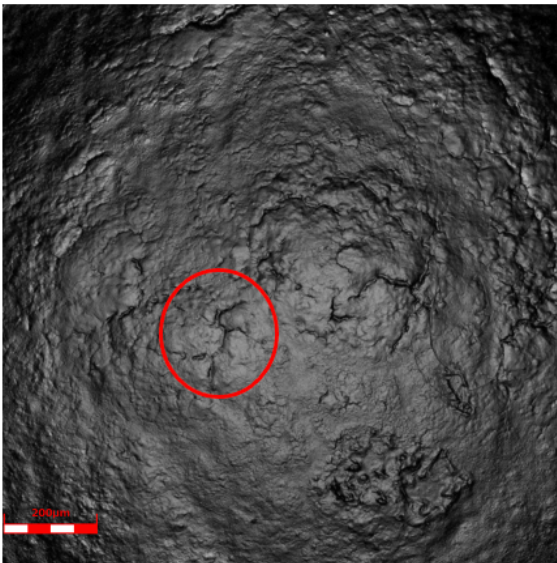
(e) 9 atm
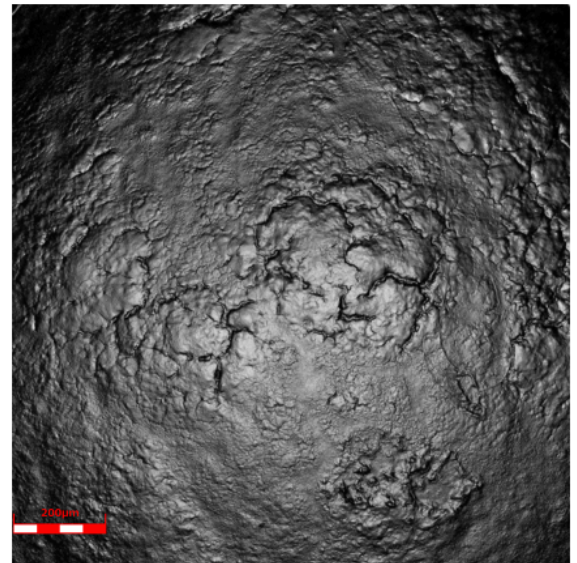
(f) 10 atm
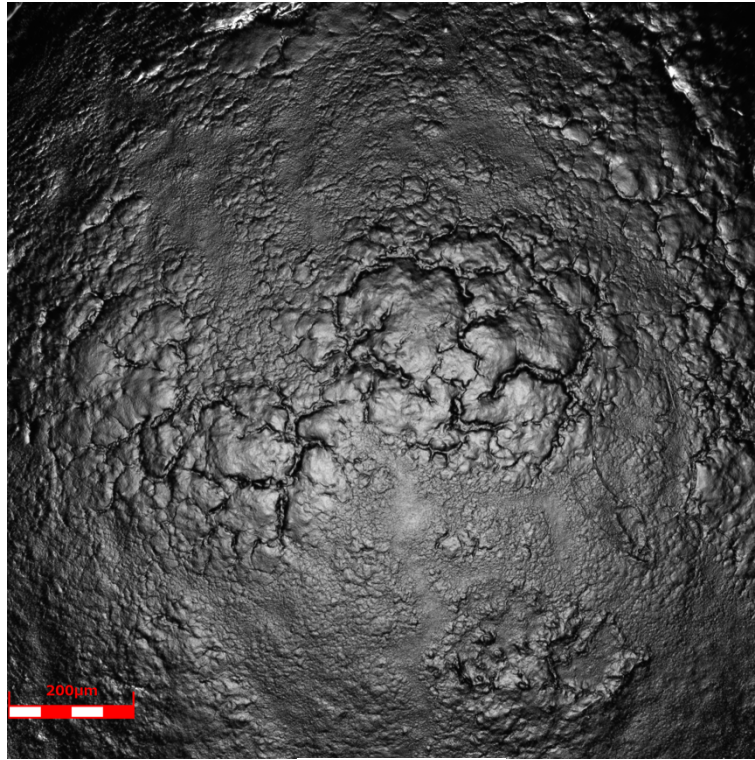
(g) 11 atm

Figure 92: Image sequences of the polymer-spray-coated Pebax film during the inflation.

Polymer – micropipette – coated samples

Considering the unique nature of this particular coating, two different sample types were prepared: i) sample taken in area with coating accumulation (see blue circle in Figure 93) and ii) sample taken on area exhibiting more homogeneous coating (yellow circle in Figure 93).
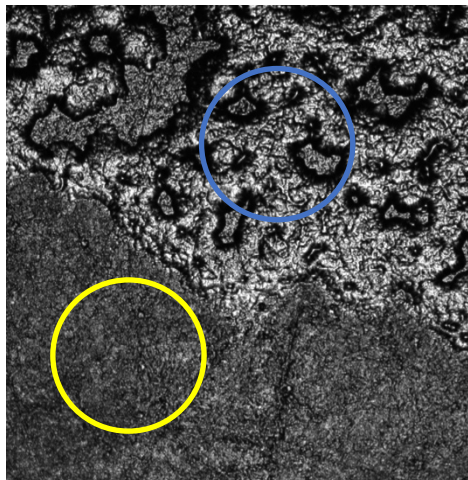
Figure 93: Polymer – micropipette – coated sample taken from the region exhibiting coating accumulations (circle in blue) and from the more uniform zone (circle in yellow).

Upon subjecting the samples to a bulge test, it was observed that the integrity of the excipient layer remained unaffected in both cases, as indicated by the absence of any discernible differences between the initial configuration (figure 94(a) and 94(c)) and final configurations (figure 94(b) and 94(d)).
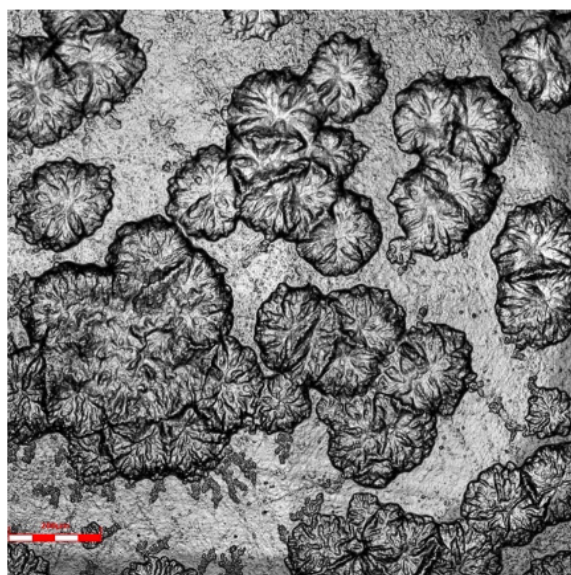
(a) 1 atm
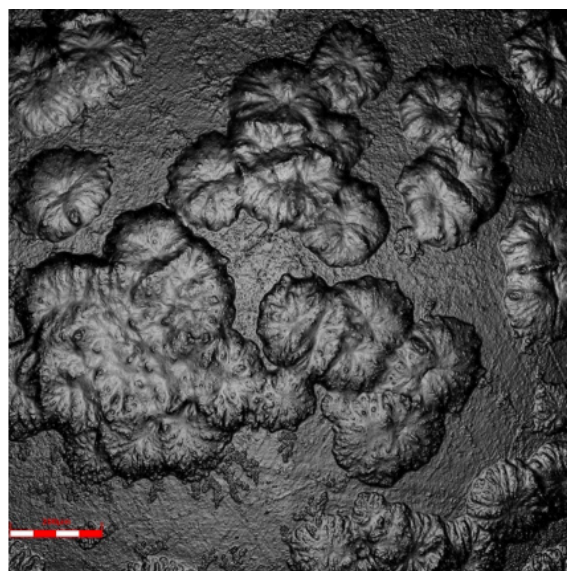
(b) 11 atm
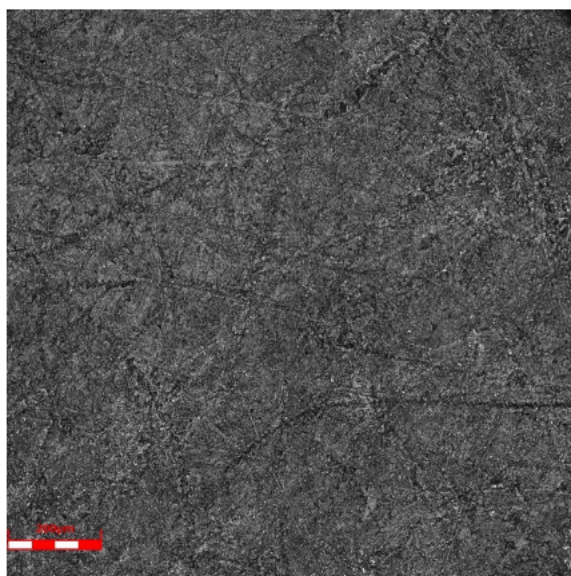
(c) 1 atm
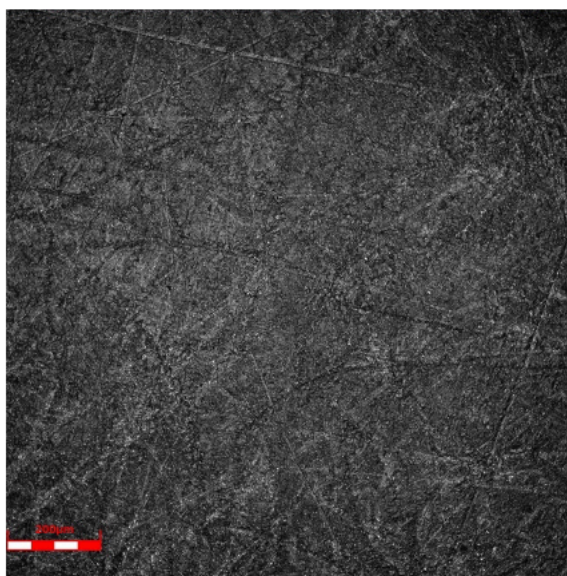
(d) 11 atm

Figure 94: Images captured with the confocal laser microscope at pressure 1 atm ((a),(c)) and at pressure 11 atm ((b),(d)) during the bulge test. In the top images, the sample is taken from zone 1, while in the bottom from zone 2.

The pressure-deflection curves obtained in the two different cases are shown in Figure 95, where it is reported an average made on 3 samples each. It can be seen that the sample taken in the zone where there are coating accumulations (zone 1) inflates more than the sample taken in the more uniform zone (zone 2). However, the explanation of this phenomenon is still to be found.
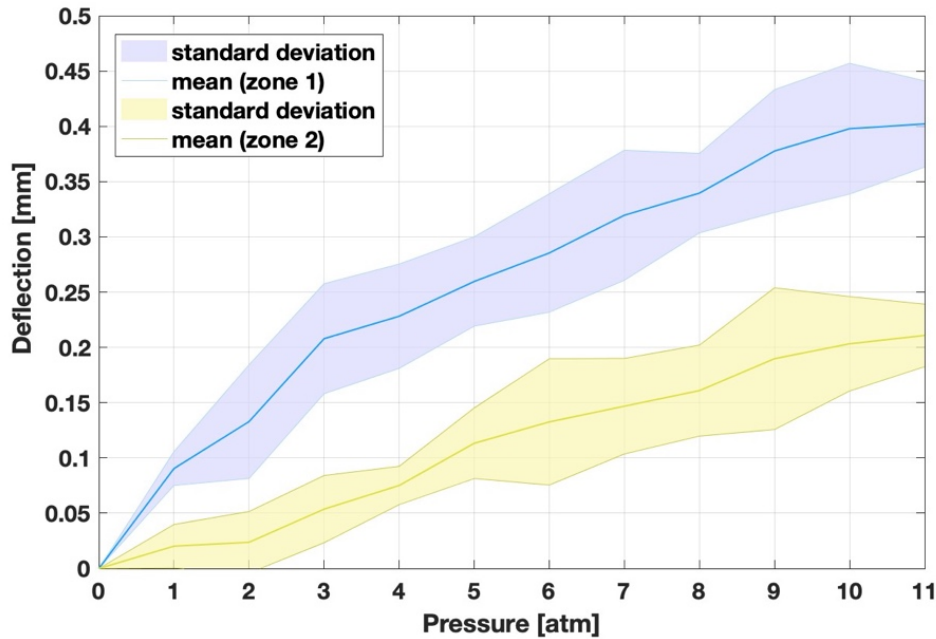
Figure 95: Pressure-deflection curve of the sample taken in from zone 1 in blue and pressure-deflection curve of the sample taken from zone 2 in yellow.

The graph in Figure 96 shows the pressure-deflection curves obtained by testing two specimens of samples with coating deposited via the spray technique and three samples with coating deposited via the micro-pipette technique. For this comparison, it was decided to take into account the samples taken from the region exhibiting coating accumulations.

It appears that the micro-pipette-coated samples inflate more at lower pressure values, but plateau around 10 atmospheres, while the values of the spray-coated ones continue to increase.
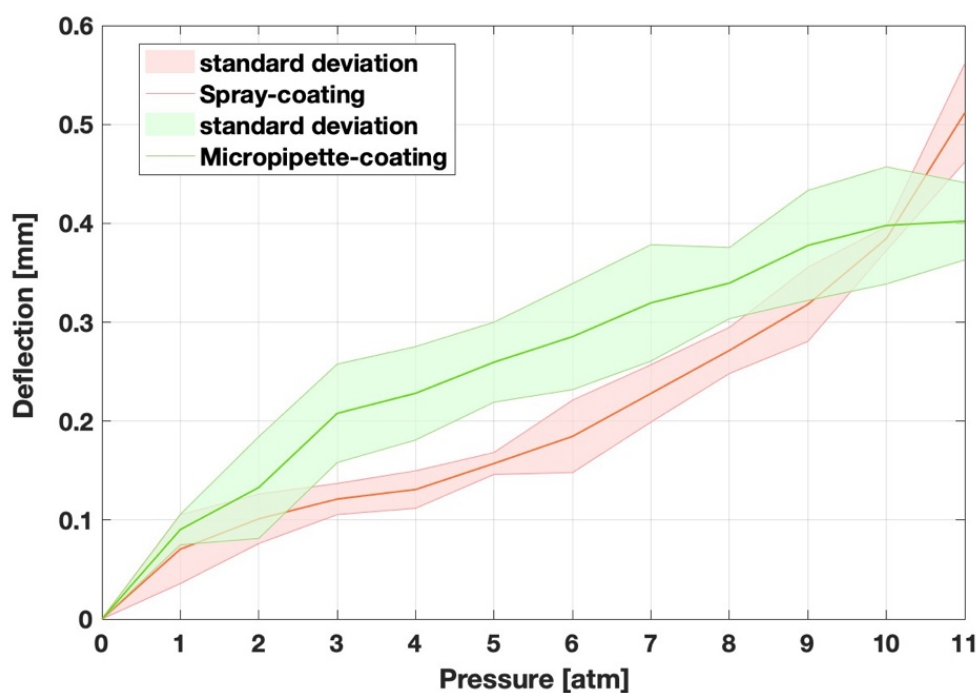
Figure 96: Pressure-deflection curves of samples with coating deposited via the spray technique (in orange) and samples with coating deposited via the micro-pipette technique (in green).

Drug – excipient – coated samples

In the experimental studies conducted on the drug-polymer-coated specimens, it has been observed that cracks begin to appear at a pressure of 4 atm (Figure 97(b)). Furthermore, at a pressure of 8 atm, corresponding to a deformation of the underlying material of 4.55%, the fractures open up (Figure 97(d)).
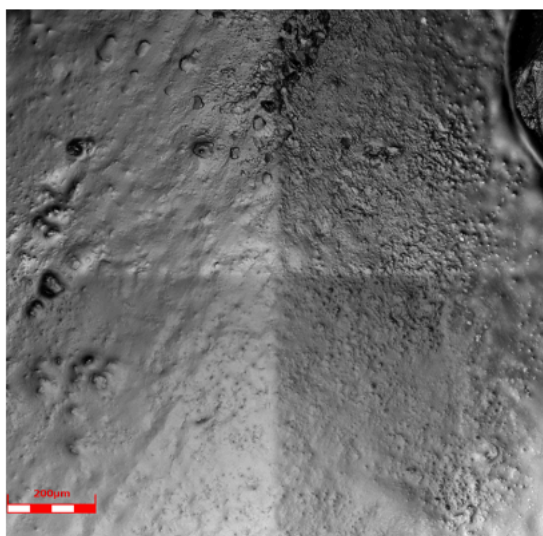
(a) 1 atm
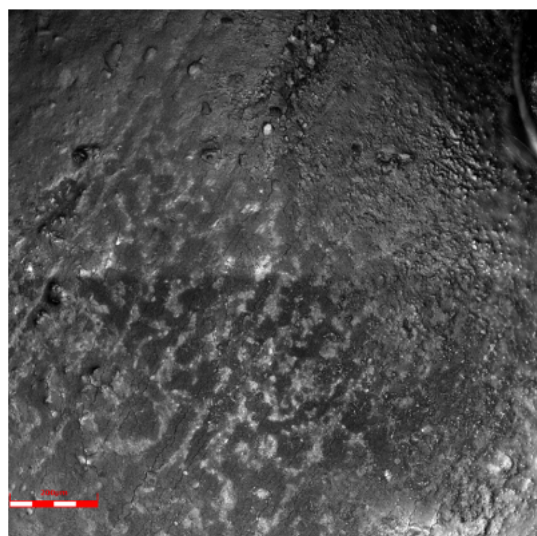
(b) 4 atm
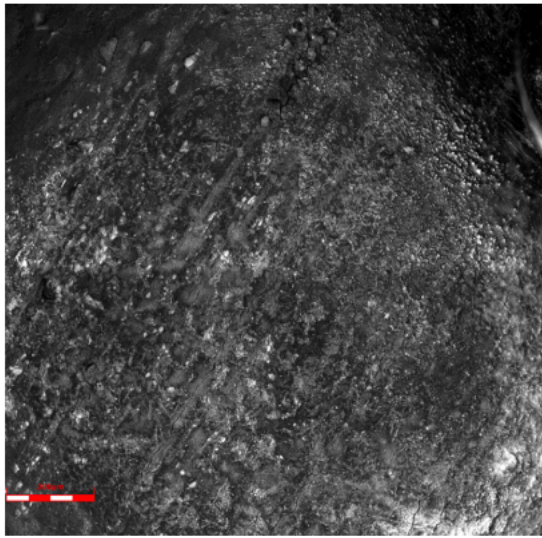
(c) 6 atm
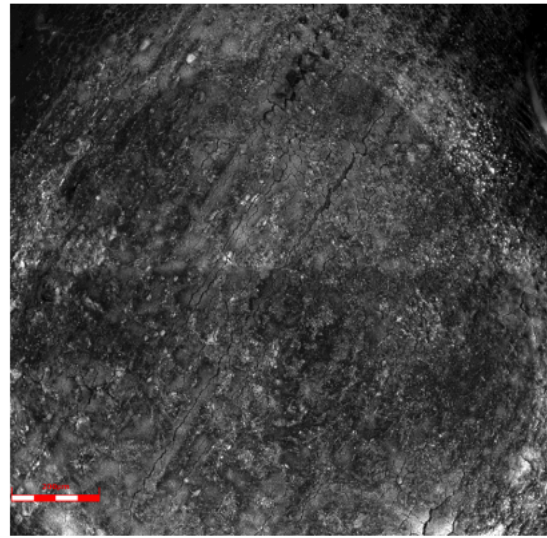
(d) 8 atm
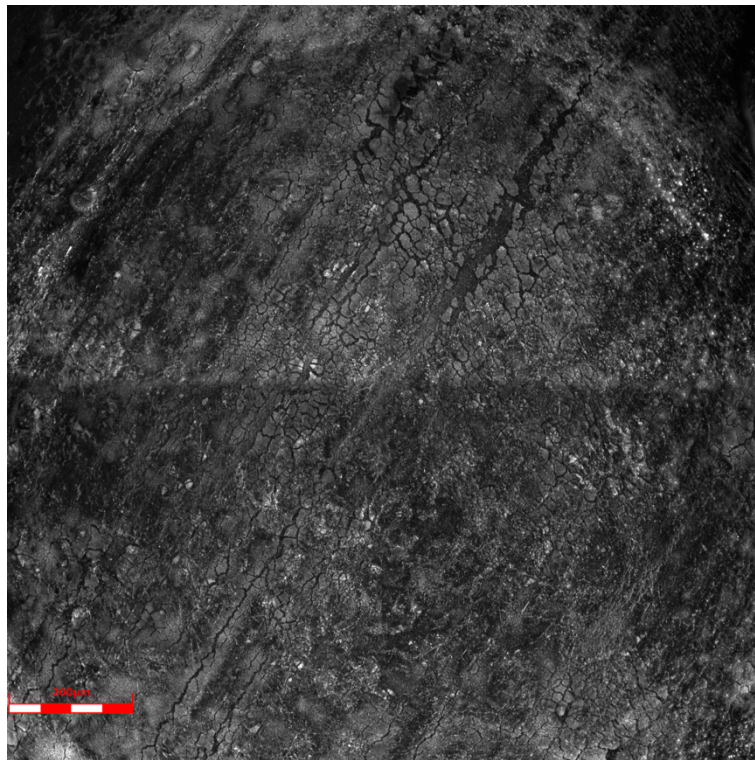
(e) 9 atm

Figure 97: Image sequence of drug-coated Pebax film during inflation

The pressure-deflection curve, shown in Figure 98, is obtained by making the average on 8 drug – polymer – coated samples that have been subjected to the bulge test.
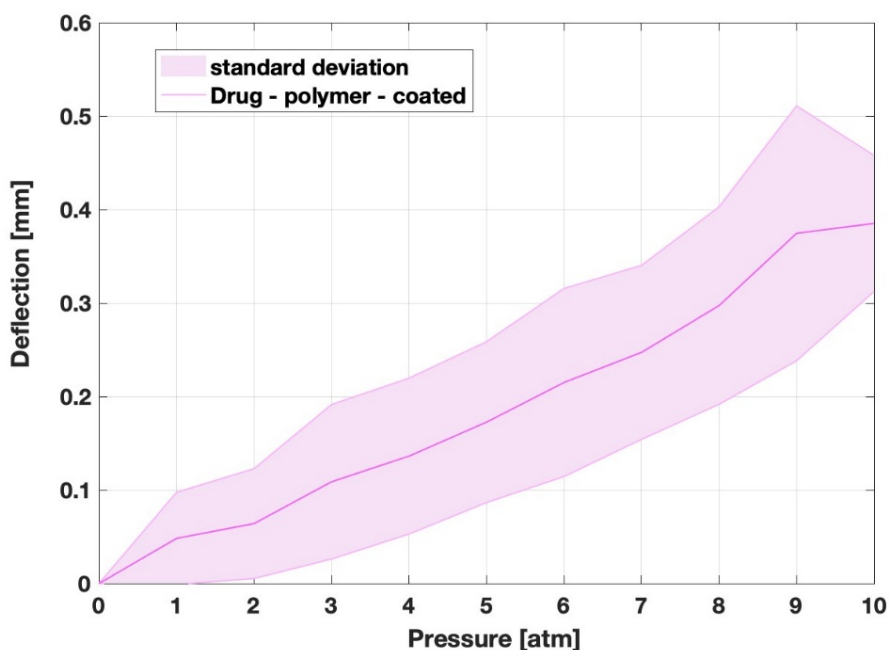
Figure 98: Pressure-deflection curve of drug – polymer – coated samples.

Comparison between uncoated and coated samples

A comparison was made between various types of Pebax material, including uncoated, spray-polymer-coated, micropipette-coated, and drug-polymer-coated samples. The objective was to evaluate the mechanical response of the substrate-excipient system by investigate the deflection behavior, which was measure through a series of tests.

Upon analysis of the graph (Figure 99), it was observed that all samples exhibited similar trends. However, the uncoated samples demonstrated lower deflection values compared to their coated counterparts. This result was unexpected and prompted further investigation. Two potential factors were identified as possible explanations for this observation: the influence of the coating on the underlying material, or a difference in the thickness of the samples. However, due to limitations in the measurement of the coating thickness, a precise determination could not be made.
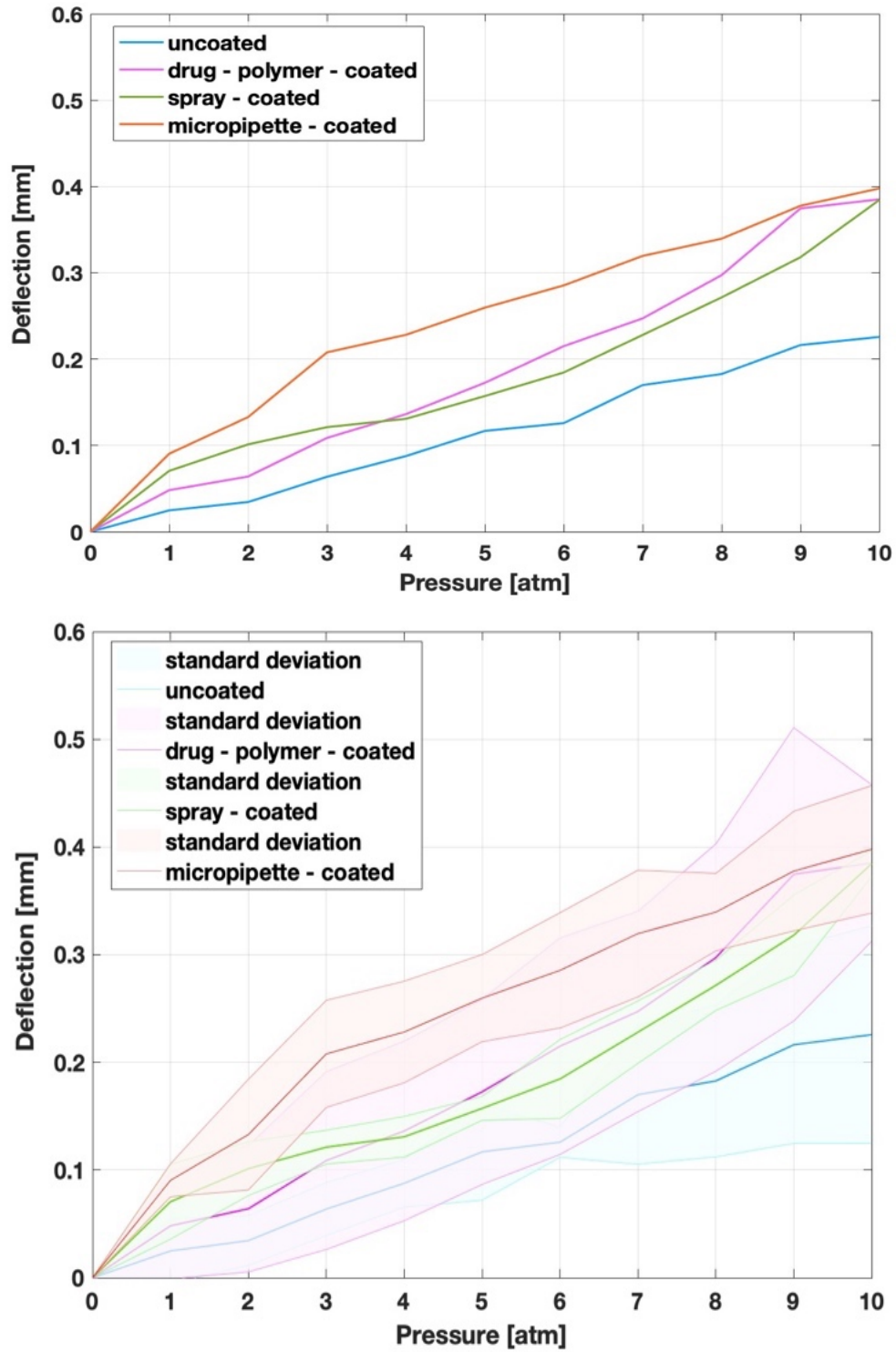
Figure 99: Comparison between pressure-deflection mean curves of uncoated, spray-polymer-coated, micropipette-coated, and drug-polymer-coated samples (on the top) and the same curves with the standard deviation (on the bottom).

4.4. Isotropy

The isotropy property of the material has been investigated in two ways. The first is to calculate the degree of anisotropy (DA) from the curvature for each pressure increment as:

$$DA_i = \frac{C_{max} - C_{min}}{C_{min}}\big|_i$$

where i ranges from the first pressor increment to the last one reached. C_{min} and C_{max} are minimum and maximum curvature, respectively.

If the two curvatures are equal, DA is found to be zero, indicating a deformed configuration with circular height contour lines and thus material isotropy. On the other hand, if the value of DA deviates from zero, it indicates a higher degree of material anisotropy, which is demonstrated by an elliptical deformed configuration.

The curves in the Figure 100 represent the variation of DA as a function of Δp. It has been decided to calculate DA from the pressure of 2 atm since at a pressure of 1 atm a higher value is obtained due to the effect of the initial configuration found after tightening the bolts. The mean and relative standard deviation has been calculated for each sample class. From the DA values obtained, the isotropy of the materials can be affirmed.
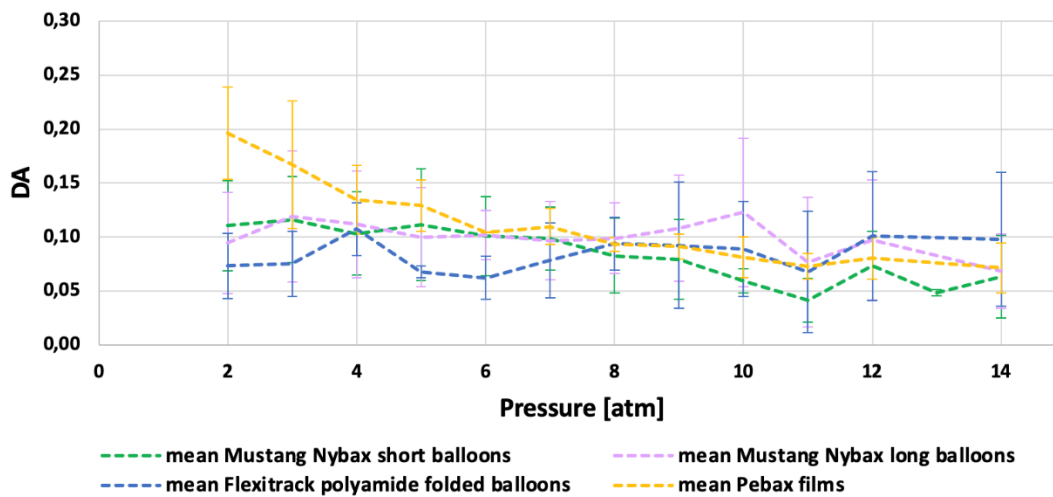
Figure 100: Graphs of the trend in the degree of anisotropy as a function of pressure increment, for all specimens tested.

The average degree of anisotropy computed over the different pressures was calculated for each sample class.

Samples/Materials	DA
Mustang Nybax short balloons	0,08380
Mustang Nybax long balloons	0,0997
Flexitack polyamide folded balloons	0,0839
Pebax films	0,1110

Table 10: Average DA for each type of sample tested

In figure 101, DA is reported with respect to maximum displacement (Δz) on the horizontal axes instead of the applied incremental pressure. The results clearly reveal that the DA calculated on the different materials under consideration (Nybax, Pebax, polyamide) is close to zero.
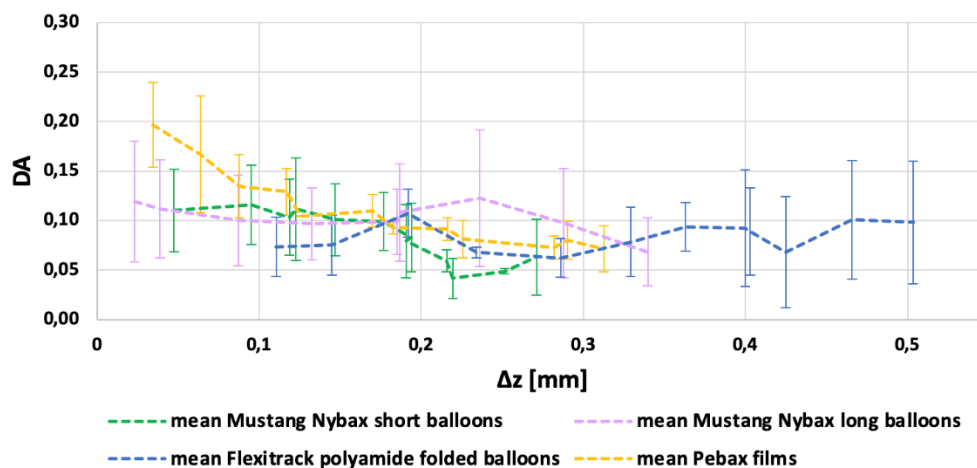
Figure 101: Graphs of the trend in the degree of anisotropy as a function of displacement, for all specimens tested.

A comparison with a material demonstrated to be anisotropic, namely the pericardium membrane (PM), has been conducted using the outcomes from D'Andrea *et al.* work [48].

Figure 102 shows two contour maps of the displacements from three-dimensional laser scanning (left column) and after the grid fit (right column). The ellipsoidal shape of the isolines indicates anisotropy of the material (DA=0.6); while circular height contour lines are found on the isotropy (DA=0.04).
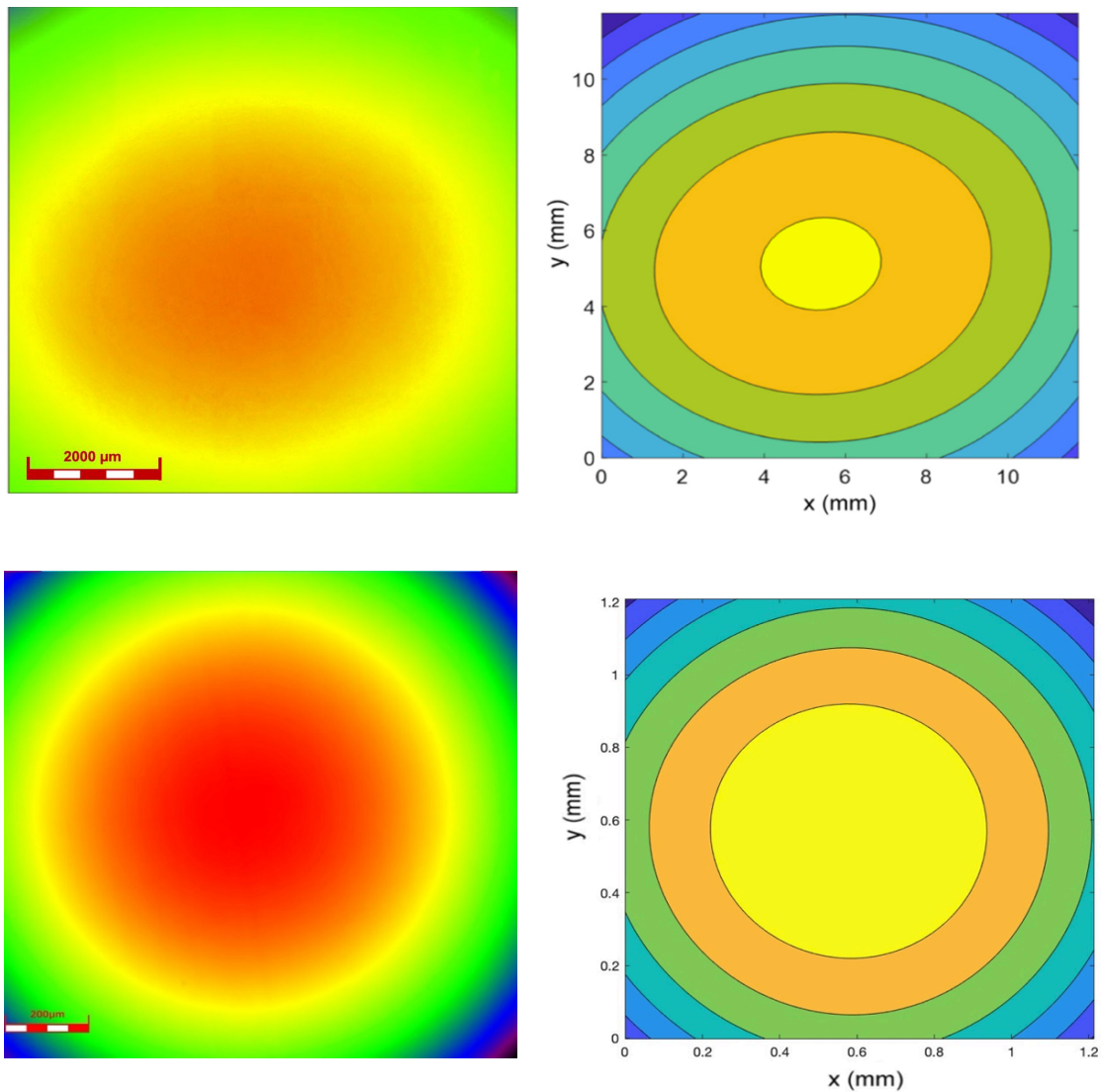
Figure 102: Displacement contours for the anisotropic material (PM) (DA = 0.6) (top) and for Pebax sample (DA = 0.04) (bottom); left column: 3-D topography from confocal laser microscopy; right column: gridded surface.

The investigation of material isotropy also involved a comparison of the outcomes obtained from uniaxial tensile tests conducted along the circumferential and axial orientations (Section 3.2). Eight samples were taken from the circumferential direction to be tested and four samples from the axial one (Figure 103).
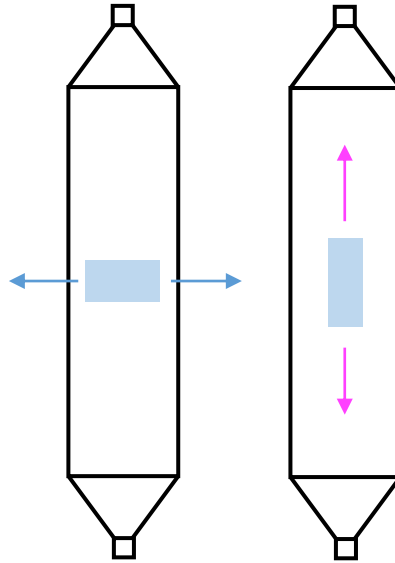
Figure 103: Sampling from the balloon in circumferential (left) and axial direction (right).

The stress-strain curves reported below in Figures 104 and 105 exhibit a similar trend, particularly for strains below 10%, indicating the isotropic behavior of the material, for both short and long Mustang Nybax balloons. However, beyond 10% strain, the stress-strain curves show deviations, suggesting a possible shift towards anisotropic behavior. Since Mustang Nybax balloons does not exhibit strain higher than 10% during bulge testing (see Section 4.3.2), the anisotropy of the material is not apparent during bulging.
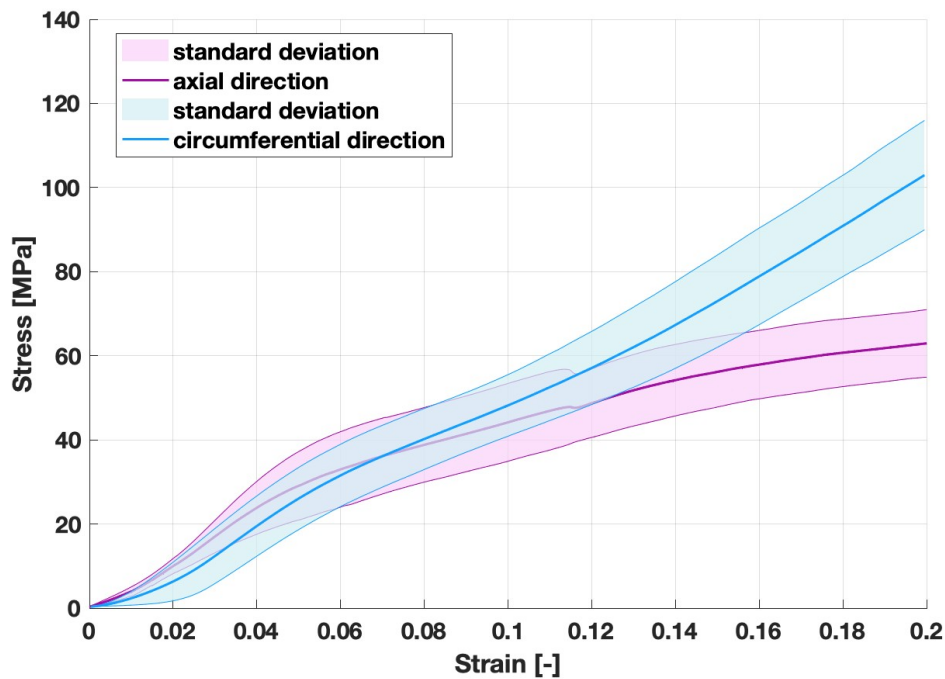
Figure 104: Comparison of Mustang Nybax short balloons tested along circumferential and axial directions.
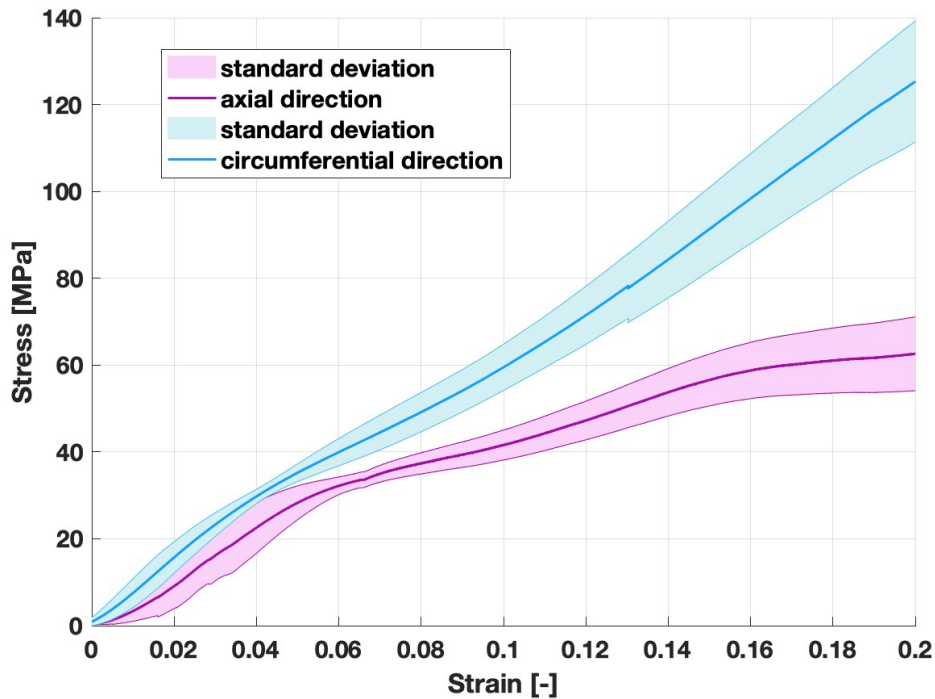
Figure 105: Comparison of Mustang Nybax long balloons tested along circumferential and axial directions.

Regarding the squared Pebax films, specimens were extracted along two distinct directions, denoted as direction 1 and direction 2 (Figure 106). Based on the graph (Figure 107), which displays 6 samples with their corresponding thickness measurements, it can be observed that there is no discernible difference between the two directions. The curves do not show evidence of material anisotropy; however, three of the 6 curves show a substantially lower stress in comparison to the remaining three samples. This mismatch is most likely owed to inaccuracy in thickness measurements.
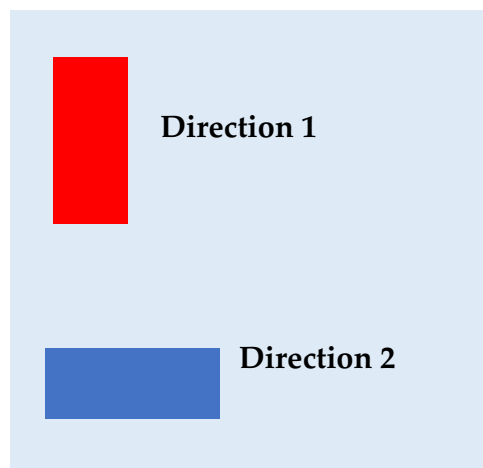
Figure 106: Sampling from the Pebax film along direction 1 and direction 2.
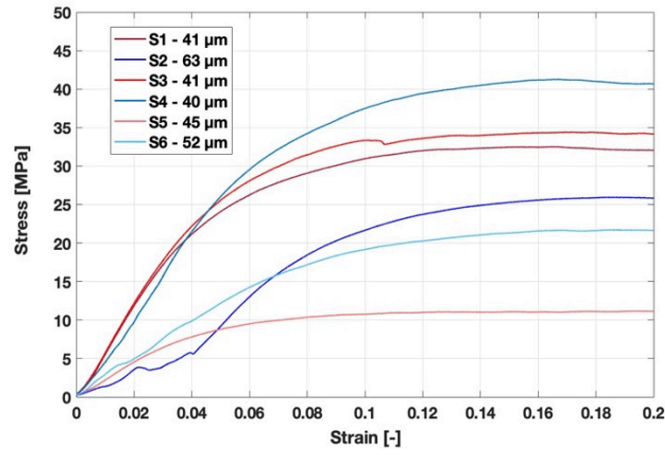
(a)
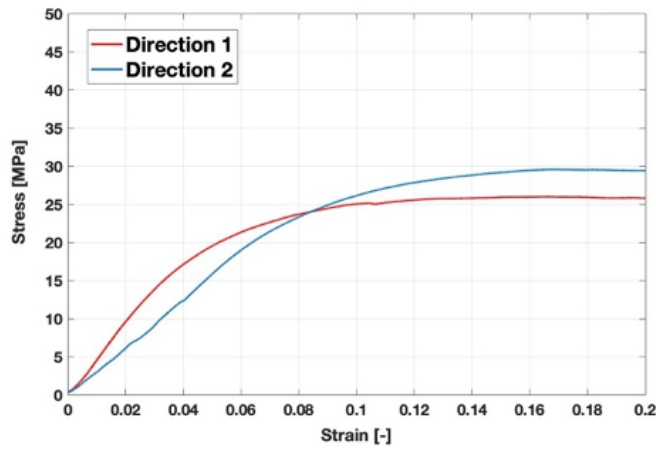
(b)
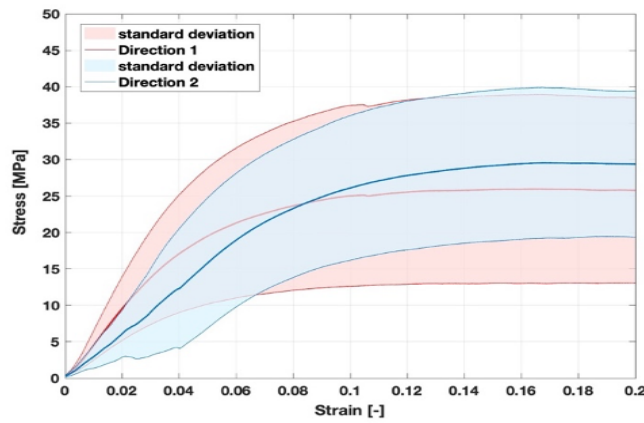
(c)

Figure 107: Comparison of 6 Pebax films tested along the two different directions (a), mean of sample tested along the two directions (b), mean and standard deviation of sample tested along the two directions (c),

4.5. Thickness measurement

4.5.1. Uncoated samples

The thickness of the transparent balloons was measured employing LEXT's *film thickness* tool (Section 3.2.4). The refractive index of Pebax and Nylon is found in the literature to be 1.51[51] and 1.53 [52], respectively. However, the refractive index value for Nybax (a composite of Pebax and Nylon) could not be found. Hence, for the present study, it has been assumed to be the same as that of Pebax.

During the acquisition, the microscope detects two peaks that correspond to the top and bottom surfaces of the material (Figure 108), whose distance gives its thickness.
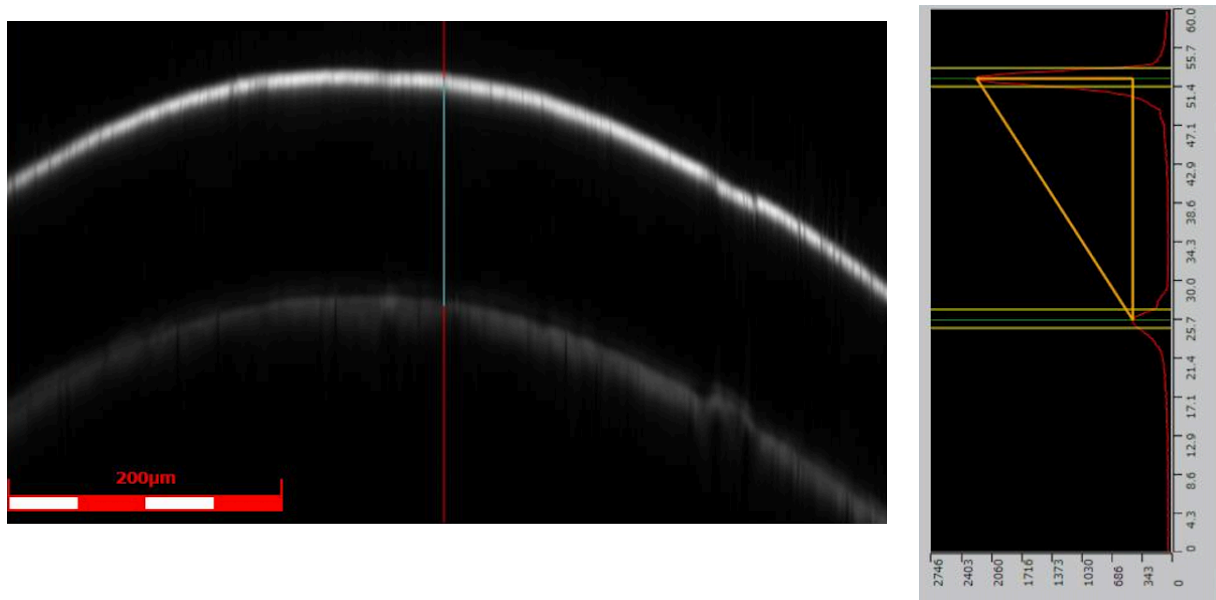
Figure 108: Top and bottom layer of the balloon detected by the laser (left) and thickness measurement as the distance between the peaks located at the top layer and bottom layer (right).

The results of each type of sample are reported in Table 11:

Samples	Thickness [μm]
Mustang Nybax short balloons	45 - 49
Mustang Nybax long balloons	46 - 52
Flexitack polyamide folded balloons	18 - 22
Pebax films	40 - 63

Table 11: Thickness measurement.

In light of these results, a thickness of 50 μm for the unfolded balloons and Pebax films and 20 μm for the folded balloons has been considered.

4.5.2. Coated samples

The coating thickness could not be measured in the same way as the polymer substrate alone because of its opacity. Therefore, to get an idea of the coating thickness, it was measured across a fracture by taking the height difference between the top of the coating and the bottom of the fracture. However, it cannot be determined whether there may be the coating still intact below the fracture or the underlying polymeric material.

The measured values for the polymer-coated samples and drug-coated samples, both deposited by the spray technique, are reported in Tables 12 (left and right). The average thickness is found to be 9.36 μm and 7.23 μm, respectively. Additionally, Figure 109 (left and right) display the measurement locations.

Position	Thickness [μm]
1	8.97
2	10.68
3	10.06
4	8.58
5	8.29
6	7.81
7	10.29
8	11.01
9	8.11
10	9.82

Position	Thickness [μm]
1	7.51
2	6.42
3	7.38
4	6.17
5	8.59
6	7.31

Table 12: Values of the thicknesses of the coating accumulations of the polymer-spray-coated (left) and drug-spray-polymer samples (right).
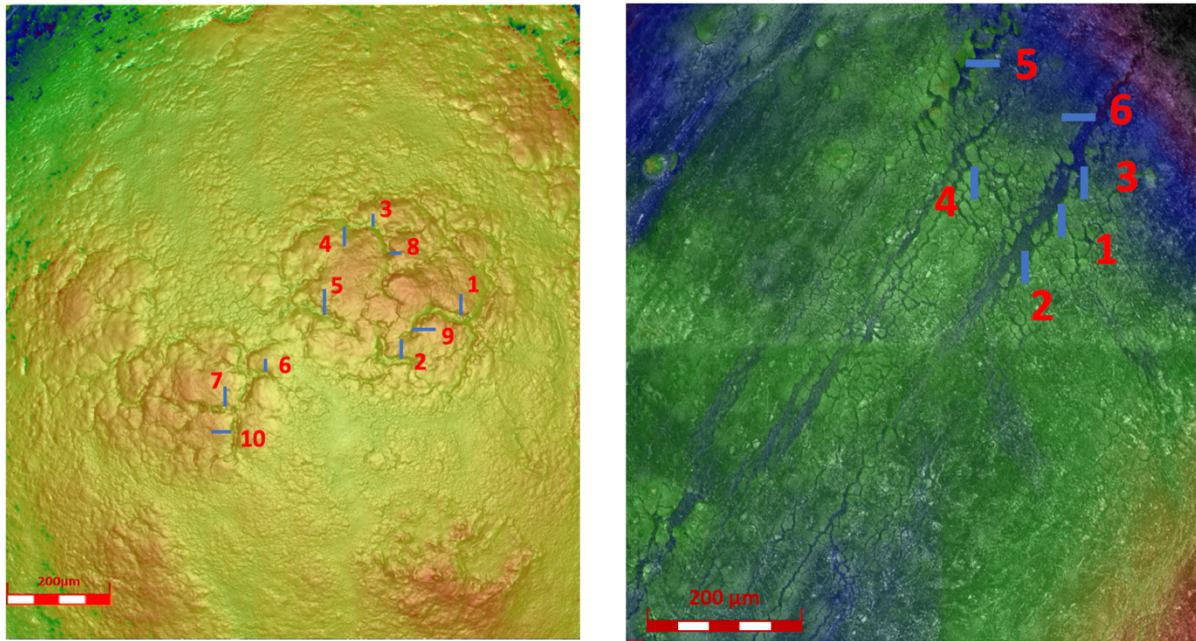
Figure 109: Measurement locations correspond to the height of the fractures in the polymer-spray-coated (left) and drug-spray-polymer samples (right).

Regarding the polymer samples that were coated using the micropipette technique, as no fractures occurred during the bulge test, what was measured were the heights of the coating accumulations. Again, the measured values are provided in Table 13 and the corresponding measurement locations are depicted in Figure 110. The average thickness of the accumulations turns out to be 22.97 µm. This confirms the inhomogeneity of the coating.

Position	Thickness [μm]
1	29.77
2	22.33
3	16.32
4	15.66
5	28.20
6	19.43
7	22.69
8	27.36
9	25.01

Table 13: Values of the thicknesses of the coating accumulations of the polymer-micropipette-coated samples.
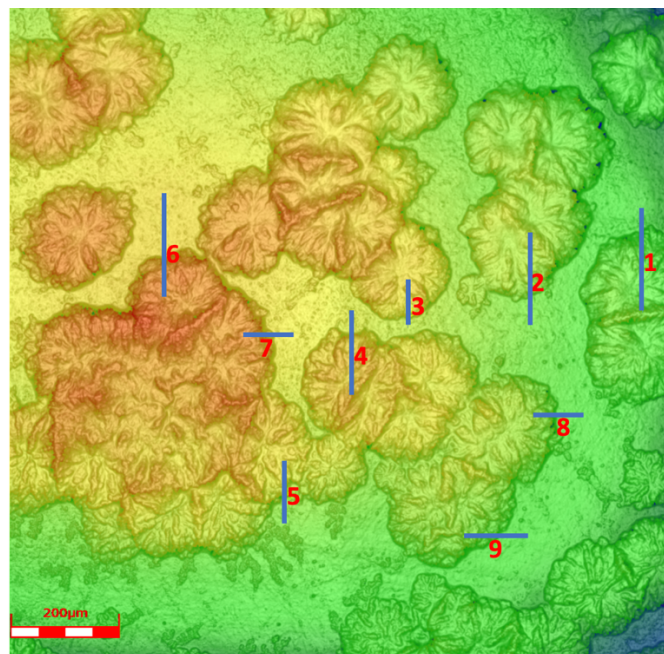
Figure 110: Measurement locations correspond to the height of the coating accumulations in the polymer-micropipette-coated samples.

5 Conclusions, limitations, and further developments

The present study aimed to investigate the mechanical properties of balloon polymer substrates utilized in angioplasty through the inflation test.

To achieve this objective, a custom-made experimental setup consisting of a hydraulic pump for the application of constant pressure, an inflation test device, and a confocal laser microscope for vertical displacement measurement was employed.

The use of water as the pressurizing medium was based on the convenience of easy management and immediate connection with the rest of the circuit. Nonetheless, the manual increase of pressure resulted in limited precision in pressure application to the sample.

The confocal laser microscope was utilized to determine the out-of-plane displacement caused by the inflation of the polymer membrane and to obtain the pressure-deflection profile for each type of specimen.

However, due to the inability to calculate stresses and deformations on the material surface during the experimental testing, a computational analysis was conducted in conjunction with the experimental analysis. To replicate the experimental scenario, a finite element model of the bulge test was created.

To determine the distinctive parameters of the materials required for numerical simulations, uniaxial tensile tests were conducted on unfolded Mustang balloons from Boston Scientific and Pebax films from the University of Montpellier. The folded balloons from both L2MTech and Boston Scientific could not be subjected to testing due to their reduced size and circumferential stiffness, preventing their attachment to the cantilevers. In subsequent research, it would be valuable to develop suitable grasping mechanisms that circumvent the need for adhesive fixation of specimens to the experimental setup.

The stress-strain curves obtained for Nybax suggests that the material demonstrates hyperelastic behavior. Therefore, the Yeoh model was chosen to describe this material. This decision was made for the sake of simplicity and due to a lack of information regarding the behavior of the material upon unloading, neglecting the material's time dependence.

By fitting the analytical and experimental curve, a set of parameters (C_1, C_2 and C_3) was derived. These parameters were used as an indication to investigate through finite element simulations the best possible triad. Through an optimization process, the parameter triplets that fit the bulge pressure-deflection curve were defined.

Overall, it appears that the Yeoh hyperelastic model can adequately fit the experimental data. However, the results of the present study did not establish a clear correlation between alterations in a single parameter and modifications in the slope of the curve. The observed variations in the curve seem to be solely dependent on the joint influence of the three factors. Therefore, it would be advisable to find a relationship that connects the pressure-deflection curve behavior with incremental or decremental changes in the value of each of the individual factors, namely C_1, C_2, and C_3.

Furthermore, with regard to selecting a suitable triplet for folded balloons, additional investigation is necessary. The Yeoh model's constitutive parameters, determined for Nybax unfolded balloons, were applied to Nylon folded balloons. However, as these consist of a composite of Nylon and Pebax, it is plausible that the parameters derived from the unfolded balloons may not entirely reflect the behavior of Nylon alone. Therefore, further research is needed to refine the selection of parameters that accurately capture the behavior of the composite material in the folded balloon configuration.

In contrast, the outcomes derived from the uniaxial testing of Pebax film indicated a nonlinear response with the achievement of a maximum stress at increasing applied strain. Even if unloading protocol was not applied, the hypothesis of elastoplasticity was made. However, the selected model has certain limitations that prevent the finite element simulation from converging. At the point of contact between the material and the metal plate, plasticization of the specimen and subsequent necking occur. One potential approach to improve the numerical model would be to conduct further mesh refinement in the region of interest.

Validated finite element models can be used to infer the stress and strain occurring in the central region of the patch during inflation. In particular, the homogeneity of the strain distribution in the central area is essential for studying the behavior of the coating.

Furthermore, the mechanical properties of the polymer substrates were leveraged to assess the mechanical stability of the excipient layer and excipient-drug system when subjected to strain on the underlying substrates. To this end, samples of excipient-only and excipient-drug-coated Pebax films provided by Montpellier University were subjected to biaxial loading through the bulge test. Images captured with the microscope illustrated the occurrence of coating failure and its association with substrate surface deformation.

In the future, it would be valuable to extract surface deformations directly from the microscope images, utilizing image analysis software to improve the accuracy of the analysis.

It is evident from the polymer-coated samples that the coating method results in variations in coating homogeneity. Specifically, the spray-coated samples demonstrate greater surface uniformity than the micro-pipetted samples, which exhibit a variety of substrate accumulations.

When examining the pressure-deflection behavior, it was observed that all samples exhibit similar trends. However, the uncoated samples demonstrate lower deflection values compared to the coated samples. This unexpected result prompted further investigation. The potential effect of the coating on the underlying material or variations in sample thickness were both considered as possible explanations for this finding. However, an exact determination was not feasible due to the limitations in measuring coating thickness.

In general, the obtained results may be influenced by several factors, the effect of which should be further investigated:

1. Thickness inhomogeneity: due to the manufacturing process, the samples do not have a homogeneous thickness, especially for Pebax films. In data analysis, the thickness considered was obtained by averaging the various measurements.

2. Viscoelastic effects: the viscoelastic nature of the material used in the balloon may have an impact on the experimental results. To ensure the stability of the material, a waiting time of approximately 3 minutes was incorporated after each pressure increment. However, it is important to verify whether this waiting time is adequate to eliminate the influence of viscoelasticity on the experimental outcomes.

3. Effects of laser light: the effect of laser light exposure on the specimens during acquisition should be properly investigated as the timing of each acquisition increases as the sample under investigation is inflated, resulting in varying exposure times. Laser light exposure could cause heating and result in microstructural changes in the sample, potentially impacting the accuracy and reliability of the results obtained.

4. Experimental variability: the placement of the samples on the bulge window or uniaxial test cantilevers can influence the resulting measurements and should be carefully controlled to minimize variability. Given that the samples are cut and glued by the user on the experimental setup, the precision of this process may vary, and as a result, impact the results.

108

6 Bibliography

[1] I. J. Kullo and T. W. Rooke, "Peripheral Artery Disease," *New England Journal of Medicine*, vol. 374, no. 9, pp. 861–871, Mar. 2016.

[2] J. A. Anderson, S. Lamichhane, T. Remund, P. Kelly, and G. Mani, "Preparation, characterization, in vitro drug release, and cellular interactions of tailored paclitaxel releasing polyethylene oxide films for drug-coated balloons," *Acta Biomater*, vol. 29, pp. 333–351, 2016.

[3] E. Goel *et al.*, "Pre-clinical investigation of keratose as an excipient of drug coated balloons," *Molecules*, vol. 25, no. 7, pp. 1–12, 2020.

[4] G. A. Holzapfel, C. A. J. Schulze-Bauer, and M. Stadler, "Mechanics of angioplasty: Wall, balloon and stent," *ASME International Mechanical Engineering Congress and Exposition, Proceedings (IMECE)*, vol. 2000-Z, pp. 141–156, 2000, doi: 10.1115/IMECE2000-1927.

[5] M. C. Berg, H. Kolodziej, B. Cremers, G. Gershony, and U. Speck, "Drug-coated angioplasty balloon catheters: Coating compositions and methods," *Adv Eng Mater*, vol. 14, no. 3, pp. 45–50, 2012, doi: 10.1002/adem.201180067.

[6] J. A. Warner, B. Forsyth, F. Zhou, J. Myers, C. Frethem, and G. Haugstad, "Characterization of Pebax angioplasty balloon surfaces with AFM, SEM, TEM, and SAXS," *J Biomed Mater Res B Appl Biomater*, vol. 104, no. 3, pp. 470–475, 2016, doi: 10.1002/jbm.b.33414.

[7] D. Jackson, D. Tong, and J. Layland, "A review of the coronary applications of the drug coated balloon," *International Journal of Cardiology*, vol. 226. Elsevier Ireland Ltd, pp. 77–86, Jan. 01, 2017. doi: 10.1016/j.ijcard.2016.09.045.

[8] S. Kaule *et al.*, "Correlating coating characteristics with the performance of drug-coated balloons - A comparative in vitro investigation of own established hydrogel- and ionic liquid-based coating matrices," *PLoS One*, vol. 10, no. 3, pp. 1–18, 2015, doi: 10.1371/journal.pone.0116080.

[9] G. M. Xiong *et al.*, "Materials technology in drug eluting balloons: Current and future perspectives," *Journal of Controlled Release*, vol. 239. Elsevier B.V., pp. 92–106, Oct. 10, 2016. doi: 10.1016/j.jconrel.2016.08.018.

[10] E. A. Turner, M. K. Atigh, M. M. Erwin, U. Christians, and S. K. Yazdani, "Coating and Pharmacokinetic Evaluation of Air Spray Coated Drug Coated

Balloons," *Cardiovasc Eng Technol*, vol. 9, no. 2, pp. 240–250, 2018, doi: 10.1007/s13239-018-0346-1.

[11] S. Woolford *et al.*, "Studying the effect of drug-to-excipient ratio on drug release profile for drug coated balloons," *Int J Pharm*, vol. 620, no. April, p. 121749, 2022, doi: 10.1016/j.ijpharm.2022.121749.

[12] A. H. Matsumoto, J. Klemens, H. Barth, J. B. Selby, and C. J. Tegtmeyer, "CardioVascular and Interventional Radiology Peripheral Angioplasty Balloon Technology."

[13] J. E. Abele1, "Balloon Catheters and Transluminal Dilatation: Technical Considerations."

[14] Zollikofer *et al.*, "Mechanism of transluminal angioplasty", 1992.

[15] J Gerlock *et al.*, "An examination of the physical characteristics leading to angioplasty balloon rupture".

[16] W. E. A. S. et al. Shawn N. Sarin, "Balloon Catheters," vol. Chapter 5.

[17] Sr. James C. WangJohn AbeleGeorge T. RobertsBrian A. Pederson, "Method of forming a co-extruded balloon for medical purposes".

[18] Boston Scientific, "MUSTANG ™ Balloon Dilatation Catheter Brochure."

[19] M. A. Geith *et al.*, "Experimental and mathematical characterization of coronary polyamide-12 balloon catheter membranes," *PLoS One*, vol. 15, no. 6, Jun. 2020, doi: 10.1371/journal.pone.0234340.

[20] F. Sadeghi and D. Le, "Characterization of polymeric biomedical balloon: Physical and mechanical properties," *Journal of Polymer Engineering*, vol. 41, no. 9, pp. 799–807, Oct. 2021, doi: 10.1515/polyeng-2021-0203.

[21] Mabry E., " Extruded Tubing Designed for Balloon Production," *MDDI. Tubing*, 2008.

[22] R. D. v. Dominick V., "Blow molding," *Plastic Product Material and Process Selection Handbook*, vol. 6, 2004.

[23] A. Holzapfel *et al.*, "Mechanics of Angioplasty: Wall, Balloon and Stent ," 2021.

[24] I. Rykowska, I. Nowak, and R. Nowak, "Drug-eluting stents and balloons-materials, structure designs, and coating techniques: A review," *Molecules*, vol. 25, no. 20. MDPI AG, Oct. 01, 2020. doi: 10.3390/molecules25204624.

[25] J. P. Sheth, J. Xu, and G. L. Wilkes, "Solid state structure-property behavior of semicrystalline poly(ether-block-amide) PEBAX w thermoplastic elastomers." [Online]. Available: www.elsevier.com/locate/polymer

[26] F. Sadeghi and D. Le, "Characterization of polymeric biomedical balloon: Physical and mechanical properties," *Journal of Polymer Engineering*, vol. 41, no. 9, pp. 799–807, Oct. 2021, doi: 10.1515/polyeng-2021-0203.

[27] M. A. Geith *et al.*, "Experimental and mathematical characterization of coronary polyamide-12 balloon catheter membranes," *PLoS One*, vol. 15, no. 6, Jun. 2020, doi: 10.1371/journal.pone.0234340.

[28] J. P. Sheth, J. Xu, and G. L. Wilkes, "Solid state structure-property behavior of semicrystalline poly(ether-block-amide) PEBAX w thermoplastic elastomers." [Online]. Available: www.elsevier.com/locate/polymer

[29] F. Sadeghi and A. Ajji, "Structure, Mechanical and Barrier Properties of Uniaxially Stretched Multilayer Nylon/Clay Nanocomposite Films," *International Polymer Processing*, 2013.

[30] S. Rhee and J. L. White, "Crystal structure and morphology of biaxially oriented polyamide 12 films," *J Polym Sci B Polym Phys*, vol. 40, no. 12, pp. 1189–1200, Jun. 2002, doi: 10.1002/polb.10181.

[31] M. K. Small and W. D. Nix, "Analysis of the accuracy of the bulge test in determining the mechanical properties of thin films," *J Mater Res*, vol. 7, no. 6, pp. 1553–1563, 1992, doi: 10.1557/JMR.1992.1553.

[32] Xian Xuying, "Development of a bulge test experimental setup for the in-situ mechanical characterization of metal thin films on polymer substrate."

[33] J. S. and A. B. G. Matthiesen, "Pressure control for a hot gas bulge test using parallel on-off valves," 2017.

[34] L. Yang, S. G. Long, Z. S. Ma, and Z. H. Wang, "Accuracy analysis of plane-strain bulge test for determining mechanical properties of thin films," *Transactions of Nonferrous Metals Society of China (English Edition)*, vol. 24, no. 10, pp. 3265–3273, 2014, doi: 10.1016/S1003-6326(14)63466-X.

[35] E. Plancher *et al.*, "Tracking microstructure evolution in complex biaxial strain paths: A bulge test methodology for the scanning electron microscope," *Exp Mech*, vol. 60, pp. 35–50, 2020.

[36] C. Jayyosi, K. Bruyère-Garnier, and M. Coret, "Geometry of an inflated membrane in elliptic bulge tests: Evaluation of an ellipsoidal shape approximation by stereoscopic digital image correlation measurements," *Med Eng Phys*, vol. 48, pp. 150–157, Oct. 2017, doi: 10.1016/j.medengphy.2017.06.020.

[37] S. Cutugno *et al.*, "Patient-specific analysis of ascending thoracic aortic aneurysm with the living heart human model," *Bioengineering*, vol. 8, no. 11, Nov. 2021, doi: 10.3390/bioengineering8110175.

[38] T. C. Gasser, "Biomechanical Rupture Risk Assessment," *AORTA*, vol. 04, no. 02, pp. 42–60, Apr. 2016, doi: 10.12945/j.aorta.2015.15.030.

[39] C. S. Lin *et al.*, "Mechanical properties measurement of polymer films by bulge test and fringe projection," *Advances in Materials Science and Engineering*, vol. 2014, 2014, doi: 10.1155/2014/170279.

[40] B. L. Boyce, J. M. Grazier, R. E. Jones, and T. D. Nguyen, "Full-field deformation of bovine cornea under constrained inflation conditions," *Biomaterials*, vol. 29, no. 28, pp. 3896–3904, Oct. 2008, doi: 10.1016/j.biomaterials.2008.06.011.

[41] T. K. Tonge, L. S. Atlan, L. M. Voo, and T. D. Nguyen, "Full-field bulge test for planar anisotropic tissues: Part I-Experimental methods applied to human skin tissue," *Acta Biomater*, vol. 9, no. 4, pp. 5913–5925, 2013, doi: 10.1016/j.actbio.2012.11.035.

[42] Zioupos P., Barbenel J. C., and Fisher J., "Mechanical and optical anisotropy of bovine pericardium," *Med. Biol. Eng. Comput.*, vol. 30, pp. 76–82, 1992.

[43] L. H. M. Palmeth, M. A. G. Carmona, and J. M. Castro, "Design and analysis of a bulge test device," *Ingenieria e Investigacion*, vol. 41, no. 3, Dec. 2021.

[44] N. Rull *et al.*, "Constitutive modelling of the mechanical response of a polycaprolactone based polyurethane elastomer: Finite element analysis and experimental validation through a bulge test," *Journal of Strain Analysis for Engineering Design*, vol. 56, pp. 206–215, 2021.

[45] X. T. J. M. Considine, "Use of bulge test geometry for material property identification," *Springer New York LLC*, vol. 8, pp. 43–46, 2018.

[46] M. M. Sylvester, "Learning Experience in Designing a Hydraulic Bulge Test Setup for Material Properties Characterization."

[47] A. Romo *et al.*, "In vitro analysis of localized aneurysm rupture," *J Biomech*, vol. 47, pp. 607–616, 2014.

[48] L. D.' Andrea *et al.*, "Anisotropic mechanical response of bovine pericardium membrane through bulge test and in-situ confocal-laser scanning.", 2022.

[49] J. Zhang, F. Xue, Y. Wang, X. Zhang, and S. Han, "Strain energy-based rubber fatigue life prediction under the influence of temperature," *R Soc Open Sci*, vol. 5, no. 10, Oct. 2018, doi: 10.1098/rsos.180951.

[50] "3D Measuring Laser Microscope OLS4100."

[51] ulprospectors, "Pebax® MH 2030."

[52] A. Yahya *et al.*, "Optical Characterization and Properties of Polymeric Materials for Optoelectronic and Photonic Applications," 2013.

List of figures

List of tables